Phase and texture development of intermetallics in the Al-Mg binary system using metal matrix composites

Doctoral Thesis
(Dissertation)

to be awarded the degree
Doctor of Engineering (Dr.-Ing.)

Submitted by
Soheil Sanamar
from Hamedan, Iran

approved by the Faculty of Natural and Materials Science
Clausthal University of Technology

Date of oral examination
24.06.2020

Dean

Prof. Dr. -Ing. Karl-Heinz Spitzer

Chairperson of the Board of Examiners

Prof. Dr. -Ing habil. Joachim Deubener

Supervising tutor

apl. Prof. Dr. rer. nat. Dr.-Ing. habil. Heinz-Günter Brokmeier

Reviewer

Prof. Dr. -Ing. habil. Florian Pyczak

Tag der Einreichung: 03.12.2019
Tag der mündlichen Prüfung: 24.6.2020

Abstract

There is still some debate about the nature of the phase transformations that take place in the central region of the Al-Mg binary phase diagram and the formation kinetics of the intermetallic phases that are formed. The purpose of the current work is to characterize the phase formation reaction between Al and Mg and to better understand the formation kinetics of the intermetallic phases that form in the binary Al-Mg system. Therefore, two compositions, Al60Mg40 and Al40Mg60 (wt. %) were investigated, which are very suitable for studying the central part of the Al-Mg phase diagram. Powder metallurgy, including cold extrusion was used to create a large interface between the Al and Mg, which facilitates fast reaction kinetics. In order to observe the phase formation and to analyze their crystal structures, X-ray diffraction using synchrotron radiation was used. This technique offers advantages due to its high brightness and brilliance, enabling the detection of small phase fractions, and has proven to be extremely effective in resolving complex phase studies. Moreover, synchrotron radiation coupled with a fast read-out area detector, makes in situ investigations of phase transformations possible with a high time resolution. The effects of crystal orientation distribution (texture) on the physical and mechanical properties of metallic alloys is well known. Supplementary to the information on phase development, texture at high temperature was also determined to get information on the orientation relationships between the Al and Mg and the intermetallic phases that formed.

Texture development and phase analysis were both performed using ex-situ and in-situ experiments. The γ-$Al_{12}Mg_{17}$-phase is the first phase formed in both the alloy compositions, Al40Mg60 and Al60Mg40. After the γ-$Al_{12}Mg_{17}$-phase has reached a critical thickness, the β-Al_3Mg_2–phase is formed. Thus the γ-phase is the first to form in the system.

After annealing at 400 °C for 2 h, the Al40Mg60 composition consisted of a very high amount of $Al_{12}Mg_{17}$ and a small amount of Al_3Mg_2 while the Al60Mg40 composition consisted of $Al_{12}Mg_{17}$ and Mg, indicating that thermodynamic equilibrium has been approached. On further annealing at 400 °C for 12 h, both compositions formed one phase, this was the $Al_{12}Mg_{17}$ phase in the Al40Mg60 composition and Al_3Mg_2 in the Al60Mg40 composition.

Due to the extrusion process, a texture gradient was observed over the cross-section of both compositions. The aluminum phase showed a typical texture component of plane-strain deformation in the middle part of the extruded bar and a uniaxial deformation texture near the surface. In the central region of the extruded bars, the (0002) Mg pole figure showed a split along the extrusion direction (±ED), resulted from the activation of c+a glide. These two poles twist towards the transverse direction on moving towards the surface of the extruded bar; one pole moving towards +TD and the other one towards −TD. The angle of twist increased up to 90° towards the TD surface.

After annealing at 200 °C for 12 h, a recrystallization texture was observed in both the Al and Mg for both compositions. This recrystallization can be recognized by a 30° rotation of the Mg crystals and by the formation of a cube texture component in the Al phase.

After annealing the Al40Mg60 composition at 400 °C for 12 h, a texture transformation occurred. This resulted in the (110) plane of $Al_{12}Mg_{17}$ being parallel to the (0001) plane of Mg and the $(1\bar{1}0)$ plane of the $Al_{12}Mg_{17}$ being parallel to the $(1\bar{1}00)$ of Mg. This indicates that an orientation relationship between the Mg and the $Al_{12}Mg_{17}$ phases was formed.

Zusammenfassung

Die genaue Abfolge der Phasenreaktionen, die im zentralen Bereich des binären Phasendiagramms von Al-Mg bei der Reaktion von intermetallischen Phasen aus den festen Phasen stattfindet, ist ein umstrittenes Thema aktueller Forschung. Ziel der vorliegenden Arbeit ist es, die Phasenbildungsreaktion zwischen elementarem Al und Mg zu charakterisieren und die Bildungskinetik der intermetallischen Phasen, die sich im binären Al-Mg-System bilden, besser zu verstehen. Es wurden zwei Verbundwerkstoffproben mit der Zusammensetzung, Al60Mg40 und Al40Mg60 (Gew.-%), untersucht, die sich sehr gut zum Studium des zentralen Teils des Al-Mg-Phasendiagramms eignen. Pulvermetallurgie zusammen mit Strangpressen bei Raumtemperatur wurde eingesetzt, um bei der Proben-herstellung eine große innere Grenzfläche zwischen Al und Mg herzustellen. Um die Phasenbildung zu beobachten und die gebildeten Kristallstrukturen zu analysieren, wurde Röntgendiffraktion mit 87keV Synchrotronstrahlung eingesetzt. Diese Strahlung bietet wegen der hohen Brillanz Vorteile, so dass die Detektion kleinster Phasenanteile ermöglicht wird. Mit einem schnellen Flächendetektor wurden in-situ Untersuchungen mit hoher zeitlicher Auflösung durchgeführt. Der Einfluss der Kristallorientierungsverteilung (Textur) auf die physikalischen und mechanischen Eigenschaften von metallischen Legierungen ist bekannt. Ergänzend zu den Informationen über die Phasenentwicklung wurde auch die Textur bei hoher Temperatur untersucht, um Informationen über die Orientierungsbeziehungen zwischen Al und Mg und den gebildeten intermetallischen Phasen zu erhalten.
Sowohl die Texturentwicklung als auch die Phasenanalyse wurden mit ex-situ- und in-situ-Experimenten durchgeführt. Die γ-$Al_{12}Mg_{17}$-Phase ist die erste Phase, die in den beiden Legierungszusammensetzungen Al40Mg60 und Al60Mg40 gebildet wird. Nachdem die γ-$Al_{12}Mg_{17}$-Phase eine kritische Dicke als Grenzschicht erreicht hat, wird die β-Al_3Mg_2-Phase gebildet. Nach dem Glühen bei 400 ℃ für 2 h hatten sich in der Probe Al40Mg60 ein hoher Anteil an $Al_{12}Mg_{17}$ und ein geringer Anteil an Al_3Mg_2 ausgebildet, während die Probe mit der Zusammensetzung Al60Mg40 aus $Al_{12}Mg17$ und Mg bestand. Beim weiteren Glühen bei 400 ℃ für 12 h reagierten beiden Verbundproben zu einer einphasigen intermetallischen Probe. Dies war die $Al_{12}Mg_{17}$-Phase für die Verbundprobe mit der Zusammensetzung Al40Mg60 und Al_3Mg_2 für die Verbundprobe mit der Zusammensetzung Al60Mg40.
Aufgrund des Strangpressprofils wurde ein Texturgradient über den Probenquerschnitt gebildet. Aluminium zeigt typische Texturkomponente der Verformung. Ebene Verformung im Zentrum wechselt zu uniaxialer Verformung am Rand. Mg zeigt die typische Aufspaltung in der (0002)-Mg-Polfigur im Probenzentrum, wie sie für c+a Gleitung beschrieben wurde. Diese Pole scheren kontinuierlich in Richtung Querrichtung des Strangpressprofils. Der Drehwinkel steigt bis nahe 90° je näher sich die Messposition an die Oberfläche in Querrichtung nähert.
Nach dem Glühen bei 200 ℃ für 12 Stunden wurde eine Rekristallisationstexturkomponente sowohl im Al als auch im Mg für beide Zusammensetzungen beobachtet. Diese Rekristallisation ist im Mg durch eine 30° Drehung der Mg-Polfigur und durch die Bildung einer Würfeltexturkomponente in der Al-Phase erkennbar.
Analog zur Phasentransformation wurde an der Verbundprobe mit der Zusamensetzung Al40Mg60 die Texturtransformation untersucht. Bei 400 ℃ für 12 h führte dies dazu, dass die (110) Ebene von $Al_{12}Mg_{17}$ parallel zur (0001) Ebene von Mg und die $(1\bar{1}0)$ Ebene von $Al_{12}Mg_{17}$ parallel zur $(1\bar{1}00)$ von Mg orientiert war. Dies deutet darauf hin, dass eine Orientierungsbeziehung zwischen den Phasen Mg und $Al_{12}Mg_{17}$ vorhanden ist.

Acknowledgments

This thesis and the research during my Ph.D. work, while being an individual piece of work, benefited from contribution, advice and guidance of many people.

First of all, I would like to express my sincere gratitude to Prof. Heinz-Günter Brokmeier for giving me the chance to explore the world of texture. I would also like to thank him for the possibility he gave me to widen my scientific background by studying different new metallic alloys in addition to my Ph.D. topics. I particularly appreciated the open-door policy of his office. We had many numerous discussions together, not only on the different diffraction methods, texture and phase analysis but also on the fundamentals of material science and many different materials and most recently on ceramics and rocks. Having so many discussions made me change the way I was thinking on the fundamentals of material science before and after my Ph.D.

Besides Prof. Brokmeier I would like to express my sincere regards to Prof. Florian Pyczak. Many thanks for constant interest in my work and his availability in all kinds of situations and all his constructive comments.

I would like to express my thanks to the past and present scientific colleagues of the TU Clausthal for their help, kindness and friendship.

I acknowledge the Helmholtz Zentrum Geesthacht GEMS outstation at DESY for the provided beamtime. Thanks to Dr. Norbert Schell for his collaboration on performing the measurements.
I would like to show my greatest appreciation to the selfless compassionate technical support provided by Bernd Schwebke from HZG and Rüdiger Nowak from DESY.

I acknowledge the departments WMF and WPM at HZG for generous support during using their facilities for the EBSD sample preparations and measurements. I would like thank Prof. Robert A.Schwarzer from TU Clausthal for many discussions about the EBSD measurements and sample preparations.

In Helmholtz Zentrum Geesthacht (HZG) I had the opportunity to work in ideal conditions, not only because of the overall infrastructure and free access to analytical facilities but above all due to the great working atmosphere. Special thanks to Regina Rossmann, and Nicola Kampner at HZG.

I would like to show my greatest appreciation to my very good friends, Dr. Michael Oehring, Dr. Andreas Stark, Prof. Michael Dahms, Dr. Jonathan Paul, from HZG for all their selfless frequent help, generous assistance and advice with many questions I always had.

I would like to thank Chang Liu, who during supervision of her master thesis became a teacher in the field. Having her at office was a nice time as well.

Most of all, I thank my parents and family for their moral supports and their faith, which played a crucial role for successfully carrying out this thesis research. I would like to thank my father, dearest Ahmad, my brother, dearest Amirhossein and his family, my sister dearest Saghi and her family.

Specifically, I thank my mother, who sacrificed everything for me. This thesis is lovingly dedicated to you, Fatemeh Dadfarma. Thank you for the unfaltering support and encouragement that you provided me throughout my life. I am grateful for having you as important part of my life.

I owe very important debt for many scientific communications with the experts in these fields; those and also those countless people who I have failed to mention here, many thanks.

Table of Contents:

1 Motivation and objective

Considerable experimental and theoretical efforts have been expended on studying the binary aluminum-magnesium phase diagram in order to understand the solid-state reactions that occur between the Al and Mg. The first complete review of the Al-Mg phase diagram was published by Murray [1] (see Figure 1.1-1) followed by Su et al. [3], Okamoto [4] and Czeppe et al.[5]. As can be expected from the phase diagram, the solid-state reaction between Al and Mg leads to the formation of intermetallic phases. The occurrence of intermetallic phases has been studied in several works using different experimental methods like scanning electron microscopy [6], differential scanning calorimetry (DSC)[6], thin film reactions[7], XRD [8], accumulative roll bonding [9] and TEM [10] analysis.

One reason to study these intermetallic phases is that they have been detected in many engineering materials that have been subjected to processing procedures such as mechanically alloying, where powder is produced by high energy ball milling of Al and Mg powders[11], casting [12] of Al-Mg alloys and also after welding through different welding technologies of Al and Mg alloys [13,14], therefore, the intermetallic phases in the system Al-Mg have gained much interest in recent years.

Up to now the nature of the phase transformations taking place in the center of the Al-Mg binary phase diagram and the formation kinetics of the intermetallic phases remains unclear. Different experimental methods are probably one reason for some of the discrepancies, which have existed until now with respect to the central part of the Mg-Al equilibrium phase diagram. Another possible reason for these discrepancies could be that Mg easily oxidizes. The different experimental techniques employ different cooling rates and different metastable phases may form on cooling. Therefore, there is uncertainty about the nature and occurrence of the intermetallic phases as indicated by various authors.

In this work, two compositions, Al60Mg40 and Al40Mg60 were used, which are very suitable for studying the central part of Al-Mg phase diagram. The powder metallurgy method including cold extrusion was used to create a large surface interface between the Al and Mg, which facilitates fast diffusion. In order to observe phase formation and analyze crystal structures synchrotron radiation was used, which due to its high brightness and brilliance has the ability to detect small phase fractions has proven to be extremely effective in resolving complex phase studies. Moreover, synchrotron radiation coupled with a fast read-out area detector, makes in-situ investigations of phase transformations possible with a high time resolution.

The general effects of crystal orientation distribution (texture) on the physical and mechanical properties of metallic alloys are well known. Additionally, many intermetallic alloys have anisotropic elastic/plastic behavior. To date these effects have not been adequately addressed for intermetallic alloys. In addition, after most phase transformations, some orientation relationships may exist between the parent and the product phases, which give us additional information about the nucleation and growth processes.

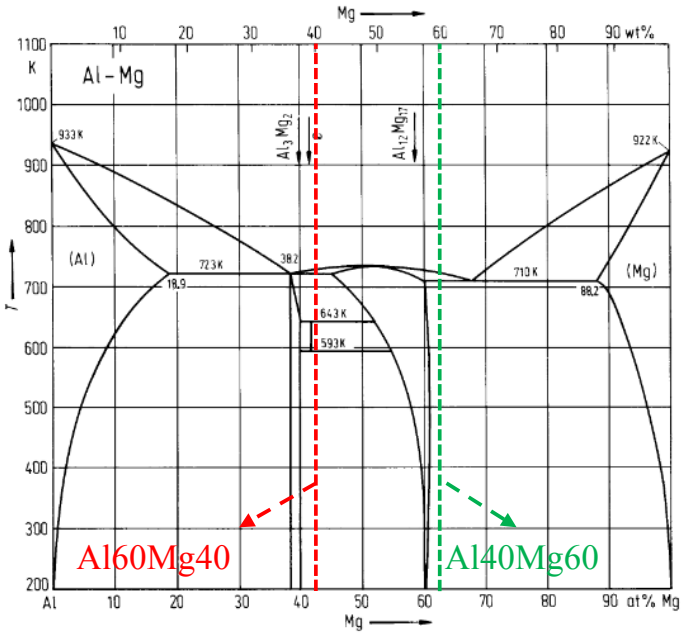

Figure 1.1-1 The binary Al-Mg phase diagram suggested by Murray[1].

2 State of Art

2.1 The Al-Mg binary phase diagram

In general, the solid-state reaction between Al and Mg results in the formation of intermetallic phases. Considerable experimental and theoretical efforts have been undertaken to study the binary aluminum-magnesium phase diagram (see Figure 2.1-1). The first complete review was published by Murray [1], followed by Schürmann and Voss [15], Su et al.[3], and Okamoto [4] with the middle part of the phase diagram being investigated by Czeppe et al.[5]. Murray in her assessment, which remains one of the most complete overviews on the binary Al-Mg phase diagram, proposed the existence of three intermetallic phases, namely γ-$Al_{12}Mg_{17}$ with a composition range between 45 and 60.5 at % Mg, β-Al_3Mg_2 with a composition range between 38.5 and 40.3 at% Mg and a R-phase ,which was sometimes called the ε phase (Su et al. [3]), and exists at a composition around 44.0 at %Mg.
The γ and β phases form as a result of a eutectic reaction L → (Mg) + γ at about 437 °C and a L → (Al) + β at about 450 °C or via a eutectoid reaction at about 250 °C and are stable down to room temperature. The compositional range of the γ-phase varies slightly in the literature compared to Murray's suggestion, which was between 45-52 at % Mg. The later work by Su et al. [3] discussed the compositional range of the γ phase that is in equilibrium with the β and ε phases. The single γ-phase field exist at 45.8 at % Mg at 445 °C to 48.1 at. % Mg at 350 °C. Although the β phase is reported by Su et.al [3] to have the composition range 38-40 at% Mg, and essentially does not change with temperature. Saunders [16] also suggested a narrow composition range close or at 38.5 at% Mg for the β-phase, which is actually the same value as reported by Su. et al. [3]. For the third phase R(ε), the composition range proposed by Murray was a narrow region at 44 at% Mg, who considered the Mg loss for her calculation and is in good agreement with Zhou [17] and Su et al. [3], or 43.5- 44.8 at % by Okamoto[4], and it forms via a very sluggish reaction. The ε phase has been reported by Schürmann and

Voss [15] to form on cooling via a transformation of the liquid phase during the peritectic reaction L+ ζ→ ε at 450 ℃ [3]. The presence of the phase named ζ-phase was suggested by Schürmann and Voss [15] to exist within the temperature range 450 °C to 435 °C with a stoichiometry of $Al_{52}Mg_{48}$. The presence of this phase is not mentioned in other work or via a peritectoid reaction γ + β→ ε according to [18] at a temperature 401±5 °C [2] and 370±5 °C [1]. Samson [2] suggested that the upper temperature for the formation of the ε phase is between 380 and 395℃, where Murray [1] stated that the highest temperature limit to be 405± 5 °C and suggested it forms via a peritectoid reaction between γ- and β-phases at 370± 5 °C and subsequently decomposed at 320 °C to β and γ. Su et al.[3] established 410 °C as the upper limit for this phase and indicated that due to the very slow reaction of the ε-phase it is difficult to indicate the lower temperature limit but it could be around 250 °C. Czeppe et al. [5] reported the upper temperature limit for ε as 427± 1 °C, but did not suggest the lower temperature limit for this phase. Su et al. [3] also suggested the presence of a fourth phase, a λ-phase forming via a peritectic reaction L+ γ → λ at a temperature of 450 °C which over the temperature range 435 - 445 °C dissociates into the γ and β phases. A similar constitution was suggested by the phase diagram of Okamoto [4]. He compiled some previous assessments of the Al-Mg phase diagram. The existence of the λ-phase was not observed in the investigation of Czeppe et al. [5] and they reported that the observations by Su et al. [3] could be a result of oxide contamination. In conclusion, there clearly exist some debate concerning the Al-Mg binary phase diagram in the composition range between 40 and -60 at %Mg, but there is no doubt about the existence of the γ, β and ε phases.

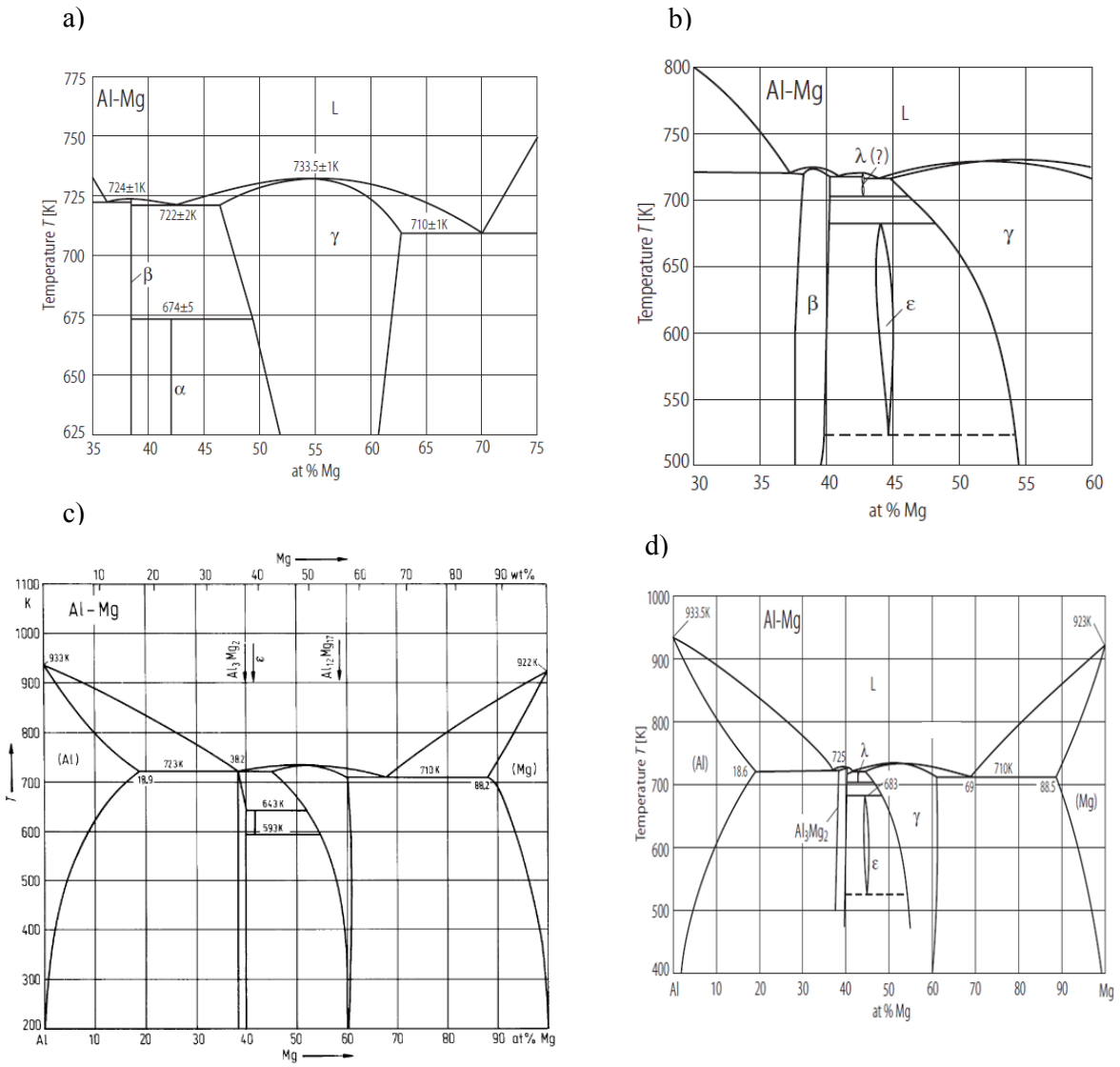

Figure 2.1-1: a) Partial phase diagram calculated by Zuo and Chang [17] , b) partial phase diagram suggested by Su et al. [3] , c) phase diagram suggested by Murray [1] and d) the partial phase diagram proposed by Okamoto [4].

2.2 Kinetics and thermodynamics of phase formation by interdiffusion of elemental mixtures

The transport of species of atoms, ions or molecules in a medium like a solid, gas or liquid defines the term diffusion, caused by the random motion of atoms. This atomic transport occurs under a gradient in the chemical potential, which can arise due to differences in

concentration, electrical potential, thermal or even stress gradients, and reduces the gradient. In solids more specifically, the thermal activation can cause the atoms changing their lattice sites, referred as solid state diffusion. The driving force for atomic transport is to lower the free energy of the system, in order to reach thermodynamic equilibrium. Therefore, atoms migrate in a solid medium e.g. to decrease the gradient in the chemical potential. More on this subject can be found in [19].

Solid-state phase formation will occur, when there is a driving force for the reaction. Generally, the Gibbs free energy of a phase, e.g. the Al-Mg solid solution is given by:

$$\Delta G = \Delta H - T\Delta S \qquad \text{Equation 2.2-1}$$

Where ΔH is the enthalpy and ΔS is the entropy of the respective phase, in this case the solid solution. In certain cases, other free energy contributions have to be taken into account, e.g. the interfacial energy or the strain energy.

Depending on the thermodynamics and the resulting phase diagram, an initial mixture of elements will transform into a solid solution and/or intermetallic phases via a solid-state reaction if the temperature and time are sufficient to allow interdiffusion of the elements [20]. This reaction includes the transition of atoms of one substance through the interface from one phase to another. The process of such a reaction is schematically shown in Fig. 2.2.1. The reaction of pure elements is currently an active research topic, e.g. for multilayer systems, and an overview about this topic has been given by Tanguep Funamizou [21], Brennan [22] where both chemical reactions and diffusion of the atoms cause this layer formation [20] .

Definition of some terms

Vacancy mechanism:

At elevated temperatures atoms are oscillating around their average positions. Due to this oscillation atoms can jump from their current position in the crystal lattice with a certain probability depending on the oscillation strength to adjacent unoccupied lattice sites named vacancies. Smigelskas and Kirkendall [23] demonstrated the mechanism of vacancy diffusion.

a)

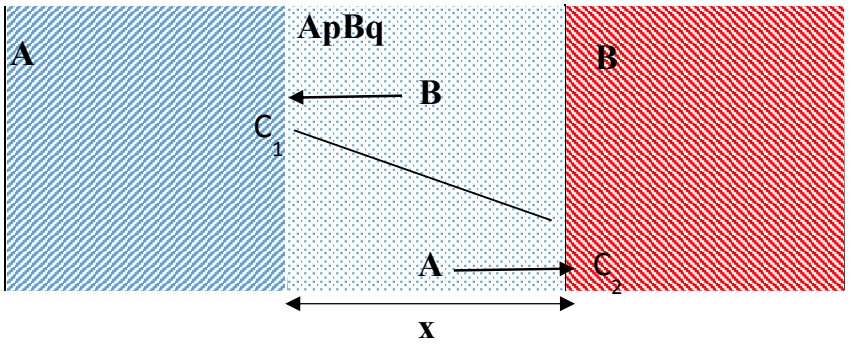

b)

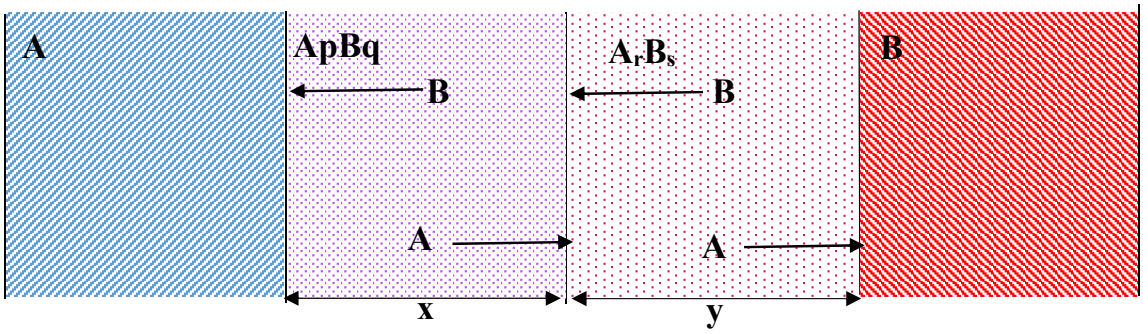

Figure 2.2-1: A schematic illustration of diffusion in the binary A B system. a) According to the phase diagram the compound A_pB_q is the first to form at the A-B interface (p and q are positive numbers) b) Later on A_rB_s (where r and s are positive numbers) starts to form at the A_pB_q – B interface. The thickness of the respective phases is given by x and y.

This vacancy mechanism is responsible for self-diffusion in pure metals as well as diffusion of substitutional solutes in alloy systems. In order to study self-diffusion a tagged atom, which is normally a radioactive isotope chemically identical to the matrix is used. In the case when the diffusing species is chemically different to the matrix the process is called impurity diffusion.

The trace diffusion of Al in Mg was studied by Brennan over the temperature range 573-673 °C and she suggested the expression below for the diffusion coefficient [22]:

$$D_{Mg}^{Al} = 3.9 \times 10^{-3} \exp\left(-\frac{155\text{kJ}}{\text{mol}}/RT\right) \frac{\text{m}^2}{\text{s}} \qquad \text{Equation 2.2-2}$$

It is also known that diffusion of Al in the Mg lattice is anisotropic and that diffusion of Al along the c-axis is 1.3 times faster than in the direction of the a-axis. This is due to a higher energy barrier for atomic jumping along the a-axis than the c-axis [24].

Fujikawa [25] studied the diffusivity of Mg in Al over the temperature range 325-650 °C using a carrier-free radioactive Mg specimen and proposed the equation:

$$D_{Mg/Al}=(0.0623\begin{pmatrix}+0.0126\\-0.0103\end{pmatrix}\times\{\exp(1.19\pm0.0012)(1.60*10^{-19}\text{kJ/kT}\}\frac{cm^2}{s} \qquad \text{Equation 2.2-2}$$

Interdiffusion:

In a binary system interdiffusion between species A and B is described by an effective interdiffusion coefficient. The rate of diffusivity for each element in the binary system is called the intrinsic diffusion. A heterogeneous phase transformation is divided in many publications and in the literature into two categories. Firstly, a diffusive nucleation and growth mechanism and secondly a martensitic transformation, which is a diffusion-less transformation and happens by co-operative movements of many atoms. In the diffusive transformation, atom-by-atom transformation at the interface boundary results in growth. This kind of boundary is regarded as glissile. In the case of a non-glissile boundary, the rate of grain boundary growth is categorized by phase transformations in the vicinity of the interface. One can assume that this kind of interface is stepped on an atomic scale and migrates by the movement of the steps. The long-range transport of the atoms causes motion of the interface, which is a result of diffusion. In principle, two types of migrating interfaces can be identified. Firstly, there is a very slow moving boundary, the motion of which is largely independent of the diffusion rate, the growth is described as interface controlled. Secondly, a very highly mobile boundary, which moves as rapidly as the rate of diffusion allows. The growth rate then is determined, almost completely by diffusion and categorized as diffusion controlled. The driving force for an interface controlled mechanism is the difference in the free energy per

atom for the atoms in the opposite sides. From a mathematical point of view when one defines both the growth rate as G and r as a linear dimension with t as time, then the growth can be defined as $G=\frac{dr}{dt}$. When G is constant, the growth is linear with time and the transformation is interface controlled. In the second case, G is proportional to $\sqrt{t}$ and it can be categorized as diffusion controlled [26].

2.3 Crystal structure of Mg

Mg has the atomic number 12. Its lattice parameters are $a_1 = a_2 = 3.21$ Å, $c = 5.21$ Å with the angles $\alpha = \beta = 90°$, $\gamma = 120°$. This result in an axis ratio c/a=1.623, which makes Mg under atmospheric pressure having a perfectly hexagonal close-packed (HCP) crystal structure with the space group P63/mmc. Mg has, due to its crystal structure anisotropic properties [27] and the atoms are situated at (0, 0, 0) and (1/3, 2/3, 1/2) (see Figure 2.3-1). HCP crystal structures have the atomic packing factor 0.74 and the coordination number 12. The empirical atom radius of Mg is 1.5 Å and the calculated one is 1.45 Å. The planes and directions of Mg crystal are shown on the Figure 2.3-2.

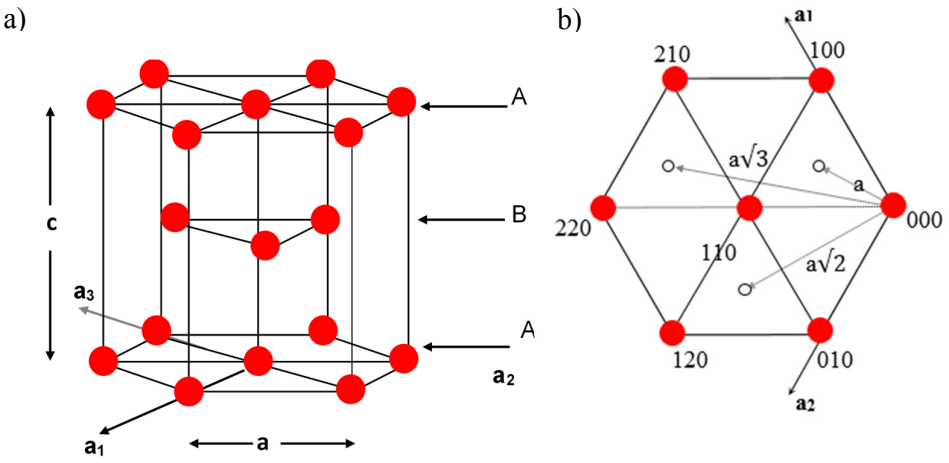

Figure 2.3-1: (a) Hexagonal close-packed structure and (b) atom positions in projection of the basal plane.

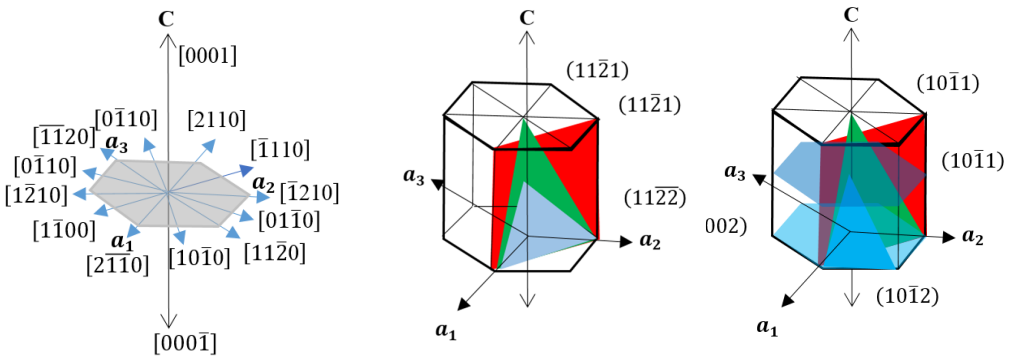

Figure 2.3-2: The directions and planes in the magnesium unit cell [28].

2.3.1 Stacking faults in Mg

Stacking faults (SF) are planar defects enclosed by partial dislocations. The forming process or annealing can lead to the occurrence of SF. Stacking faults are important since they control some deformation processes like work hardening, twinning, ease of climb and cross slip.
A lower stacking fault energy results in a higher activation energy for these processes. In Mg three principal stacking faults can form:

a) extrinsic stacking faults indicated with E, which occurs when an extra layer of atoms is introduced and is described by the sequence:…ABABCABAB
b) intrinsic stacking faults indicated with I and described by
    1. I_1 when stacking sequence '…ABABCBCB…' is produced and
    2. I_2 when stacking sequence '…ABCACAC…' is produced and
c) Twin-like stacking fault T'…ABABCBABABA…'.

It has to be noted that the extrinsic type stacking fault is not energetically favorable [29]. Pure Mg has the stacking sequence 'ABAB…'.

2.4 Crystallographic indexing

The crystallography of cubic structures like BCC and FCC can be described by using 3 indices Miller notation (hkl) [uvw]. For the HCP crystal structure using Miller indices causes discrepancies since similar planes are given quite different indices. To avoid confusion, the Miller-Bravais notation is used for the HCP crystal structure. The Miller-Bravais notation is based on the unit vectors a_1, a_2, a_3 and c. The crystallographic directions are given by (h k i l) and crystallographic planes by [u v t w] (see Fig. 2.3.2). The third index can be determined through the mathematical equation presented below:

$$\begin{bmatrix} h \\ k \\ i \\ l \end{bmatrix} = \begin{bmatrix} H \\ K \\ -H-K \\ L \end{bmatrix}$$

$$\begin{bmatrix} u \\ v \\ t \\ w \end{bmatrix} = \frac{1}{3}\begin{bmatrix} 2U-V \\ 2V-U \\ -U-V \\ W \end{bmatrix} \qquad \text{Equation 2.4-1}$$

2.5 Deformation mechanism of Mg

Slip system in Mg:

First Taylor [30] and later on von Mises [31] suggested that for a polycrystalline material undergoing a homogeneous deformation without brittle rupture and crack initiation it is necessary that five independent slip systems are activated. The slip systems are defined by the movement of dislocations through applied stress. The common slip systems in hexagonal metals were described firstly in [32] see Table 2.5-1 and Figure 2.5-1.

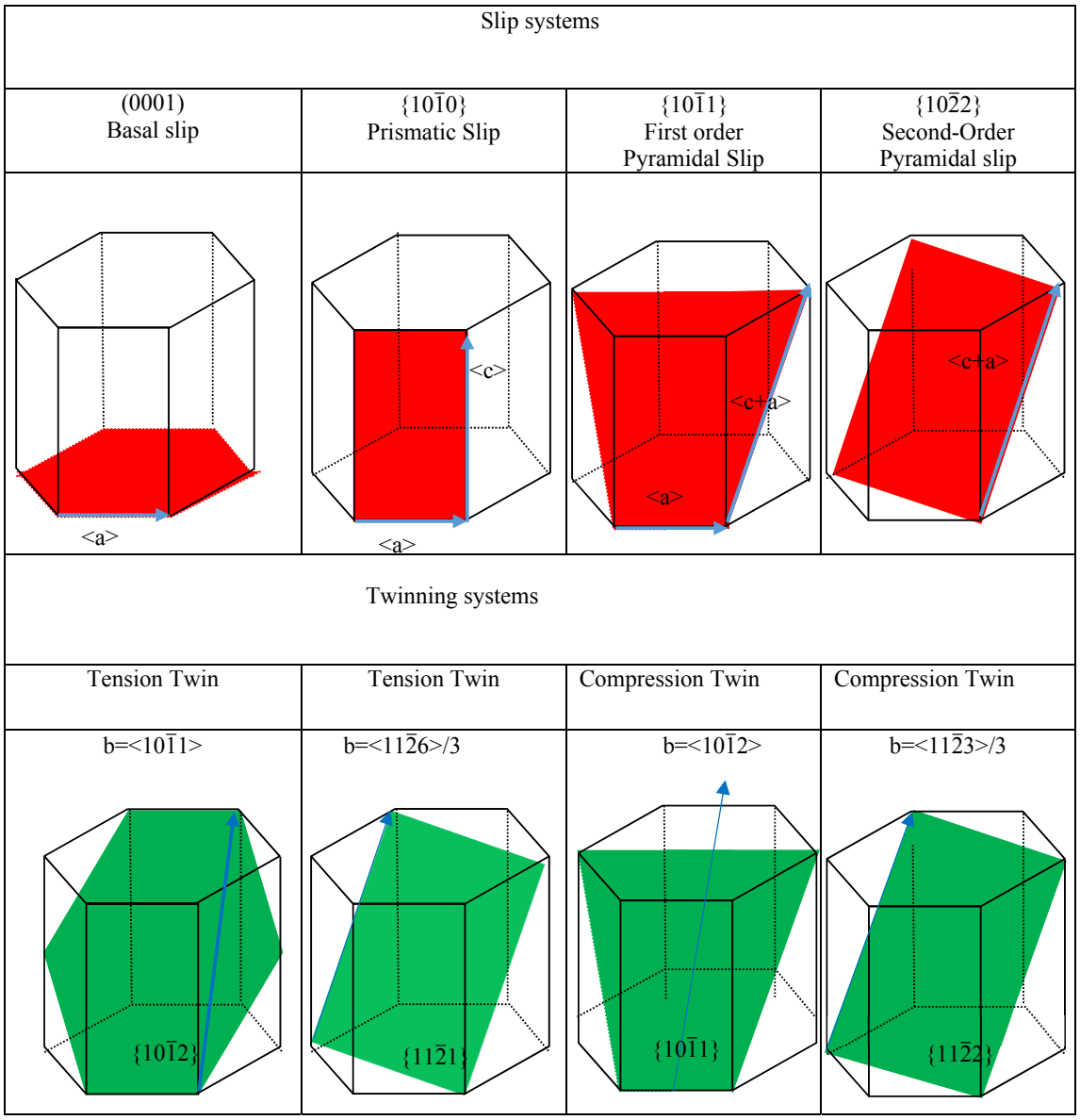

Figure 2.5-1: Important crystallographic planes and directions in HCP crystals, in relation to the active deformation systems.

Table 2.5-1: Slip systems in hexagonal metals [32].

Slip systems	Burgers Vector	Number of slip systems	
		Total	Independent
{0001}<11$\bar{2}$0>	a	3	2
{00$\bar{1}$0}<11$\bar{2}$0>	a	3	2
{00$\bar{1}$1}<11$\bar{2}$0>	a	6	4
{11$\bar{2}$2}<11$\bar{2}$3>	<c+a>	6	5
{10$\bar{1}$0}<0001>	c	3	2
{11$\bar{2}$0}<0001>	c	3	2

2.6 Dislocations in Mg

Dislocations with the Burgers vector b = 1/3 <11$\bar{2}$0>, the so called <a> dislocations, enable deformation on the basal plane, while those with the Burgers vector <c> = <0001> are responsible only for deformation along the c axis. The dislocations with b = 1/3 <11$\bar{2}$3>, the so called <c+a> dislocations, have deformation components along both the c and a axes. From the energetic point of view, the <a> dislocations are the most favorable and the <c+a> dislocations are the most unfavorable as they have the longest Burgers vector. Which dislocations are really activated during deformation is dependent on the planar density of each crystallographic plane. The main factors are the c/a-ratio and the possibility of dissociation into partial dislocations. Some related Burgers vector are listed in Table 2.6-1 using the notation of Thomson tetrahedron (see Fig 2.6-1) [32].

Table 2.6-1: list of dislocations in Mg [32].

Type of dislocation	*Total number of dislocations per unit cell*	*Direction indices (Miller-Bravis)*	*Magnitude of vector*	*Relative energy of dislocation*
Perfect dislocations				
1) AB, <a>	6	$1/3 <11\bar{2}0>$	|a|	$\|a\|^2$
2) ST (TS), <c>	2	<0001>	|c|	$\|c\|^2=8/3\,\|a\|^2$
3) ST+AB, <c+a>	12	$1/3 <11\bar{2}3>$	$\sqrt{\|a\|^2+\|c\|^2}$	$11/3\|a\|^2$
Imperfect dislocations				
4) Aσ, Bσ	6	$1/3 <10\bar{1}0>$	$\|a\|/\sqrt{3}$	$1/3\|a\|^2$
5) σS	4	1/2 <0001>	|c|/2	$2/3\|a\|^2$
6) AS	12	$1/6 <20\bar{2}3>$	$\sqrt{\|c\|^2/4+\|a\|^2/3}$	$\|a\|^2$

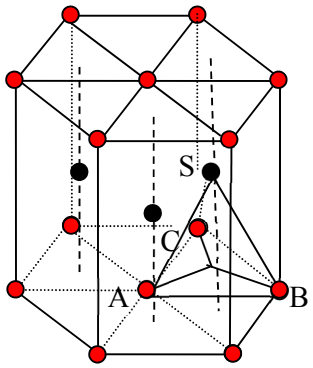

Figure 2.6-1 Description of Burgers vector in the HCP structure based on Thomson tetrahedron [32, 33].

As mentioned above, a dislocation can be moved when the applied stress has reached a critical value. For a uniaxial tension or compression, the shear stress τ acting on a specific crystallographic plane in a crystallographic direction is defined as below:

$$\tau = \sigma \sin \alpha_a \cos \beta_a \qquad \text{Equation 2.6-1}$$

where α_a is the angle between the slip plane normal and tensile axis and β_a is the angle between the slip direction and tensile axis.

If τ exceeds the critical resolved shear stress (CRSS) for a specific slip system dislocations move on this slip system. Another parameter is the Schmid factor defined by m

$$m = \sin \alpha_a \cos \beta_a \qquad \text{Equation 2.6-2}$$

which presents the ease of slip with respect to the orientation of the respective crystal. For a single crystal, the resolved shear stresses can be easily calculated from the external applied stresses.

For a polycrystalline material plastic deformation will occur when shear on certain crystallographic planes reaches the CRSS value.

The poor room temperature formability of Mg is related to the low amount of active slip systems in Mg at ambient temperature. The basal <a> slip, corresponds to slip on the closest packed direction $<11\bar{2}0>$, and is the easiest direction of slip in Mg like in many other HCP metals. The closest packed $<11\bar{2}0>$ direction also lies within other prismatic $\{10\bar{1}0\}$ and

{10$\bar{1}$1} planes. Another slip system in Mg is the <c+a> slip system, where the dislocations have a Burger vector of 1/3 <11$\bar{2}$3> and glide on the {11$\bar{2}$2} pyramidal plane. However, the activation of <c+a> slip has a higher CRSS.

Therefore, activation of other slip systems or twinning is required to undergo a plastic deformation. It should be noted that each slip system has its own CRSS value and the orientation of the crystal also plays a role.

2.7 Other deformation mechanism active in Mg

2.7.1 Twinning

Twinning is another conventional deformation mechanism in Mg and materials with a HCP crystal structure. Generally, when parts of crystals via a shear deformation are shifted and mirrored with reflections of each other with respect to a certain plane, then one can conclude that deformation has occurred by twinning. In Figure 2.7-1 one can see a visualization of the twinning mechanism with two shear planes k_1 k_2, which remain undistorted during deformation and two directions from the intersection of these planes, namely η_2 and η_1. Twinning is a very important deformation mechanism in Magnesium.

The {10$\bar{1}$2} <10$\bar{1}\bar{1}$> tension twinning and the {10$\bar{1}$1} <10$\bar{1}\bar{2}$> compression twinning are frequently observed. The {10$\bar{1}$2} <10$\bar{1}\bar{1}$> tension twinning reorients the grains by a ≈ 86º rotation about a <1$\bar{2}$10> axis, while compression twinning feature a ≈ 56º rotation about a <1$\bar{2}$10> axis. Generally, compression parallel to the basal plane and tensile stress perpendicular to the basal plane favors {10$\bar{1}$2} twinning. At ambient temperature, {10$\bar{1}$2} twinning is the mechanism that results in the texture changes in c-axis direction [34]. Besides {10$\bar{1}$2} twinning, {10$\bar{1}$1} twinning is also a common deformation mechanism and provides a compression along the c-axis direction but requires a higher stress to be activated. {10$\bar{1}$3} twinning is another common deformation mechanism. All common twinning mechanisms in

Mg are listed in Table 2.7-1. In some cases the shear produced by twinning is not sufficient to create the correct twinned crystal for which additional small movements of atoms are required, which is called atomic shuffling.

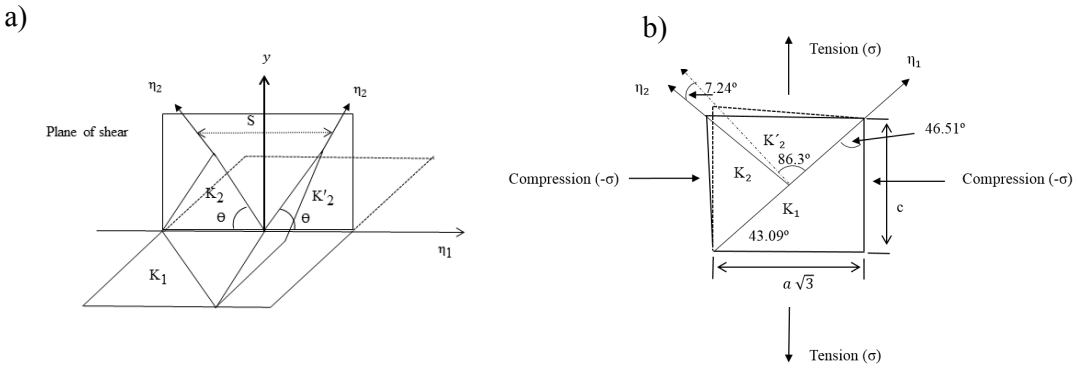

Figure 2.7-1 a) A schematic illustration of the crystallographic elements of twinning. b) The activated twinning mechanism in Mg by $\{10\bar{1}2\}$ twinning [32].

Table 2.7-1 The common twinning system in Mg and the related shear amount and complexity of atomic shuffling (q).

K_1	K_2	η_1	η_2	S	q
$\{10\bar{1}2\}$	$\{\bar{1}012\}$	$<10\bar{1}\bar{1}>$	$<\bar{1}01\bar{1}>$	0.130	4
$\{10\bar{1}1\}$	$\{10\bar{1}\bar{3}\}$	$<10\bar{1}\bar{2}>$	$<30\bar{3}\bar{2}>$	0.137	8
$\{11\bar{2}1\}$	(0001)	$<11\bar{2}\bar{6}>$	$<11\bar{2}0>$	0.616	2
$\{11\bar{2}2\}$	$\{11\bar{2}\bar{2}\}$	$<11\bar{2}\bar{3}>$	$<22\bar{4}3>$	0.260	6

Sometimes, twinning is accommodated by another twinning system and this mechanism is named double twinning. Double twinning has been described when $\{10\bar{1}1\}$ or $\{10\bar{1}3\}$ has occurred and made the twinned plane ideal for $\{10\bar{1}2\}$ twinning.

Generally, twinning is described as a mechanism which will be activated when the amount of plastic shear is small, and the material experiences uni-directional stresses. The CRSS value which is described before, is also important for the activation of twinning but also the microstructure and grain size of the material and the applied stress state play a role. In general, the amount of shear and atomic shuffling, which is described as small amount of movements of atoms in HCP crystals after the rotation of the HCP crystals has occurred due

the twinning. The twinning process is generally divided in two stages, twin nucleation and twin growth.

In comparison to materials with FCC and BCC crystal structures in Mg and other HCP crystals twinning is a much more frequent deformation mechanism.

2.7.2 Latent hardening

Latent hardening is defined as hardening of a slip/twinning system by another active system. As described above, twinning produces rotation of the crystallographic planes and can make it easier or harder for another deformation mechanism to be activated which is called composite effect [35].

2.7.3 Kink banding

Kink banding is defined as the cooperative motion of dislocations that leads to arbitrary reorientations of the crystal lattices along the kink boundaries. Kink banding is a favorable mechanism in Mg and mostly observed in single crystals of Cd and Zr. It was observed that some intermetallic phases like NiAl also undergo kink banding. This mechanism was also observed in layered structural materials like laminated composites [35].

2.8 Crystal structure of Al

Aluminum has a face-centered cubic crystal structure with a close- packed cubic lattice and the atomic packing factor 0.74. The close-packed planes are stacked ABCABC instead of ABAB as for the HCP structure. The atomic radius of Al is 1.43 Å with a metallic bonding of the crystal structure, which is stable over the whole temperature range up to the melting point. The unit cell has a coordination number of 12, and the closest distance between two atoms is 2.863 Å at room temperature while it is 3.19 Å for Mg, which is 12% larger than for Al. Figgins et .al [36] determined the lattice parameter of Al with a purity of 99.99% to be

a=4.04963 Å at 25 ℃, which is in good agreement with Straumanis [37]. The empirical atomic radius of Aluminum is 1.25 Å and the calculated one is 1.18 Å.

2.9 Deformation mechanisms of Al

As discussed in section 2.5 the slip systems are directly related to the crystal structure and the specific slip systems have a certain CRSS value, which is the critical resolved stress value to move the dislocations. Like for the HCP crystal structure, in the FCC crystal structure plastic deformation is accommodated by slip or twinning. Twinning causes abrupt changes of the crystal orientation distribution, while slip aligns the crystals along the tensile or compression axis. The slip systems in FCC, as illustrated in Figure 2.9-1, are {111} <110> and the twinning system {111} <112>. In an FCC material like Aluminum, the 12 slip available slip systems are sufficient to fulfil the von Mises [31] criteria. Taylor [30] also predicted which slip system is selected for a certain crystal orientation with respect to the deformation geometry, and based on the activated slip systems the resulting texture can also be predicted [38].

Another important factor dictating the mechanism of plastic deformation is the stacking fault energy (SFE). The texture of FCC metals are divided in two categories, based on their SFEs: metals with a high stacking fault or low stacking fault energy. Al has a high stacking fault energy and therefore the resulting texture in the case of plain strain deformation is called the copper-type texture.

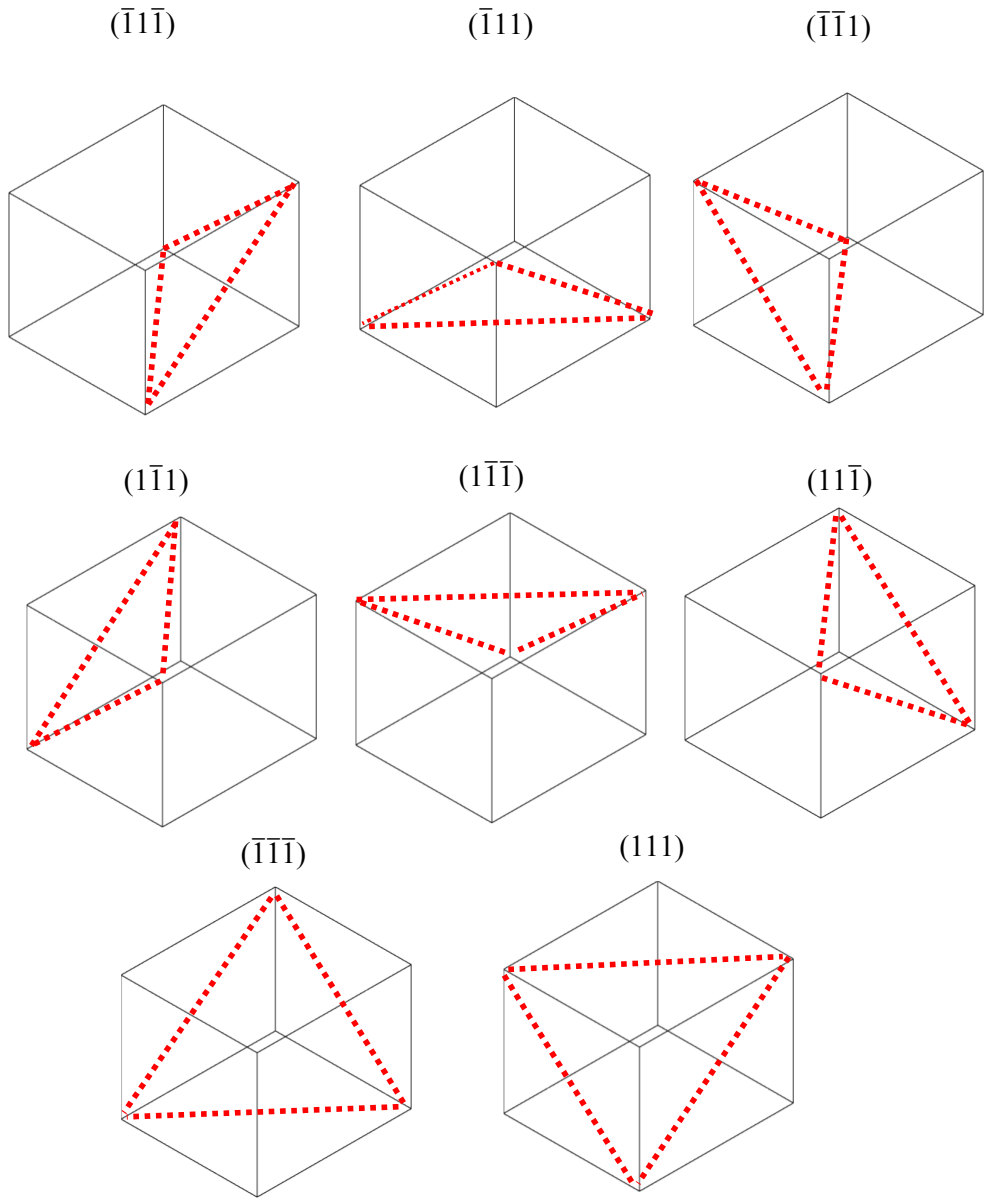

Figure 2.9-1: The (111) planes in FCC system

The copper-type texture consists of an orientation tube, which begins with the C (Copper) through the S component and ends at the Bs (Brass) texture component. With increasing degree of deformation the texture intensity increases. In the case of uni-axial deformation a double fibre texture with <111> major and minor <100> fiber texture along the elongation direction can be formed. As mentioned the number of slip systems in FCC metallic materials is higher than 5 and this may cause difficulty in recognizing the active glide systems. Through simulation models like the “relaxed constraints” or the Grain Inter-Action“GIA” model the

active slip systems [39] can be predicted. As an example the active slip systems in a rolled sheet for a β-fibre in the stereographic projection for {111} slip planes are illustrated in Figure 2.9-2. As can be seen, for the Cu orientation only four slip system are active. For the Brass orientation results, only two systems, A1 and B1, are activated. The S orientation forms when two additional slips systems, A2 and B2, are activated. In addition to the nature of the crystal structure, which determines the mode of slip systems, other important parameters are the form of the strain induced due to the applied stress in the material and its magnitude. Alloying is also another important factor, which due to altering the SFE can change the type of texture formed. A further important parameter is the temperature during the induced deformation.

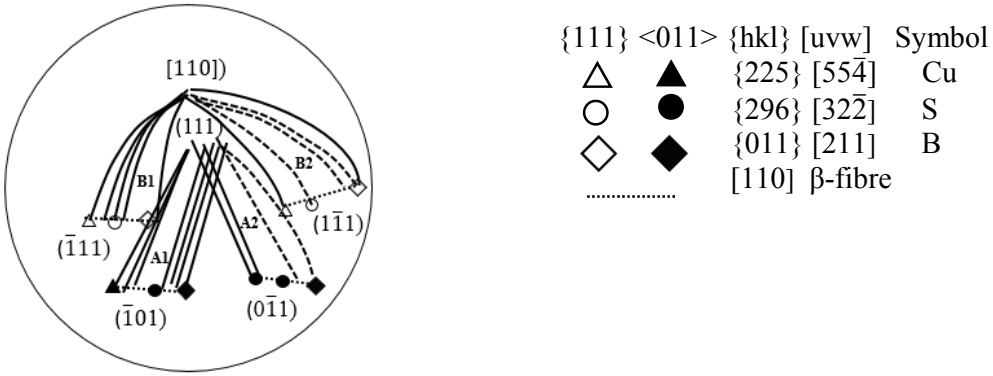

Figure 2.9-2: the active slip systems during plane strain deformation in FCC metals. (A1) and (A2) two coplanar slip systems (111):[$\bar{1}$01] and (111):[0$\bar{1}$1] respectively. (B1) and (B2) two co-directional slip systems with (211)[110] and (111)[110] respectively [39].

2.9.1 Dislocations in Aluminum

In order to understand the dislocation mechanisms in Aluminum there is a need to understand the nature of the microstructure in FCC metals. In FCC metals the grains are subdivided into the mesoscale and microscale (see Figure 2.9-3). Mesoscale grains include the deformation bands and microscopic scales grains include cell blocks and cells. Hansen et al [40] categorized three type of boundaries, which can form in FCC materials.

1. When the DDWs (dense dislocation walls) are aligned to the trace of the slip planes
2. When the DDWs show no alignment with the {111} planes

3. When there are no boundaries and the cells are in the same direction.

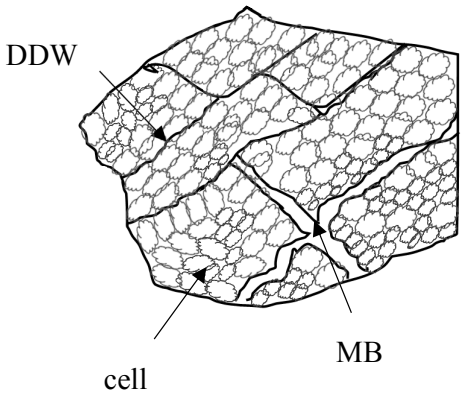

Figure 2.9-3: Representation of DDWs and MB and the cell structure. MB indicates the Microbands [41].

2.9.2 Shear bands in Aluminum

Shear bands are another important microstructural feature in FCC metals. Shear banding is activated when homogenous dislocation slip is activated by high plastic deformation [42]. The walls and cell blocks are the typical microstructure obstacles for a material with high SFE, like Aluminum. The effect of shear banding on the resulting crystallographic texture of high SFE materials after deformation is categorized by a copper-type texture. The resulting crystallographic components are described by the {112}<111> copper component with {123}<634> (S) components and the {011}<100> Goss texture components [42].

2.10 Crystal structure of the Al_3Mg_2

The first intermetallic phase, of which there is no doubt about its existence in the binary Al-Mg system is the Al_3Mg_2 phase, known as the β-phase. It can be formed over the 60-62.5at.% Al. It belongs to the group of structurally complex metallic alloy phases (CMAs), which are characterized by a long lattice period consisting of several hundred or thousands of atoms per unit cell. Investigating the Al_3Mg_2 phase is not only important because of its crystal structure, but also because it has certain physical properties like superconductivity [43] and a low

specific weight ratio [44]. Moreover, due to its crystal structure it has the potential to be used as a hydrogen storage and a thermoelectric material. Some other intermetallic phases like Cu_4Cd_3 and $NaCd_2$ have the same crystal structure as the β-phase. Therefore studying the kinetic formation of the β-phase can help to obtain a better understanding of their formation kinetics as well. The existence of the β-phase in the Al-Mg system was first discussed by Riederer [45]. He used a powder diffraction method and suggested a hexagonal structure with a= 11.38 Å and c = 17.99 Å that consisted of eight formula units with the chemical composition Al_8Mg_5 per unit cell [45]. Later on Laves and Möller [46] suggested that the β-phase was an isomorphous crystal structure with the Cu_4Cd_3 structure. Perlitz [47] presented a cubic structure for the β-phase with the space group Fd3m (O7h) with 1166 atoms per unit cell with a= 28.22 Å and the chemical composition Al_3Mg_2. Samson [48] with the help of three dimensional least square techniques investigated many details of the Al_3Mg_2 structure and proposed a cubic crystal structure with the space group Fd3m and a =(28.239 ± 0.001) Å. He suggested [48] there are approximately 1168 atoms in the unit cell, which are distributed over 23 crystallographically different positions and the 23 crystallographic different atoms produce 41 different polyhedral structures. It is also known [44] that at 214˚C the Samson phase [6] undergoes a structural phase transition to a rhombohedral phase identified as β'. This β' phase has the space group R3m, which is a subgroup of Fd3m and has no inversion symmetry. Its lattice parameters are a= 11.9968 Å and c =4 8.9114 Å. The crystal structure of the β and β' Samson phases were recently reinvestigated by Feuerbach et al. [49]. They verified many details of the crystal structure published by Samson [48].

Of the 1168 atoms in the Samson structure, there are 528 aluminum and 351 magnesium atoms, which are distributed over 1832 positions with the SOF = 1 (SOF= site occupancy factor). The remaining 289 atoms take incompletely the unoccupied 953 positions with the SOF=0.3. Al atoms form 22 layers with the sequence ABC and these atoms with SOF equal to

0.3 form a cluster in between as can be seen in the Figure 2.10-2. The unit cell of A_3Mg_2 is presented in the Figure 2.10-1.

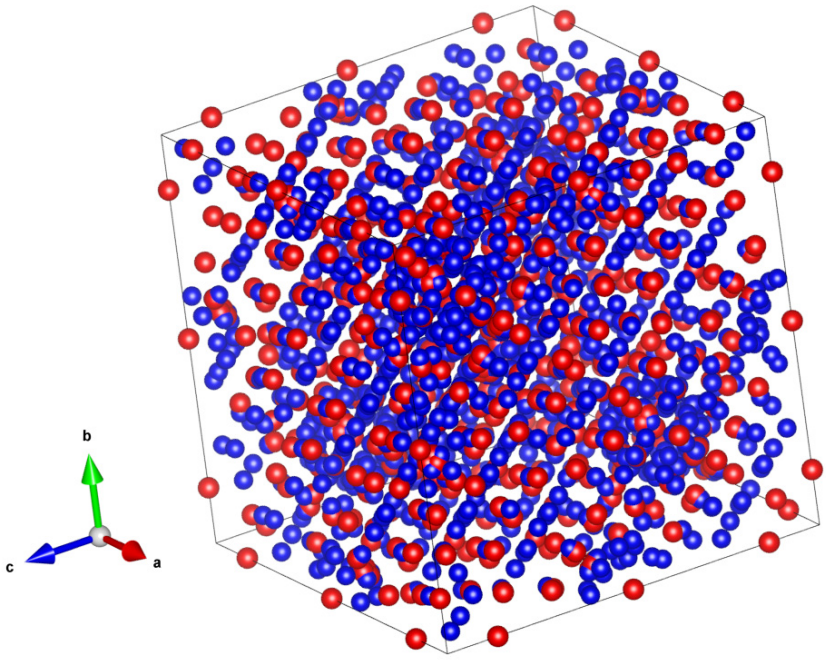

Figure 2.10-1 The unit cell of Al_3Mg_2 (β-phase) red spheres represent Mg atoms and the blue one Al atoms.

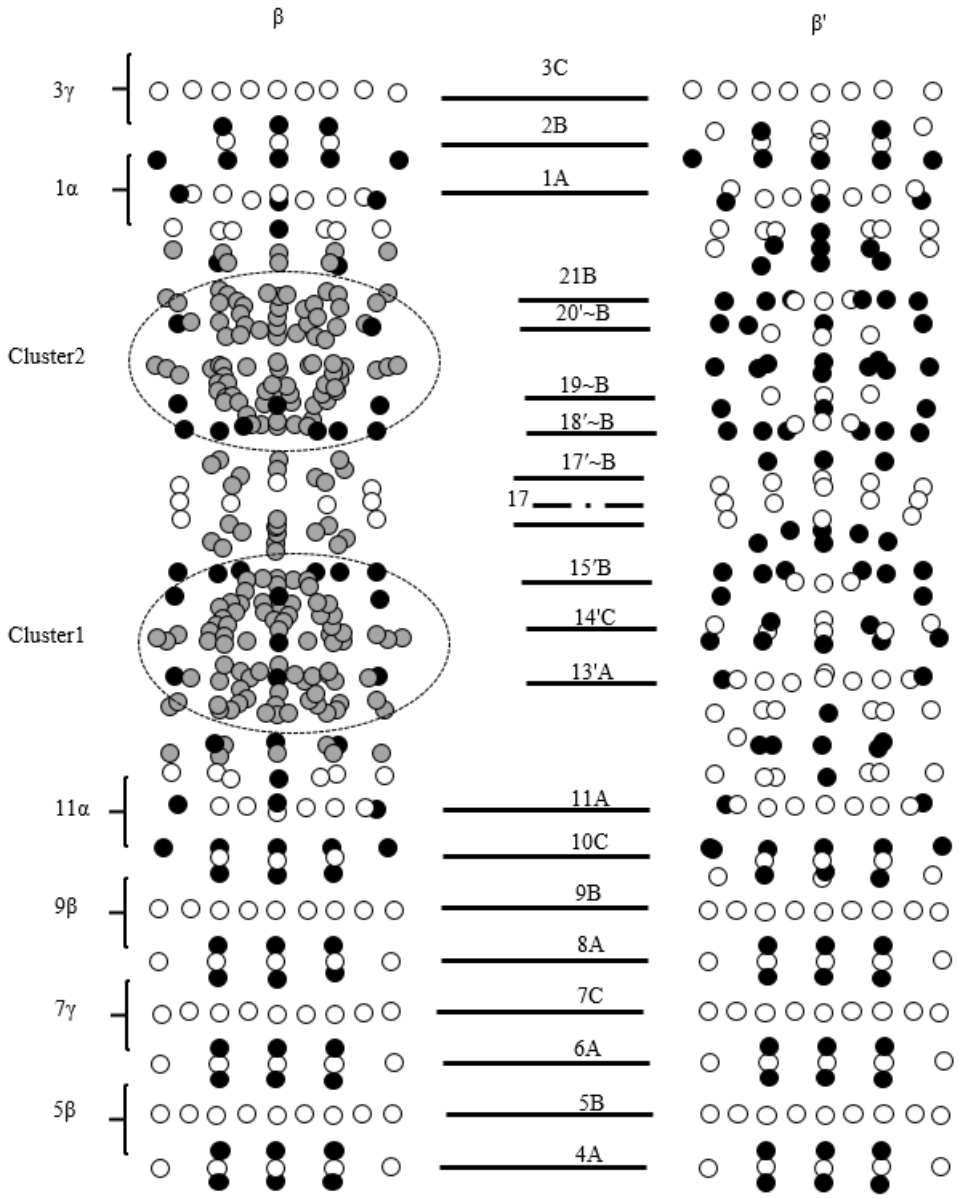

Figure 2.10-2: Schematic representation of the β and β'crystal structures, modified image based on [50]. Open circles represent Al and the black one Mg atoms. Black and white indicate atoms with SOF=1 and the gray circles indicate atoms with SOF=0.3.

A simplified representation of the crystal structure of Al_3Mg_2 was proposed by Wolny [50] as can be seen in Figure 2.10-2. They named the atomic layers using ABC and other more complex multilayer structures using the symbols α, β and γ. The B layers are incompletely occupied with Al atoms (see Figure 2.10-3). In both β and β', the sequence of the layers is

1α2B3γ4A5β6A7γ8A9β10C11α. In these sequences, there are gaps. When the gaps are occupied with Mg atoms due to its bigger size the layers are shifted very slightly.

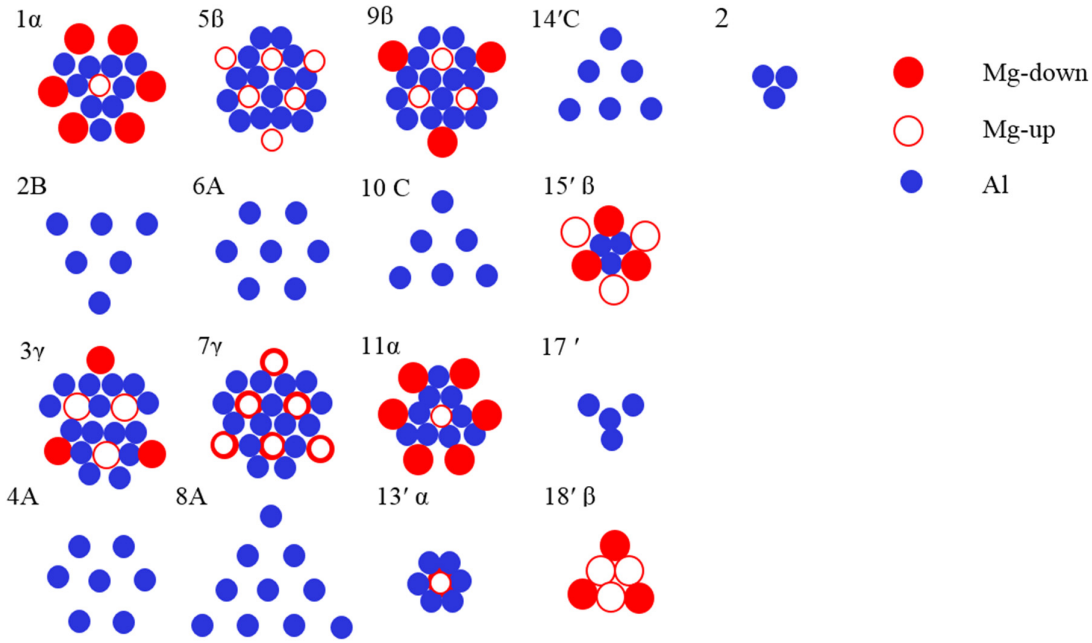

Figure 2.10-3: Cross section of the Al_3Mg_2 crystal structure showing individual layers, modified from [50].

In the ideal form, the Al_3Mg_2 phase can be considered as a combination of five Friauf polyhedra (see Figure 2.10-4) [46].

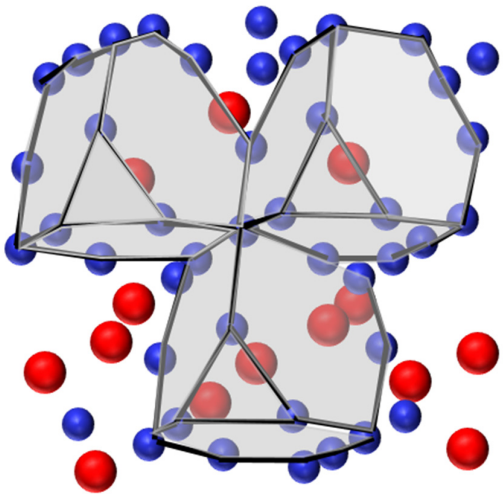

Figure 2.10-4: Ideal crystal structure of Al_3Mg_2 [50].

In this case, if the entire space was filled with these five Friauf polyhedra then the atomic ratio between Mg and Al should be 2:1, however the measured ratio is 3:2. This indicates that there is a lower occupancy of Mg atoms in the crystal structure than expected. It should be noted that the actual stoichiometry of the experimental investigated crystal structure is $Al_{61.5}Mg_{38.5}$. In the ideal model illustrated above, 1192 atoms for the crystal structure are present, although, in the calculation of the Wycoff positions, 1832 atoms were obtained. This difference shows that only two thirds of the positions are occupied with atoms. Feuerbach et.al [49] suggested that the crystal structure of Al_3Mg_2 arises through structural disorder rather than missing atoms and therefore proposed a diamond structure with a space group number CF1168. For the β-phase they also suggested the volume $V_{at}^{Al3Mg2} = 19.26$ Å^3, where Al has $V_{at}^{Al} = 16.61$ Å^3 and Mg has $V_{at}^{Mg} = 23.24$ Å^3.

2.11 Crystal structure of the $Al_{12}Mg_{17}$ phase

The $Al_{12}Mg_{17}$ phase has some technological importance, i.e. in some important Al-Mg alloys like AZ91 it is used as a precipitate phase to increase the strength of the alloys or it can be used as a hydrogen storage material. The existence of the γ-$Al_{12}Mg_{17}$ phase was first discussed by Laue et al. in 1934 [51]. At that time this phase was called Al_2Mg_3 and 4 atom

positions were suggested (see Figure 2.11-1, Figure 2.11-2 , Table 2.11-1 and Table 2.11-2) namely i)2a ii) 8c: x=0.317 y=x, z=x iii) 24 g1: x= 0.356 ,z= 0.042 iv) 24g: x= 0.089, y=x z= 0.278 [52]. Laves et al. [51] compared theoretical and experimental results and suggested that this phase should have the formula $Al_{12}Mg_{17}$ and the same crystal structure as α-Mn with 58 atoms and a lattice constant a = 10.54 Å. The structure of α-Mn was first suggested by Bradley and Thwelis in 1972 [52]. The crystal structure they suggested for α-Mn was a cubic body-centered crystal structure with a space group $\bar{I}43m$ with 58 atoms occupying the four existing positions. The Strukturbericht symbol for α-Mn is A12. Later on, Frank and Kasper in 1959 [53] categorized $Al_{12}Mg_{17}$ as a Frank-Kasper phase. Recently, Joubert [54] using the Rietveld method and Calphad calculations investigated $Al_{12}Mg_{17}$ and some other intermetallic phases with the same crystal structure, which were categorized before as Frank Kasper phases namely χ-phase.

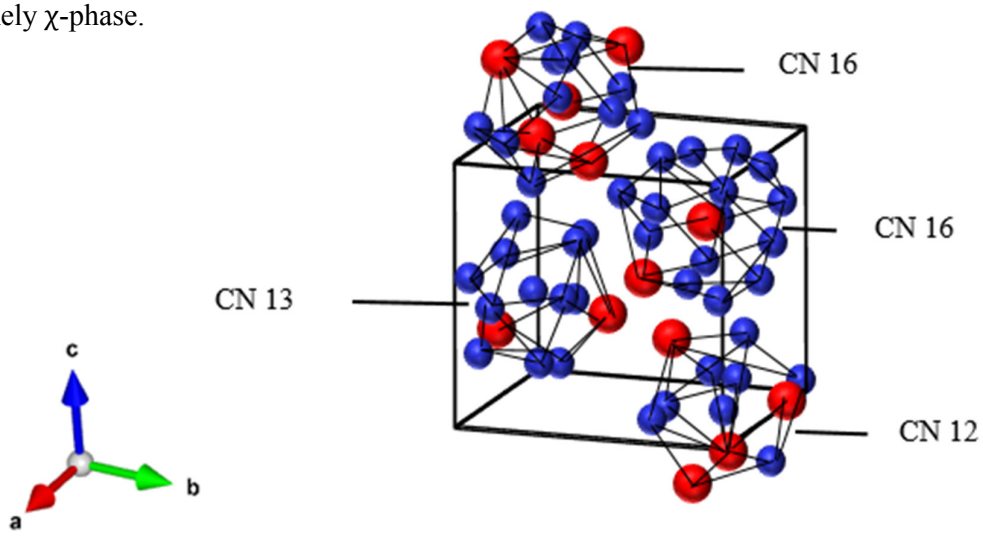

Figure 2.11-1: Crystal structure of the χ-phase ($Al_{12}Mg_{17}$), consisting of four polyhedra [54].

Table 2.11-1: The Wyckoff Positions and coordination number of the χ-($Al_{12}Mg_{17}$) phase [54].

atoms		X(position)	Y(position)	Z(position)	CN(coordination number)
Mg1	2a	0	0	0	16
Mg2	8c	0.32440	0.32440	0.32440	16
Mg3	24g1	0.35622	0.35622	0.03925	13
Al1	24g2	0.08996	0.08996	0.27681	12

Joubert et al. [54] also suggested that the shortest distance between two atoms is in the position 24g2 which is shorter than CN16 and CN12 (see Figure 2.11-2). The atomic distances depend on the CN rather than the size of the atoms, which means smaller atomic distances are associated with a lower CN and larger atoms distance prefer larger CN. They also suggested that the lattice parameters in the χ-phase ($Al_{12}Mg_{17}$) are a function of many factors including i) atomic radii of the two elements, ii) distribution of the elements on different sites, iii) the nature of the atomic bonding and iv) an intercorrelation between the coordination number and the lattice parameters. Their investigation shows that the χ phase must be categorized in three structure groups. Firstly, the α-Mn type, where a single atom occupies all atomic positions. Secondly, the A_5B_{24} type for which i_5RE_{24} is the prototype, where A indicates the sites with occupancy CN16 and B the remaining sites. Thirdly, the $A_{17}B_{12}$ type with the $A_2A_8A_{24}B_{24}$ crystal structure like the $Al_{12}Mg_{17}$ phase.

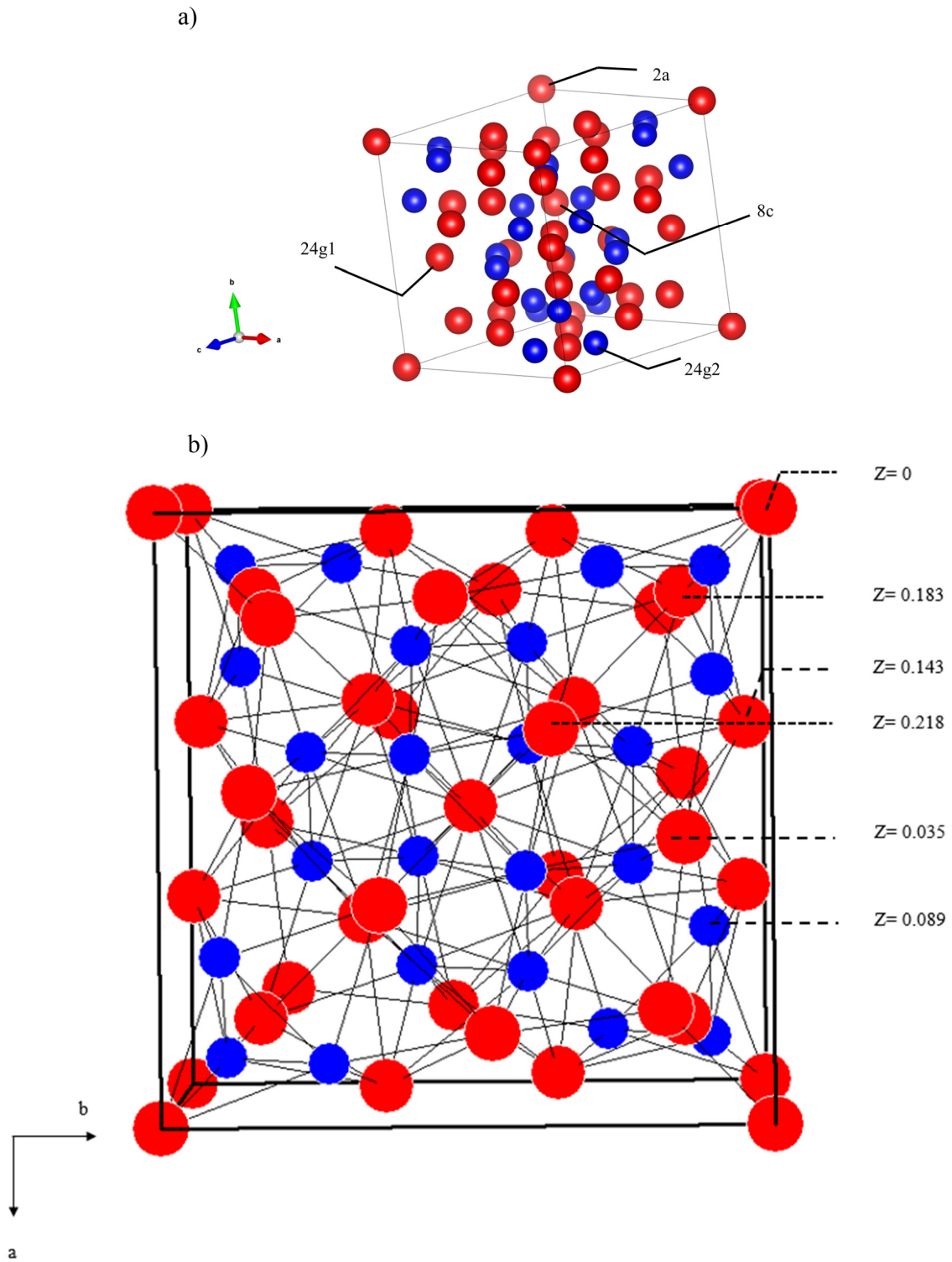

Figure 2.11-2: a) Crystal structure of the χ-phase ($Al_{12}Mg_{17}$). The 4 different atomic positions and the atomic sites are marked, b) projection along the a,b plane with the Z number between 0 and 0.218 [54].

Table 2.11-2: Atomic distances in the $Al_{12}Mg_{17}$ phase with respect to four atom positions [51].

-Mg in I (2a) point has the following neighbors:	4 Mg_{II} in distance of 3.34 Å 12 Al in distance of 3.21 Å
-Mg in point II (8a) has the following neighbors:	1 Mg_{I} in distance 3.24 Å 3 Mg_{III} in distance 2.96 Å 3 Mg_{III} in distance 3.50 Å 6 Al in distance 3.18 Å 3 Al in distance 3.42 Å
-Mg in point III (24g) has the following neighbors:	1 Mg_{I} in distance 2.95 Å 1 Mg_{II} in distance 3.50 Å 6 Mg_{III} in distance 3.16 Å 1 Al in distance 2.90 Å 2Al in distance 2.94 Å 2 Al in distance 3.15 Å
-Al in point IV (24g) has the following neighbors:	1 Mg_{I} in distance 3.21 Å 2.Mg_{II} in distance 3.18 Å 1Mg_{II} in distance 3.42 Å 1Mg_{III} in distance 2.90 Å 2Mg_{III} in distance 2.97 Å 2Mg_{III} in distance 3.15 Å 1Al in distance 2.65 Å 2Al in distance 2.82 Å

2.12 Crystal structure of the $Al_{30}Mg_{23}$ phase

The crystal structure of the $Al_{30}Mg_{23}$ phase was investigated very precisely, after30 years uncertainty, by Samson and Gordon [2]. The previous assessments refer to Kurnakov and Mikheeva [55], who suggested an Al_5Mg_4 crystal structure.

Samson and Gordon used three-dimensional least square techniques for the refinement of the crystal structure which they referred to $Al_{30}Mg_{23}$ [2]. They suggested that the ε-phase ($Al_{30}Mg_{23}$) consists of eight Friauf polyhedra, 24 icosahedra and 21 polyhedra (13 polyhedra L14, 2 L13 and 6 L1). As can be seen in Figure 2.12-1, the crystal structure at the center of $Al_{30}Mg_{23}$ consists of two Friauf polyhedra (F1). Each Friauf polyhedron (F1) shares three of

four hexagons with three light polyhedra (F2) and one hexagon with a dark Polyhedron (F1). Each polyhedra (F2) is connected to other light polyhedron (F2). Each Friauf polyhedron consists of two Mg atoms, Mg (1) and Mg (2), with different positions located on the threefold axis of the rhombohedron. b) 14 Friauf Polyhedra c)When Friauf polyhedral arranges along the rhombohedra unit cell. c) When polyhedral arranges along the threefold axis od the rhombohedron.

a b c

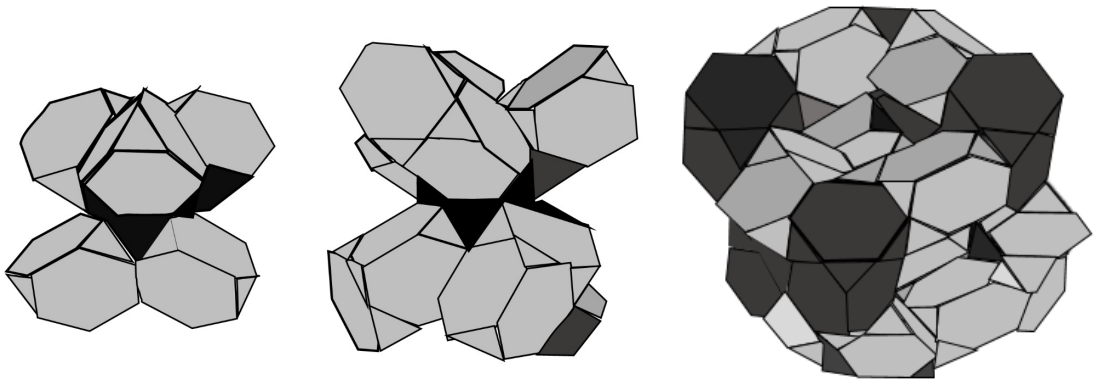

Figure 2.12-1: a)The arrangement of the F2 (light) Friauf polyhedra around the F1 (dark) [2].

d

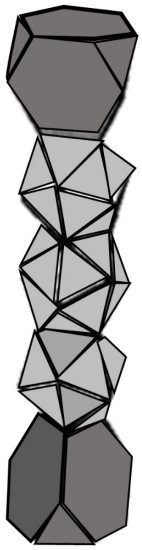

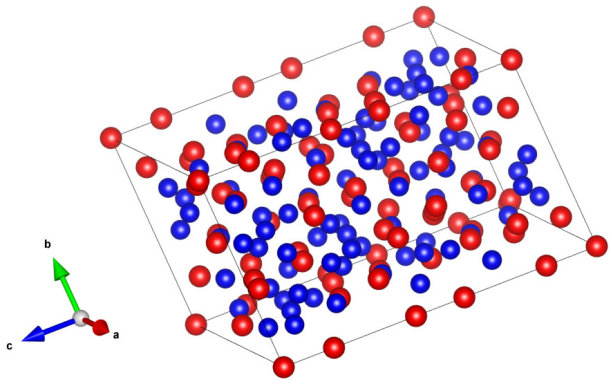

Figure 2.12-2 . The unit cell of $Al_{30}Mg_{23}$.The red circles indicating Mg atoms and the blue one the Al atoms.

In the suggested assessments by Samson and Gordon [2] the crystal structure has been described as rhombohedral with the R3 space group and a lattice parameter a = (10.3625 ± 0.0003) Å. The crystal structure consists of 53 atoms, which are distributed in 11 different crystallographic positions. As mentioned in Murray's assessments, a R-phase was suggested. Samson [2] suggested that the R- and ε-phases are isostructural and closely related structures. As mentioned above three intermediate phases certainly exist in the Al-Mg system, the β, γ and ε-phases. These phases all have in common that the crystal structure can be described by penetration of Friauf polyhedra with icosahedra. The transformation from γ to ε can be described as a result of Friauf polyhedra mode 1 to mode 3 transformation. The other interesting connection between the $Al_{12}Mg_{17}$ and $Al_{30}Mg_{23}$ phases is the general trend in valance electron concentration (VEC) which decreases from VEC = 2.57 for $Al_{30}Mg_{23}$ to VEC =2.41 for the composition range of $Al_{12}Mg_{17}$.

A summary of the phases present in the Al-Mg system is given in Table 2.12-1.

Table 2.12-1.The crystal structure, space group, and lattice parameters of possible

Phases	space group (Hermann-Mauguin) Pearson symbol International Tables number	Lattice parameter, A° (a, b, c)	References
Al	F m -3 m cF4 225	*a=4.04958*	Witt 1966[56]
Mg	P 63/m m c hP2 194	*a=3.20927* *c=5.21033*	Walker and Marezio, 1959 [7]
Al_3Mg_2 (β)	Fd-3 mm cF1832 227	*a=28.239(1)*	Samson 1965 [48]
$Al_{12}Mg_{17}$ (γ)	I -4 3 m cI58 217	*a= 10.5492*	Schobinger et al. 1970 [57]
$Al_{30}Mg_{23}$ (ε)	R-3 h hR53 148	*a=12.718* *c= 21.848*	Samson and Gordon 1968[2]

2.13 Orientation relationships in the phase transformation

Processing of engineering materials usually involves heat treatments which can result in phase transformations with one or more new phase being formed, which sometimes are called the product phase (p) or daughter phase.

Such phase transformations affect the properties and behavior of a material, firstly via the properties and morphology of the product phase, and secondly, via the orientation relationship (OR) between the parent and product phases. Knowledge of crystallographic phase transformations enables the control and design of the microstructure to obtain the required mechanical properties.

Phase transformations can be divided into two categories, namely diffusional and diffusionless phase transformation. Diffusion of phase transformations are often governed by a lowering of the interfacial energy and therefore with maximizing atomic matching across an

interface. Matching of close-packed or nearly close-packed rows of atoms at the interface is a condition that results in a minimum energy configuration and results in an orientation relationship due to the close packed or nearly close-packed directions being parallel [26]. The orientation relationship between the disappearing (parent) and the newly formed (daughter) crystals may deviate from the exact orientation relationship [58]. Although the orientation of the parent phase plays also an essential role in the formation of the daughter phase [58].

In case the parent material has a preferred orientation of its crystallite (texture), the newly formed phase may also have a texture. This is called texture transformation. The orientation relationship has some important industrial significance i.e. in the case of steel, where different orientation relationships have been proposed. The most known orientation relationships are the Wassermann and Bain [59] and Kurdjumov-Sachs (K-S) [60] relationships, which are observed in the martensitic γ to α transformation. In case of intermetallics within the Al-Mg binary system, the most well-known orientation relationship was reported by Nishiyama [61]. Having knowledge about the orientation relationship enables the prediction of the texture that forms [62].

An orientation relationship can be described in terms of the planes and directions of the parent and daughter phase, as described by (equation 5.9-1):

$\{hkl\}_p \| \{hkl\}_D$ Equation 2.13-1

$\langle uvw \rangle_p \| \langle uvw \rangle_D$,

when P indicates the parent and D the daughter phase.

Such orientation relationships can exist between HCP/BCC, FCC/BCC or FCC/HCP phases. The orientation relationship between Al and the β-Al_3Mg_2 phase has been described by Bernole et. al. [63] , as $[001]_\beta \| [001]_{Al}$ and $[110]_\beta \| [100]_{Al}$ as well as $(111)_\beta \| (001)_{Al}$ and $[110]_\beta \| [010]_{Al}$. In a study of the orientation relationships between the intemetallic phases formed in friction stir processed Al/Mg composites, Zhao et al. [64]

proposed that a cube-on-cube orientation relationship $(2\bar{2}2)_{\beta} \parallel (2\bar{2}0)_{Al}$, $(02\bar{2})_{\beta} \parallel (02\bar{2})_{Al}$, $(20\bar{2})_{\beta} \parallel (20\bar{2})_{Al}$, $[111]_{\beta} \parallel [111]_{Al}$ exists between Al and the β-Al_3Mg_2 phase.

The γ-$Al_{12}Mg_{17}$ phase has a BCC crystal structure and in the case of BCC/HCP, the orientation relationship between the phases has been investigated and calculated and eleven orientation relationships have been reported (see Table 2.13-1). In the system Al/Mg eight of the orientation relationships have been confirmed experimentally [65-68]. The three main orientation relationships are the Pitsch-Schrader [69], Crawley [65] and Burgers [70] relationships. Three other less important orientation relationships are Potter [71] [72], Porter [73] and Gjöness-Östmoe [74, 75]. All six of these orientation relationships are observed in the Al-Mg system after heating to an elevated temperature.

Table 2.13-1: Reported crystallographic ORs between a HCP and BCC phase.

Name	Crystallographic OR	References
Burgers OR	$(110)_{BCC} \parallel (0001)_{HCP}$, $[\bar{1}1\bar{1}]_{BCC} \parallel [2\bar{1}\bar{1}0]_{HCP}$	[68,70,76, 77,78]
Pitsch-Schrader OR	$(110)_{BCC} \parallel (0001)_{HCP}$, $[100]_{BCC} \parallel [2\bar{1}\bar{1}0]_{HCP}$	[72]
Crawley OR	$(111)_{BCC} \parallel (0001)_{HCP}$, $[\bar{2}11]_{BCC} \parallel [11\bar{2}0]_{HCP}$	[66, 67,68]
Gjöness-Östmoe	$(110)_{BCC} \parallel (0001)_{HCP}$, $[12\bar{1}]_{BCC} \parallel [2\bar{1}\bar{1}10]_{HCP}$	[76]
Potter OR	$(101)_{BCC}$ 2 ° from $(0001)_{HCP}$, $[11\bar{1}]_{BCC} \parallel [1\bar{2}10]_{HCP}$	[74-76,72]
Porter OR	$(110)_{BCC} \parallel (\bar{1}\bar{1}21)_{HCP}$, $[\bar{1}01]_{BCC} \parallel [01\bar{1}0]_{HCP}$	[66, 67,73]
Rong-Dunlop OR	$(021)_{BCC} \parallel (0001)_{HCP}$, $[100]_{BCC} \parallel [2\bar{1}\bar{1}0]_{HCP}$	[79]
OR8	$(101)_{BCC} \parallel (11\bar{2}0)_{HCP}$, $[\bar{1}\bar{3}1]_{BCC} \parallel [0001]_{HCP}$	[80]
OR9	$(4\bar{4}\bar{1})_{BCC} \parallel (0001)_{HCP}$, $[110]_{BCC} \parallel [2\bar{1}\bar{1}0]_{HCP}$	[81]
OR10(OR-A)	$(010)_{BCC} \parallel (0001)_{HCP}$, $[001]_{BCC} \parallel [2\bar{1}\bar{1}0]_{HCP}$	[82]
OR11(OR-B)	$(\bar{5}\bar{3}0)_{BCC} \parallel (01\bar{1}1)_{HCP}$, $[001]_{BCC} \parallel [2\bar{1}\bar{1}0]_{HCP}$	[82]

For the HCP/BCC system, two new orientation relationships have been suggested, namely [78]: $[2\bar{1}\bar{1}0]_{HCP} \| [001]_{BCC}$ $(0001)_{HCP} \| (001)_{BCC}$, $[2\bar{1}\bar{1}0]_{HCP} \| [001]_{BCC}$, $(01\bar{1}1)_{HCP} \| (530)_{BCC}$. The $(0001)_{HCP} \| (110)_{BCC}$ and $(2\bar{1}\bar{1}0)_{HCP} \| (1\bar{1}1)_{BCC}$ relationship is called a Burgers orientation relationship. This is one of the most important orientation relationship relationships between a HCP and a BCC phase, and was first identified after phase transformation in Zirconium. One should note that in this orientation relationship the angle between $(1\bar{1}0)_{BCC}$ and the $(1\bar{1}00)_{HCP}$ is 5.3°.

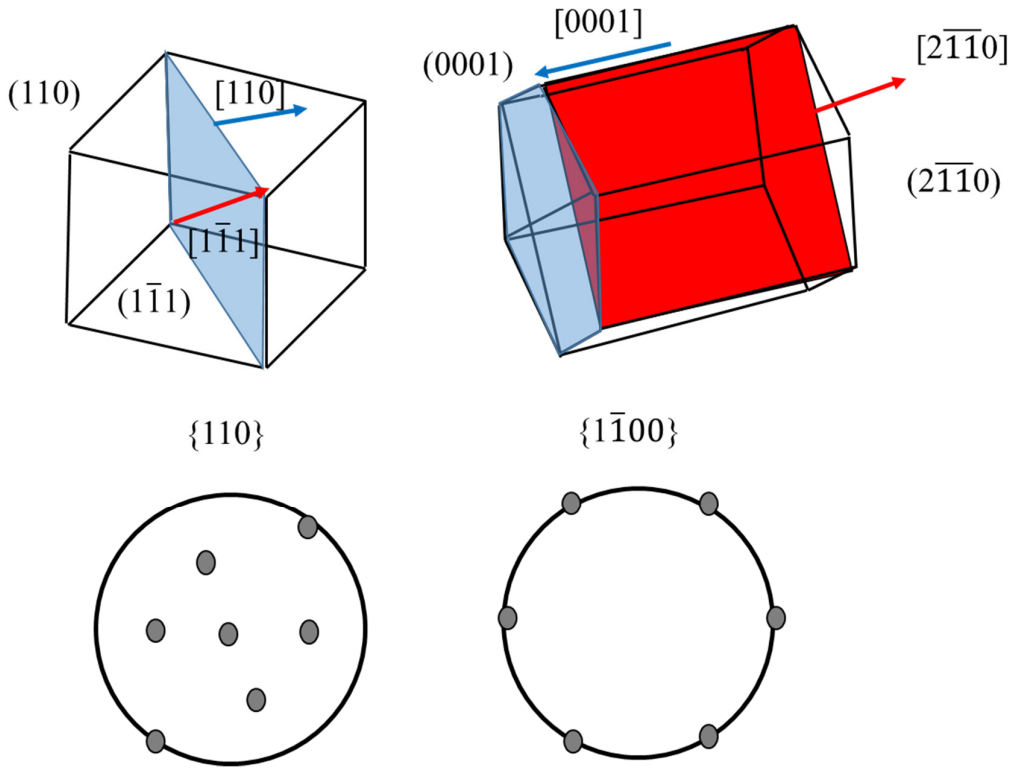

Figure 2.13-1: A schematic representation of the Burgers orientation relationship a) and b) the parallelity of slip planes, and c) the orientation diagrams [83].

In the case where these planes are exactly parallel, the orientation relationship is called Pitsch-Schrader (see Figure 2.13-2).

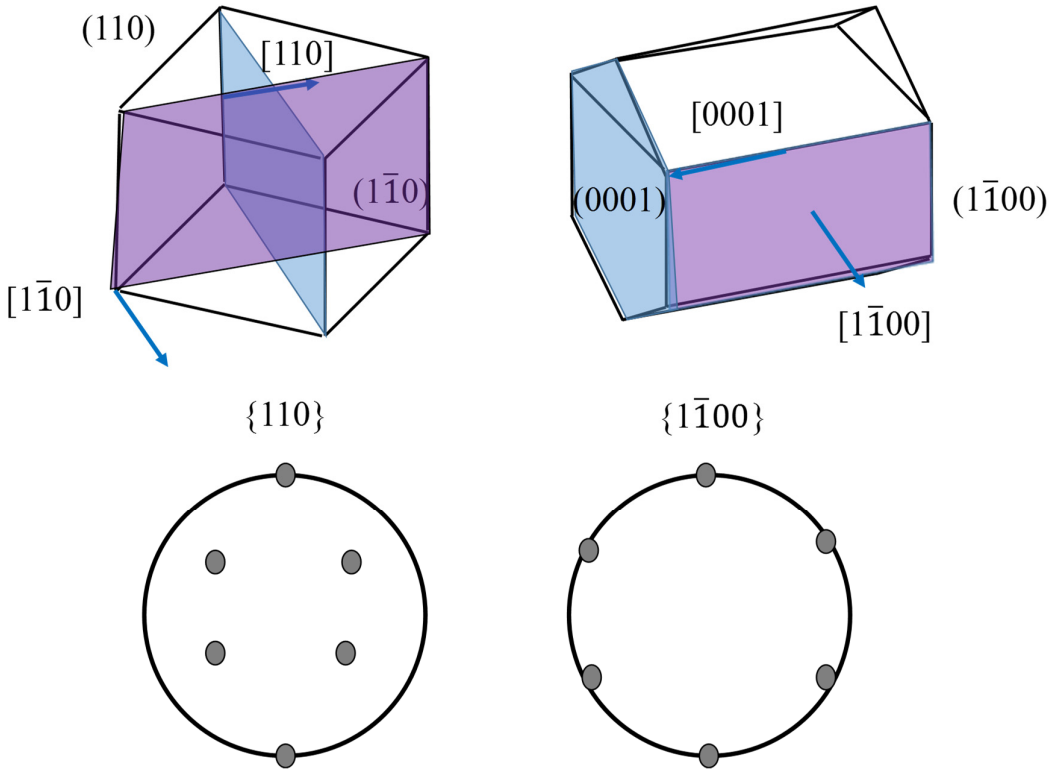

Figure 2.13-2: The Pitsch-Schrader orientation relationship [83].

Another well-known orientation relationship, named after Potter, involves a 1.5° rotation from Burgers orientation $(2110)_{HCP} \| (1\bar{1}1)_{BCC}$ and $(1\bar{1}01)_{HCP} \| (011)_{BCC}$.

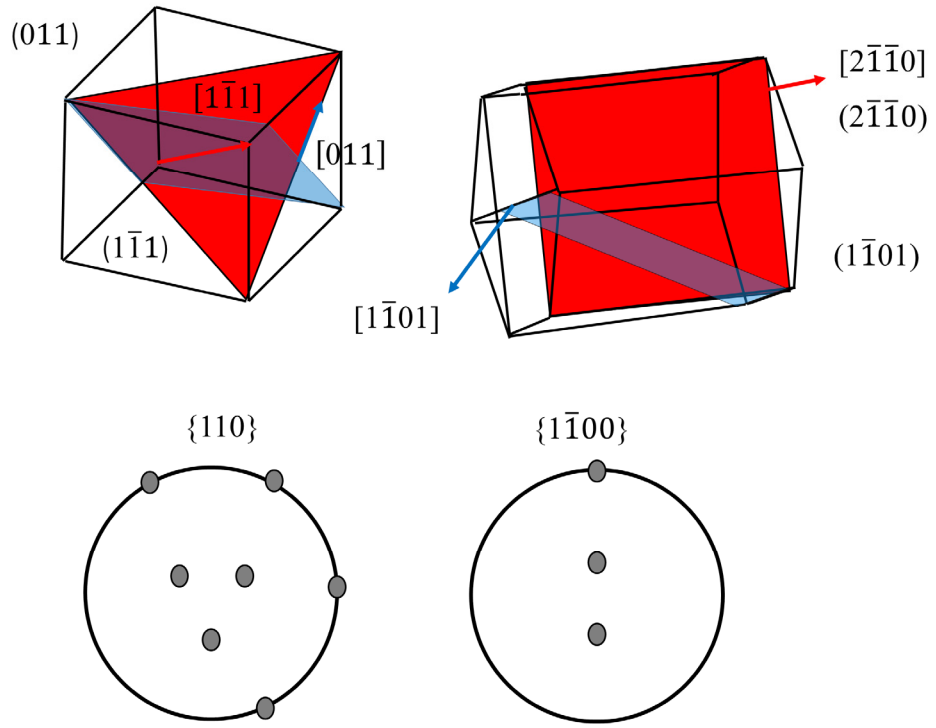

Figure 2.13-3: The Potter orientation relationship, a) crystal geometry and b) the orientation diagrams [83].

The Rong-Dunlop relationship is another well known orientation relationship (see Figure 2.13-4) with $(0001)_{HCP} \parallel (120)_{BCC}$, $(11\bar{2}0)_{HCP} \parallel (001)_{BCC}$ and $(1\bar{1}00)_{HCP} \parallel (2\bar{1}0)_{BCC}$.

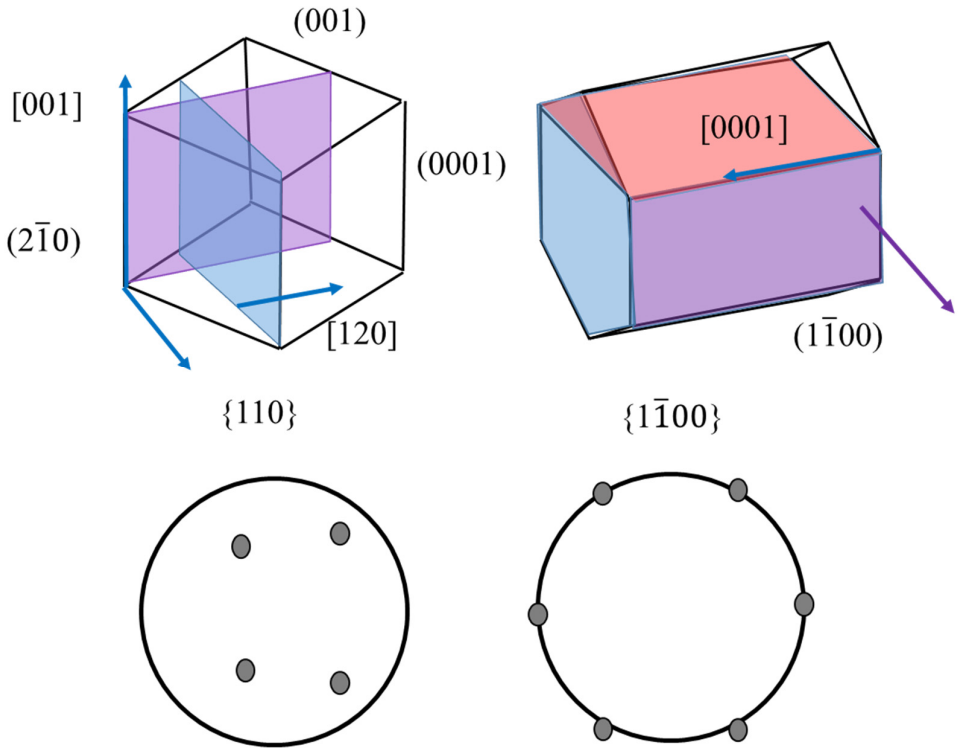

Figure 2.13-4: The Rong-Dunlop orientation relationship, a) crystal geometry and b) the orientations diagrams [83].

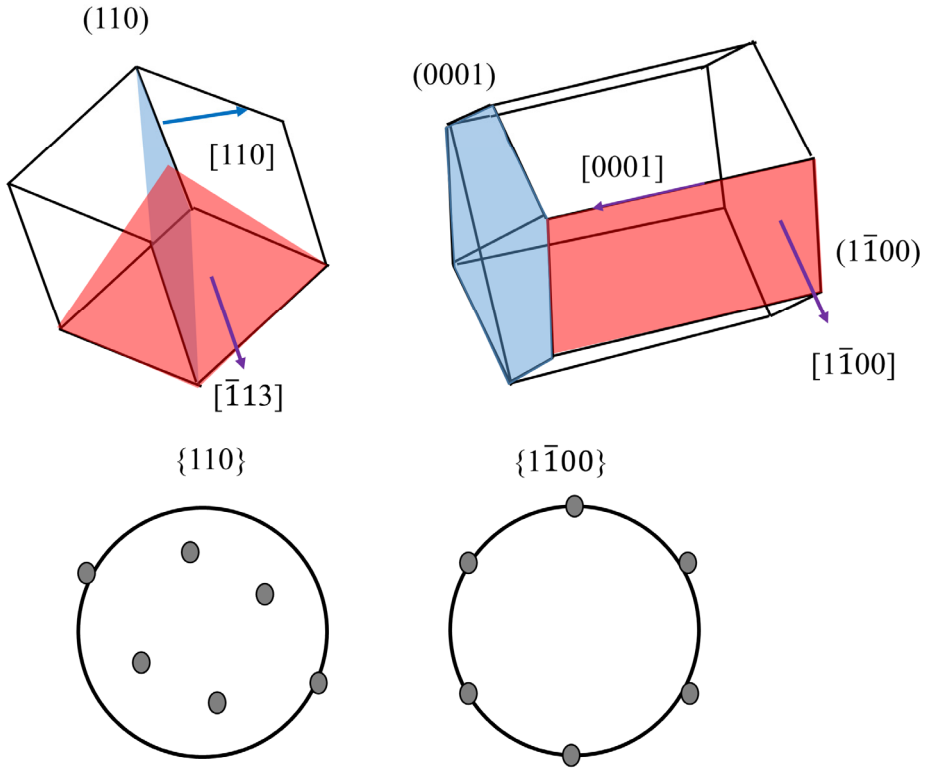

Figure 2.13-5: The Zhang-Kelly No. 5 orientation relationship, a) crystal geometry b) the parallelity of slip planes and c) the orientation diagrams [83].

Some orientation relationships are favored over others. The factors that make a specific orientation relationship more favorable compared to less favorable OR are i) the density of the matching planes between the parent and the daughter phase, ii) the rotation axes between the matrix or parent phases and the daughter phases iii) the Burgers vector [77]
When one considers these factors it will be evident that the Burgers OR is the most observed OR in the HCP/ BCC transformation [70].

2.14 The origin of the orientation relationships in Al-Mg alloys

The $(\bar{1}10)$ plane of the γ-phase-$Al_{12}Mg_{17}$ contains all close packed or nearly closed packed directions, namely the <111>, <110>, <113> as can be seen in Figure (2.14-1). These closed packed or nearly closed packed directions could be potential matching directions between atoms. However, the atomic configuration along these directions are different. The <111> and <110> directions show a straight atomic row potential matching, since there is no significant deviation in the position of all atoms (see Fig. 2.14-2).

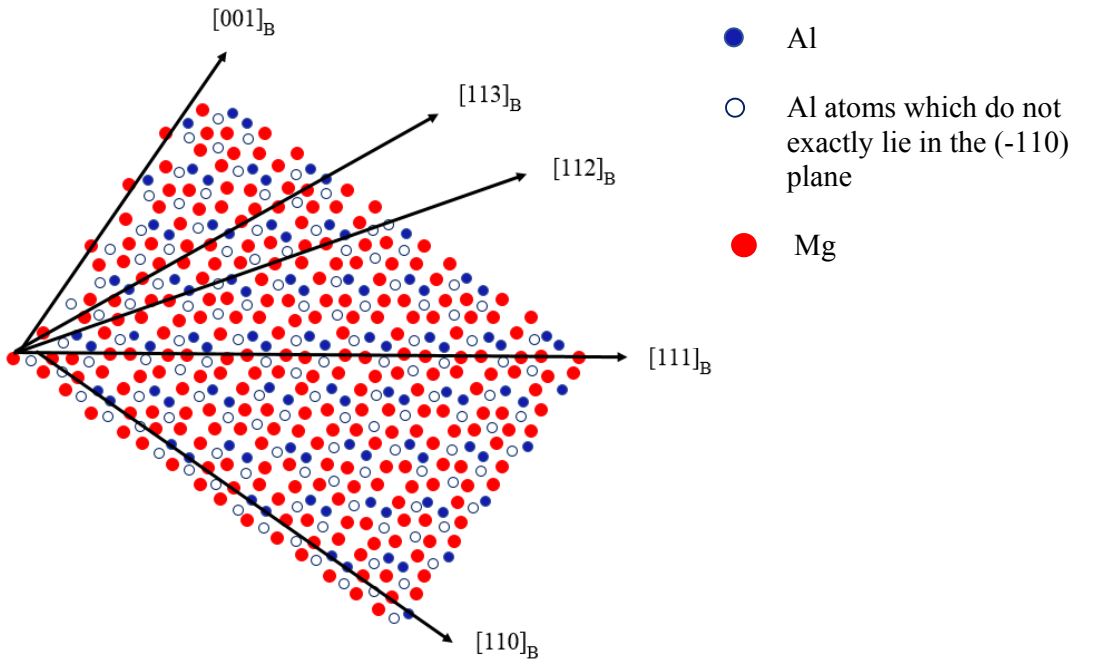

Figure 2.14-1 The atomic positions of Mg and Al in the ($\bar{1}10$) plane of the γ-phase ($Al_{12}Mg_{17}$) [75] .

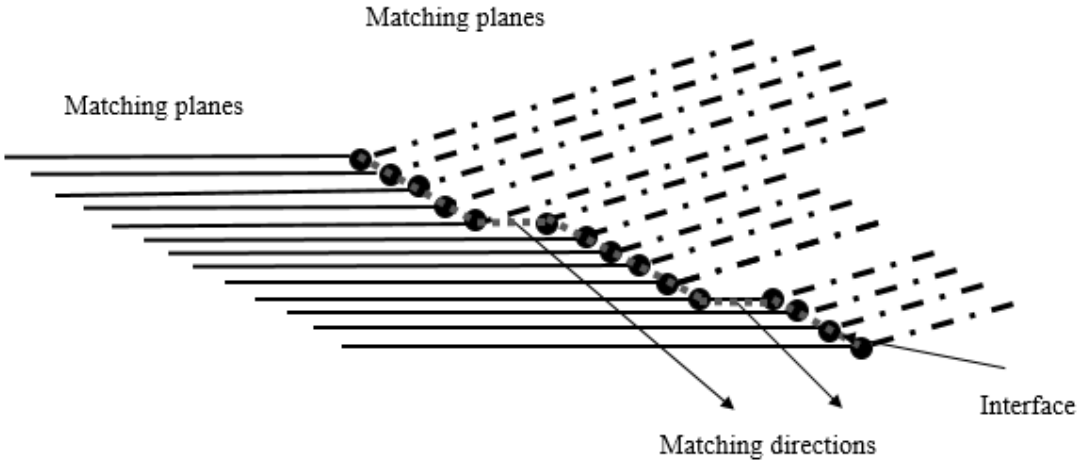

Figure 2.14-2 Schematic diagram showing the formation of an interface based on a) the edge-to-edge matching model b) the Zigzag matching model [74].

The <113> direction on the ($\bar{1}10$) plane shows both straight and zigzag matching possibilities.

Zhong [75] suggested a simple rule that straight rows match with straight rows and zigzag rows with zigzag rows.

Straight row matching conditions leads to two matching direction pairs:

<11$\bar{2}$0> Mg / <111> $Al_{12}Mg_{17}$

<11$\bar{2}$0> Mg / <110> $Al_{12}Mg_{17}$

And the <113> direction leads to three possible direction pairs:

<11$\bar{2}$0> Mg / <113> $Al_{12}Mg_{17}$.

<11$\bar{1}$0> Mg / <113> $Al_{12}Mg_{17}$ and <11$\bar{2}$3> Mg / <113> $Al_{12}Mg_{17}$.

The interatomic spacing along these matching directions depends on the lattice parameters and it differs for each direction pair. The <11$\bar{2}$0> Mg / <111> $Al_{12}Mg_{17}$ matching direction pair is actually the ideal Burger [11$\bar{1}$] $Al_{12}Mg_{17}$ ‖ [1$\bar{2}$10] Mg orientation relationship and the Potter orientation relationship [11$\bar{1}$] $Al_{12}Mg_{17}$‖ [1$\bar{2}$10] Mg. From the above mentioned matching directions eight main orientation relationships have been predicted and have also been experimentally observed as indicated in Table 2.13-1 and Figures 2.13-1 to 5.

2.15 Metal matrix composites

Nowadays, in many industrial applications, there is a need for materials with special properties for a combination of commercial and technological needs. This need has led to the invention of composite materials. The term metal matrix composite designates materials with two, or multiple phase structures that are produced by direct intervention.

Composites can be tailored such that a unique balance of physical and mechanical properties can be obtained, that cannot be achieved by an alloy or a monolithic material.

Metal matrix composites (MMCs) consist of one metal or alloy as a matrix and one reinforcement agent. The reinforcement agent can be present in different forms such as particles, short or long fibers etc.

The properties of the composites can be adjusted by the type of reinforcement, volume fraction, morphology and distribution of the second phases.

The expected properties can comprise high thermal and electrical conductivity, good resistance to aggressive environments, good impact and erosion resistance, good fatigue and

fracture properties, for some specific applications high radioactive absorption, or high strength/stiffness to density ratio [84]. The volume fraction of one of the components can be up to 70%.

The first usage of MMCs was believed to be around 7000 BC, when non-metallic-inclusions in copper were found in Turkey [85]. A couple of well-known industrial application areas of MMCS that were developed in the 1970s were the space shuttle [86] and two-phase wire composites [87]. Examples of metal matrix alloys extent over a very wide range of materials like Al-Si eutectic casting alloys, pearlitic steel, two-phase lamellar alloys such as TiAl, Al-Mg alloys with Al2O3 reinforcement. Application fields include car brake components and high radioactive absorption applications like B_4C.

The composites can be produced by powder metallurgy incorporating both discontinuous and continuous particles followed by outgassing, sintering and hot compaction followed by rolling, extrusion or forging.

Deformation processed metal matrix composites (DMMCs) consisting of two metals have received much attention during the last few decades. This is due to the resultant properties such as thermal and electrical conductivity and material properties such as high thermal and electrical conductivity and attractive mechanical properties including high strength [88-90]. The heavy deformation processing causes work hardening as well as texture changes and grain refinement, resulting in specific characteristics after deformation of the billet made up by a mixed metal matrix composite.

2.16 Metal matrix composites production via powder metallurgy

The starting material is usually a billet consisting of a compacted powder blend of metals that is then deformed by techniques such as extrusion, drawing or rolling. Deformation processed metal matrix composites (DMMCs) of two metal mixtures have received much attention

during the last few decades because of the resultant combination of properties such as thermal- and electrical conductivity and mechanical properties like high strength,[88] [90]. The heavy deformation processing causes work hardening as well as texture changes and grain refinement, resulting in specific characteristics after deformation that are different to the individual metals. The increase in strength of the deformation processed composite is one important result, which is believed to be related among other reasons to the influence of texture on the deformation behavior [91]. In systems combining Al with Cu, Ti or Pb, it was found that the Al phase develops a <111> and <001> double fiber texture in the extrusion direction (ED) when the texture over the whole cross-section is measured [92]. On the other hand, in rectangular extruded material of Al-Ti, Al-Nb and Al-Ni, Al shows four main ideal orientations {123}<643>, {112}<111>, {100}<001> and {110}<111>. The study of highly anisotropic and inhomogeneous materials such as two-phase composites is very important for a basic understanding of many technological materials. Many authors have investigated the deformation texture of two-phase materials. A very early study was performed on α-ß-brass [93]. It was found that each phase developed its own deformation texture.

During the extrusion process, several effects could result in a texture gradient. Firstly, the frictional interaction between the wall and the billet causes shear stresses along the work piece. Secondly, the extrusion conditions such as the shape of the die, the die angle, extrusion speed, and the extrusion temperature can contribute to the texture gradient. Thirdly, the flow stress difference between the two phases and how the stress from one phase is transferred into the second phase may also play a role. Another aspect of metal matrix composites is the fact that they are very useful to study reaction kinetics and getting information on the diffusion between the two phases [94]. The intense mixture of both Al and Mg in this research resulted in a high fraction of phase boundaries. Cold extrusion of Magnesium, due to its poor room temperature formability, is only possible in composites with a high content of Aluminum.

Extrusion is one of the favorite processes for the production of metal matrix composites. Generally, it is defined as a process, in which the material is compressed in a chamber and the deformed material is forced to flow through a die. This means that it is a process by which a block/billet of metal is reduced in cross section by forcing it to flow through a die orifice under high pressure. The die opening corresponds to the cross section of the required product. The extrusion process is divided in the following categories: direct/indirect extrusion, depending on whether the die is moved or not. Also hot or cold extrusion depending on the operating temperature, and horizontal or vertical extrusion depending on the equipment. In the direct extrusion process, which is the most commonly used extrusion process in industry, metal flows in the same direction as that of the ram, there being a relative motion between the billet and the chamber walls. There are two zones for friction, firstly the friction between the billet and the wall of the extrusion die and secondly that between the billet and end of the extrusion chamber. Since the friction is severe and in order to reduce the extrusion force there is the need for a lubricant, between the die and the billet such as lead [95]. In contrast, in the indirect extrusion process, metal flows in the opposite direction of the ram movement (the die is stationary and the billet and container move together). During indirect extrusion, the friction between the billet and wall is negligible although there is still friction between the billet and die. Therefore, indirect extrusion is more efficient, since the friction is considerably reduced. The flow of material is also very homogenous. However, it is a deformation process with limited application, since firstly it is restricted to the length of the extruded component, secondly the cross-sectional of the final product is limited to the diameter of the hollow stem [96, 97, 98]. The schematic representation of both processes is shown in Figure 2.16-1. There are some other extrusion processes such as impact extrusion and hydrostatic extrusion. Generally, it may be concluded that the extrusion process has advantages such as the realization of complex cross-sections, high true strains, combined with moderate costs of

the equipment and tooling. Disadvantages include the necessary application of a lubricant, the dimension accuracy and the poor quality of the finished shaped product. There can also be defects in extruded products such as surface cracking and piping.

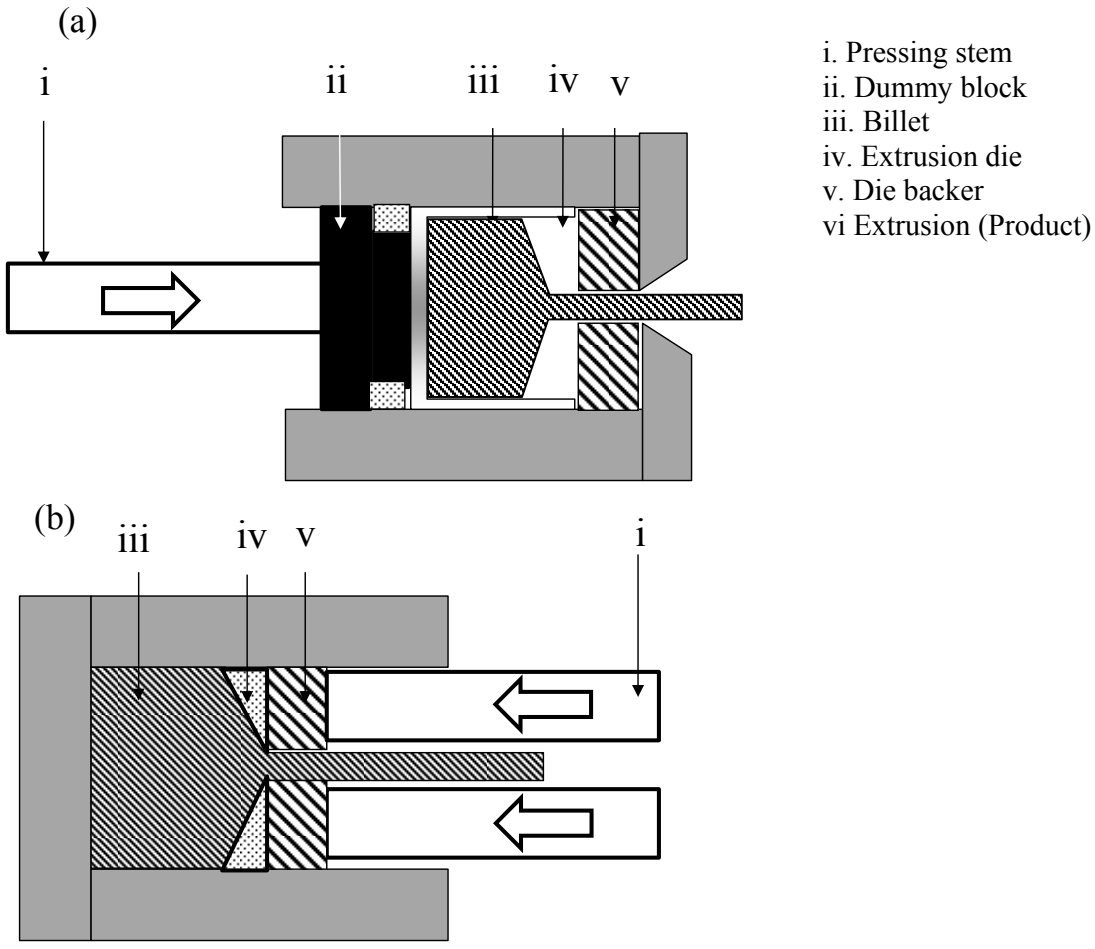

Figure 2.16-1: a) the direct and b) the indirect extrusion process.

2.17 General description on texture

To represent the orientation distribution of crystallites (texture) in a sample, two coordinate systems are necessary. The first coordinate system relates to the sample symmetry (K_A).and is defined in terms of the sample geometry, which contains the rolling or extrusion direction

(RD/ED), the transverse direction (TD) and the normal direction (ND). The second system is the crystal symmetry (K_B), which is defined through the crystal axes according to the crystal symmetry.

The crystal orientation (g) is defined as a rotation, which transfers K_A into K_B. This transformation can be written in the formK_B= g. K_A.

The crystal orientation can be described in many different forms like the orientation matrix, the Euler angles $\{\varphi_1, \Phi, \varphi_2\}$, the ideal orientation, Miller, Miller-Bravais notation, a rotation axis r and angle ω, the Rodrigues vector, or also some other.

In this communication, the Miller indices <uvw> was used, which refer to the crystallographic direction parallel to the sample axis ED and {hkil} which are the crystallographic planes parallel to the ED.

Each point in Euler space corresponds to a particular rotation and each rotation or crystal orientation leads to a point in the three-dimensional space. If one denotes V as the total sample volume and dV as the sum of all volume elements within the sample which possess the orientation g, then an orientation distribution function f (g) can be defined by:

$$f(g) = \frac{\frac{dV}{V}}{dg} \quad g = \{\alpha,\beta,\gamma\} = \{\varphi 1, \Phi, \varphi 2\} \qquad \text{Equation 2.17-1}$$

For multi-phase materials like metal matrix composites, the texture can be easily determined by defining the texture of each phase separately. The complete texture of a multi-phase material is described by the individual texture of each component and their correlation to each other. Investigation with neutrons [99] have shown that the texture of 1Vol.% Cu in a 99 Vol.% Al matrix can be determined. In the case of polycrystalline materials, the whole orientation distribution can be described by an Orientation Distribution Function (ODF). The ODF function f (g) quantitatively describes the volume fraction of the sample in terms of an orientation (g). Bunge [100] defined the function f(g) using symmetrical generalized spherical harmonics as

$$f(g)=\sum_{l=0}^{l_{max}}\sum_{m=-l}^{M(l)}\sum_{n=-l}^{l} C_l^{mn}\, T_l^{mn}(g) \qquad \text{Equation 2.17-2}$$

Where C_l^{mn} are the coefficients of the series development of the texture function f (g), $T_l^{mn}(g)$ the generalized spherical harmonic functions, M(l) the number of linearly independent harmonics and l_{max} the maximum series expansion degree.

2.18 Theory of powder diffraction

Phase and texture investigations using monochromatic X-rays are both based on the same principle of diffraction. When X-rays pass through a material their intensity is reduced via absorption and scattering. The absorption effect will be discussed in section 2.20. The scattering effect is described by Braggs law which was formulated by W.H. Bragg and W.L. Bragg and introduced in 1914 [101]

$n\lambda=2d\sin\vartheta$

Where λ the wavelength of the X-rays, d is the spacing of the diffracting lattice planes within the crystallites and ϑ is the angle of incidence of the beam with the diffracting planes, n is defined as an integer number.

It should be mentioned that the relation between the incident and diffracted beams was first given by Laue [101] by:

$$a(\cos\psi_1) - \cos\varphi_1 = h\lambda \qquad \text{Equation 2.18-1}$$

$$b(\cos\psi_2) - \cos\varphi_2 = k\lambda$$

$$c(\cos\psi_2) - \cos\varphi_3 = l\lambda$$

Where a, b and c are dimensions of the unit cell $\psi_{1\text{-}3}$ and $\varphi_{1\text{-}3}$ are the angels of incident and diffracted beams. The first experimental application of X-ray diffraction to study specimens at high temperatures was carried out in the early 1920's. Since that time, it has been developed into a practical standard technique. Phase analysis with high-energy synchrotron radiation is

based on the same principals as conventional X-ray and neutron diffraction. The advantage of high energy X-ray radiation is the ability to investigate large sample volumes.
The integrated intensity I of the Bragg peak is a function of many parameters as described by Equation 2.18-3 [101].

$$I_{hkl}=P_{hkl}*K*L_{\vartheta}*P_{\vartheta}*A_{\vartheta}*T_{hkl}*E_{hkl}*\left|F_{hkl}^{2}\right| \qquad \text{Equation 2.18-2}$$

K is defined as scale factor, P_{hkl} is the multiplicity factor, L_{ϑ} is the Lorentz multiplier, P_{ϑ} is the polarization factor, $A_{\vartheta}$is the absorption multiplier, T_{hkl} is the preferred orientation factor, E_{hkl} is the extinction multiplier, F_{hkl} is the structure factor. For more information about the definition of each parameter one can refer to [101].

2.19 Synchrotron radiation

Synchrotron radiation has delivered a number of novel and unique contributions to the field of texture measurement and phase analysis. The development of synchrotron radiation sources comes from the Betatron that was invented by Donald William Kerst at the University of Illinois [102]. In the Betatron, electrons were accelerated to 2.3 MeV to generate X-ray radiation. The disadvantage of the Betatron was that the magnetic field was limited to 1-2 Tesla and the electron acceleration was limited to only a part of the magnet cycle. The use of a larger magnet was not possible due to the construction principles of the Betatron. Therefore, in order to achieve higher X-ray energies, the synchrotron was developed. Synchrotron radiation is produced when electro-charged particles such as electrons or positrons that have been accelerated to a speed close to that of light in a storage ring and are forced to change their flight direction by a magnetic field produced by bending magnets [103]. The charged particles move in several packages called bunches around the storage ring. The photons having energies ranging from 1 MeV to 100 MeV are generated in a tangential direction to the forward direction of the electrons [103]. In the storage ring, bending magnets are used to

maintain a circulating beam by bending electrons or positrons into a closed orbit. Nowadays, wigglers and more recently undulators, are incorporated into the storage ring to periodically bend the electron beam and produce X-rays. Where undulators are used synchrotron radiation with a much higher intensity is produced. Such a high intensity X-rays cannot be obtained by bending magnets [104, 105]. Both wigglers and undulators deflect the electron beam in alternating directions, producing an angular excursion of the beam augmented in intensity [104, 105]. The first report about the application of Synchrotron radiation in the measurements of texture was published by Gottstein [106]. He used the Laue back pattern reflection method and employed film techniques [106]. From that time many developments in the application of synchrotron for texture measurements have been implemented.

Synchrotron radiation has some orders of magnitude higher intensity than laboratory X-ray devices. Having such a high intensity and a short wavelength of about 0.1 Å has twofold advantages. Firstly, the radiation has a high penetration depth in the sample. With an X-ray energy of 100 keV one can penetrate 22 mm Aluminum, 34 mm thick Magnesium and 8 mm thick Ti. Secondly, the high intensity allows a short exposure time, which is a necessary requirement for in situ studies. Using small beam diameters results in a high orientation resolving power. This high orientation resolving power and the use of small beam diameters make synchrotron radiation a unique tool for studying texture gradients specially in two phase materials [107,108].

Other important features of synchrotron radiation like a low divergence also have benefits, including high resolution of the Bragg angle which makes it possible to study the texture of multi-phase materials such as intermetallic compounds [109] .

In this investigation monochromatic radiation was used to record the Debye-Scherrer patterns on an image-plate area detector. The idea of using an image plate detector comes from an old film method for texture measurements [110].

In order that all symmetrically equivalent directions hkl of the crystalline material studied come into the reflection position one has to rotate the sample through an ω angle [109]. Besides the advantage of synchrotron radiation for texture measurements [111], its high brightness and flux, extremely collimated beam, high signal/noise ratio and high angular resolution has major advantages in phase analysis studies for the detection of low volume fraction phases. Its low absorption makes measurement of the sample without any preparation and also application of in situ furnace possible. The low divergence of the synchrotron beam causes high angular resolution on the pole sphere and in the Bragg angle ϑ. Synchrotron beams have high intensity, which results in high penetration depth in the sample. It also makes the measurement of the sample in very short time due to short exposure time possible. Due to high intensity and high angular resolution a small beam diameter can be used [112] This makes synchrotron radiation extremely effective in performing complex phase investigations. Moreover, the bunches of electrons result in short pulses of synchrotron radiation and thus make the investigation of very fast processes possible.

2.20 Absorption and volume correction

For the investigation of texture in multiphase materials, a topic that was discussed in the previous section, it is necessary to address problems concerning anisotropic X-ray absorption. The goal of the absorption correction is to ensure that the calculated texture should only be the result of the distribution of the second phases and not their volume fraction. The intensity of the synchrotron spectrum is decreased after it has transmitted through a material (Figure 2.20-1). This decrease of intensity depends on three main factors, the geometry, the properties of the sample material and the type of diffraction method employed. These parameters need to be considered in order to perform the absorption correction. Firstly, since a composite material has been used in this investigation, the absorption correction for the composite, which is different from the pure metals, should be calculated. Lambert and Beer [113]

presented a mathematical formula to describe the attenuation of radiation intensity after passing through a medium. The formula is $I=I_o.e^{-\mu d}$ (Equation 2.20-1), where I_o is the primary intensity before entering the material, μ is the linear absorption coefficient and, d is the thickness of the material. The linear absorption coefficient of any chemical element is a function of the radiation wavelength and can be calculated using the formula $\mu=(\rho*\frac{\mu}{\rho})$ (Equation 2.20-2). The linear absorption coefficient depends on the physical and chemical state of the material; the mass absorption coefficients $\frac{\mu}{\rho}$ depends only on the atomic character of the material, i.e. graphite and diamond have the same mass absorption coefficient, but not the same linear absorption coefficient. The mass absorption coefficient depends on the wavelength of the radiation and nowadays can also be looked up with the help of a database.

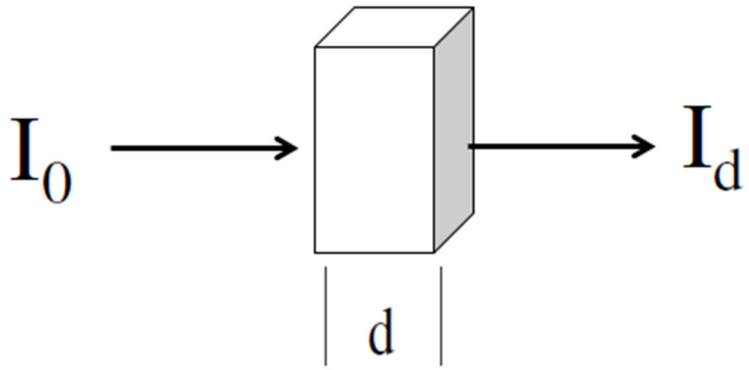

Figure 2.20-1: Schematic description of Lambert-Beersche decription

For compositions such as Al_3Mg_2 and $Al_{12}Mg_{17}$ the mass absorption coefficient can be calculated as follows:

First, one should calculate the mass fraction of Al and Mg in both intermetallic compositions, which are formed.

In the case of Al_3Mg_2 the mass fraction of Al in Al_3Mg_2 will be 0.618 and for Mg is 0.381. These values in the case of $Al_{12}Mg_{17}$ are for Al 0.4325 and for Mg 0.567.

One can find the mass attenuation coefficient value for different X-rays energies in [112] and the values for Al and Mg are 2.018×10^{-1} $cm^2g^{-1}$and 1.951×10^{-1} cm^2g^{-1} respectively.

Knowing the mass fraction of Al and Mg in the Al_3Mg_2 and $Al_{12}Mg_{17}$ phase and the mass attenuation coefficient values, one can calculate $\frac{\mu}{\rho}$ for $Al_{12}Mg_{17}$ to be 0.197 cm^2g^{-1} and for Al_3Mg_2 0.1847 cm^2g^{-1}.

The theoretical density ρ is given by the equation:

$$\rho = \frac{n.A}{V_c \ .N_A} \qquad \text{Equation 2.20-3}$$

where n= number of atoms, A=atomic weight V_c =volume (cm^3) and

N_A=Avagadro's number ($6.02*10^{23}$)

For Al_3Mg_2 the cell volume is 22518.94 cm^3) which results in $\rho = 2.346$ ($\frac{g}{cm^3}$) and therefore $\mu = 2.346*0.1847 cm^{-1} = 0.432 \ cm^{-1}$.

For $Al_{12}Mg_{17}$, the cell volume is 1173.97 cm^3) and the cell formula unit is 2 resulting in $\rho = 2.085 \ \frac{g}{cm^3}$ and therefore $\mu = 2.085*0.197 \ cm^{-1} = 0.410 \ cm^{-1}$. For Mg μ is equal to 0.32 cm^{-1} and for Al 0.5 cm^{-1}.

One should note that it is considered that the packing density through the sample thickness is considered to be constant.

Volume correction: In the extreme case the beam intensity of the sample with a rectangular shape can change by a factor of 2.24 due to the variation of the irradiated volume with the incidence angle.

3 Experiments:

3.1 Material production

For the production of the Al60Mg40 and Al40Mg60 (wt.%) composites, powders of Al with a particle size smaller than 100 µm and a purity of 99.94% and Mg with a particle size smaller than 63 µm and a purity 96% were used. The Al and Mg powders were mixed together in proportions of 60 to 40 and 40 to 60 using a tubular mixer. After that the powder mixture was compressed under protection of Argon gas at room temperature to a pre-compact (billet) with a diameter of 50 mm. The billets were wrapped in a lead foil to reduce friction and temperature during subsequent extrusion. Later on, the billets were extruded at room temperature to rectangular bars with a cross section of 5 x 20 mm^2 as can be seen in Figure 3.1-1. The degree of deformation was around 95 %. After extrusion, there was a roughly 0.1 mm thick lead coating on the surface, which had to be removed before further use. The length of the extruded bars, depends on the billet volume and was about 100 cm.

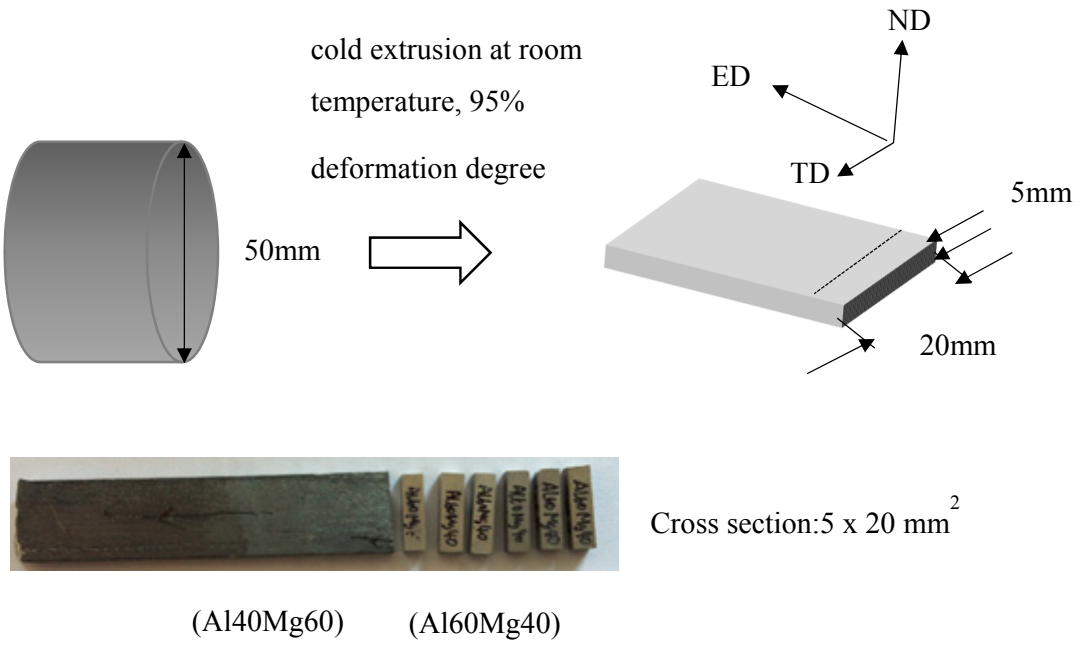

Figure 3.1-1 : Schematic sketch illustrating the material production.

3.2 Microstructure of the bars after room temperature extrusion

The microstructure was characterized using optical microscopy. To do this, the samples were first cold mounted in resin (Demotex 30 from Demotec Metallographie). Then grinding was performed using successively finer silicon carbide abrasive papers with grit sizes from 80 to 2500.

Polishing was then performed with a Struers Tegramin-30 using OPS (silicon oxide) with a 40 nm particle size as an abrasive and ethylene-glycol as a lubricant.

During preparation of the specimens, special attention was paid to minimize heating of the samples and water contamination, which may have an influence on the resulting microstructure. Microhardness investigations were conducted on TD-ND planes of the extruded bars in order to detect any potential microstructural or properties gradients and to see how they correlate to the texture gradient. An automated Vickers hardness testing machine was used with a 0.2 kg load and an indentation time of 15 s, according to the E 38-99 ASTM standard. By making measurements over a grid pattern, the complete microhardness distribution along the specimen was obtained.

3.3 EBSD measurement

The EBSD measurements were performed on an AURIGA 40 scanning electron microscope equipped with a Digiview detector (from EDAX) and a field emission gun. The AURIGA is operated by the SmartSEM software from Zeiss. Data acquisition and analysis was performed using the TSL-OIM software from EDAX. Orientation image mapping (OIM) was conducted using a 0.2 μm step size with an accelerating voltage of 20kV.

The specimens for EBSD were first ground as described earlier and then polished for 30 minutes on a polishing cloth with 1 μm using an ethylenglycol lubricant and a commercial water free silica suspension. The final polishing step in the sample preparation was conducted on a polishing cloth without abrasive particles with the same lubricant and suspension mentioned above.

3.4 Ex-situ sample heating

For the ex situ investigations a laboratory furnace from Heraeus was used. The furnace was operated under a protective argon atmosphere with a pressure of about $p<1.10^{-6}$ hPa. The temperature of the sample was controlled by two thermocouples. The maximum deviation from the nominal temperature was less than 5˚C. As the heating period the time was considered from the time the samples were put into the furnace until the time they were taken out. Annealing of the Al40Mg60 and Al60Mg40 alloys was performed for 2 different time periods, 2 h and 12 h at temperatures of 100℃, 200℃, 250 °C 300 °C and 400 °C, followed by air cooling to room temperature.

3.5 In situ phase analysis

The samples were annealed in a dome furnace that was specially designed for texture measurements using synchrotron radiation. The dome was made from SiO_2-glass, which enabled measurements to be made at all omega angles, (see Figure 3.5-1). The heating element consisted of a graphite foil, which is penetrable by synchrotron radiation. Figure 3.5-1 shows the furnace employed. An important point is that the sample must be positioned at the centre of the graphite heater in order to have an acceptable degree of temperature uniformity within the sample (see Figure 3.5-1). The temperature was controlled with a thermocouple connected to the sample and a second thermocouple connected to the lower part of the furnace. The sample was mounted on an ω-stage that was attached to a x-z-table. This setup allows scanning of the sample along the z direction and the sample can be rotated around the vertical axis.

A monochromatic high energy X-ray beam with an energy of 87.7 keV and a beam size

of 0.5 mm x 0.5 mm was used. The sample was positioned on the sample holder of the furnace and was fixed with two small screws, the rolling direction was oriented towards the detector. An image plate detector (Perkin Elmer 1621) was positioned perpendicular to the beam at a distance of 1253 mm from the sample.

By using a standard LaB_6 powder with known lattice parameters, the sample to detector distance and the position of the beam center were determined from the diffraction pattern. To study the phase evolution and texture development, a set of experiments were performed, in which the samples were held for 12 h at 200 ˚C and 6 h for at 250 ˚C after the temperatures had been reached.

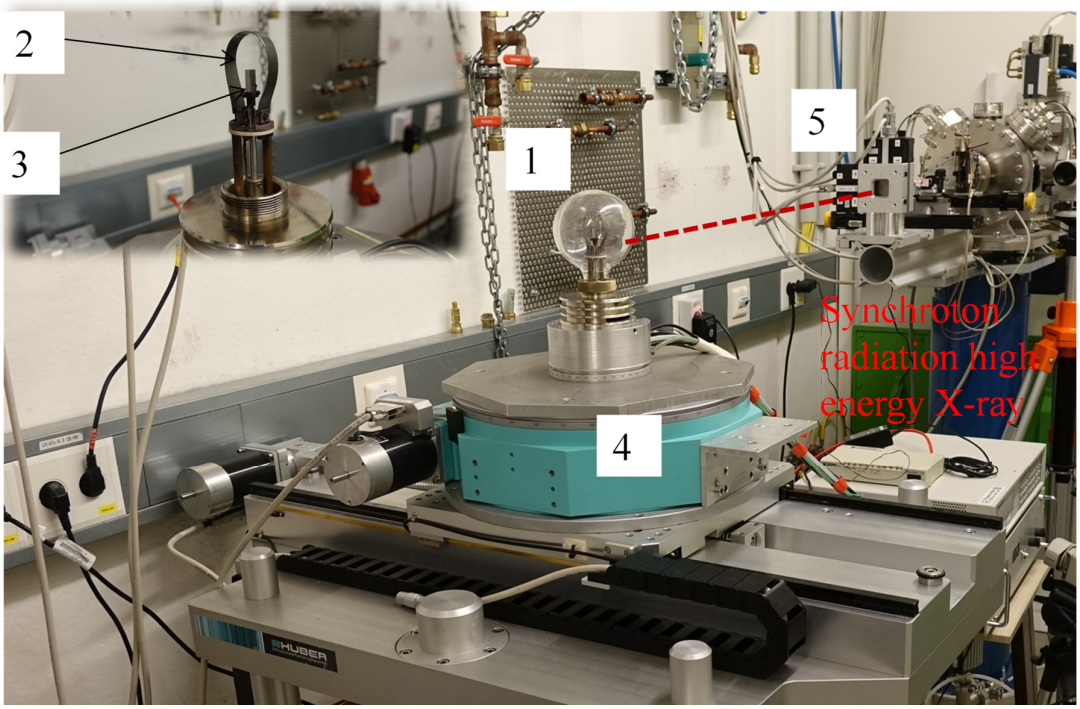

Figure 3.5-1: Specially designed furnace. 1. Furnace with glass wall 2. Graphite as heating element 3. Sample 4. Rotation table (ω-axis) 5. Synchrotron radiation shutter.

A diffraction pattern was taken every 15 minutes in order to determine the phase evolution and every hour a pole figure was also recorded. The exposure time per frame was 1s and the effective pixel size was 200 × 200 μm^2.

The high penetration of 87.7 keV X-rays allowed 5 mm thick samples to be investigated in transmission without any problems. The samples were fixed on an ω-stage that was mounted on an x-z-table. This enabled the investigation of the sample along the z direction while being rotated around the vertical axis. Using this setup, the extrusion direction was oriented parallel to the beam with the transverse direction pointing upwards. Due to the high brilliance of the synchrotron radiation, the investigations were completed after a relatively short measurement time.

3.6 Ex situ phase analysis

Ex-situ phase analysis was performed using the same data as the texture measurements. As discussed in the section concerning powder diffraction theory, for each X-ray diffraction pattern 37 pictures were taken and summed together after rotating the specimen between images by 5° using the Fit2D software. This was done in order to remove the effect of texture on the peak intensity ratios in the final integrated diffractograms.

3.7 Quantitative phase analysis

In order to correct for the effect of texture on the peak intensities, quantitative phase analysis was done by calculating so-called “sum diffraction pattern” from each of the 37 images that were obtained for pole figure measurement. A summed diffraction pattern is obtained by integration over the complete Debye-Scherrer rings. Finally, all 37 summed diffraction patterns were added together to randomize the effect of preferred orientation. For Rietveld refinement [114] the Materials Analysis Using Diffraction (MAUD) software version 2.8 was used [121]. The instrument calibration was performed by using standard NIST LaB_6 powder with the reference number 660c. The quality of the fit was indicated by weighted profile R-factor (Rwp) and the goodness of the fit. All fits were also checked graphically.

3.8 Texture measurements

Due to the high penetration of the hard X-rays and sufficient local resolution, synchrotron radiation is ideal for this kind of investigation. Texture measurements were performed with high-energy synchrotron radiation at the High Energy Materials Science (HEMS) beamline P07B at PETRAIII operated at the DESY research center (Hamburg, Germany). This beamline consists of four experimental hutches. Figure 3.8-1 shows a sketch of the beamline setup.

The primary white X-ray beam from the undulator enters through a high vacuum synchrotron pipe filter. After reducing the divergence of the beam, the beam enters the optical hutch. The High Energy Material Science Beamline (HEMS) consists of two experimental hutches. A single bounce monochromator (SBM), consisting of two flat water-cooled Laue crystals, namely a Si (111) and a Si (220) single crystal monochromator in the monochromator chamber with an asymmetric angle of 35.56º, is used for the side station. Based on the crystal structure of the monochromator two wavelengths can be obtained. Firstly, via the Si (220) crystal the wavelength is equivalent to X-ray energies of about 87 keV and 174 keV whereas the Si (111) results in X-ray energies about 57 keV and 114 keV. The beam size is controlled, firstly by the collimator in the monochromatic chamber and secondly by the vertical-horizontal slit system. The intensity of the incident beam can be reduced by a copper sheet or so-called absorber.

The sample was placed on an ω-stage that was mounted on an x-z-table (see Figure 3.8-1), which allowed scanning of the sample through the z direction and rotation around the vertical axis. The translation through the x and z directions makes local texture measurements at different positions possible.

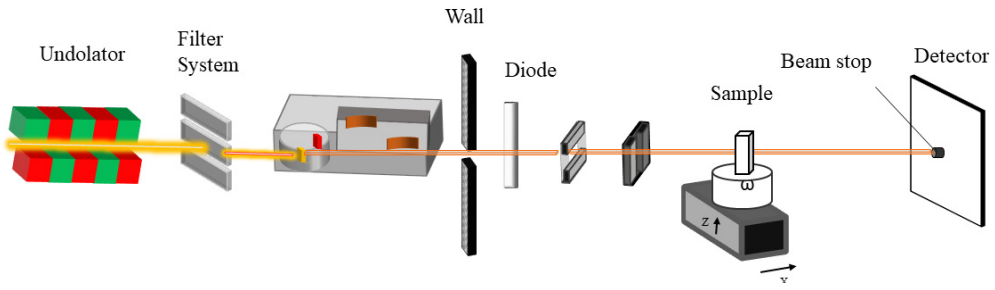

Figure 3.8-1: Beam line set-up for texture measurement at P07 in Petra III.

Generally, two area detectors of either type Mar345 (with a resolution of at least 0.1 mm to 0.15 mm and a maximum diameter of 345 mm) or a Perkin Elmer XRD 1621 detector (with a very fast readout time, a resolution of 0.2 mm and a diameter of 416 mm) can be installed on request [106,107,108, 109] [111,112].

When the beam enters the sample, two conditions should be met in order to obtain a reflection by the lattice planes (hkl). Firstly, the Bragg law $n\lambda = 2d_{hkl} \sin\theta$ has to be fulfilled and secondly, the normal **h** of diffracting lattice plane (hkl) must be parallel to the diffraction vector $\mathbf{\Delta k} = \mathbf{k'} - \mathbf{k}$, with **k** being the wave vector of the incoming beam and **k'** the wave vector of the reflected beam [115].

As can be seen in the Figure 3.9-1, a {hkl} Debye-Scherrer ring recorded at a certain angle ω on the area detector corresponds to a circle in the {hkl} pole figure. The sample has to be rotated from ω = 0° to 180° degrees to cover the whole sphere. For each degree of rotation, a Debye-Scherrer ring should be recorded. The rotation step size used (3° or 5°) was selected depending on the texture sharpness of the material. When the texture is sharper it is better to use a smaller step size like 3°.

The sample crystal symmetry defines the ω-rotation angle range, i.e. for an orthorhombic sample symmetry it ranges from 0° to 90° and for monoclinic and triclinic symmetry from 0° to 180°. One should note that even when the sample is rotated 360° around the ω axis, there

are still some blind areas where data is not collected. However, these blind areas are very small and for metallic materials and a high energy X-ray beam negligible [116].

3.9 Data analysis

It is necessary to obtain the recalculated pole figure from the Debye-Scherrer rings. First of all, misalignment of the detector has to be corrected and the detector-sample distance and wavelength of the experiment determined. This was done using a standard powder such as LAB_6, which is strain- and texture free. The software package Fit2D developed at ESRF [117] has become a quasi-standard software for performing this operation. The FIT2D program, the same program that was used for calibrating the detector parameters was used for this purpose. This program can handle both .tif format images from the PerkinElmer detector and .mar format from the MAR detector and converts the images to diffractograms by integration over the azimuthal angle and produces an output with an ASCII format. The software package SABO written by Yi [33] was used to extract pole figures from Debye-Scherrer rings. The 37 images obtained after rotating the sample in 5° steps, were combined and converted into diffractograms. As can be seen in Figure 3.9-2.the result are 360 diffractograms for every detector picture, that means (37 ×360) 13320 in total for one texture determination. The most interesting Debye-Scherrer ring (hkil) was selected for the extraction of a pole figure. Programs such as Origin or Excel can be used to perform a correction for the variation in primary intensity, volume change and anisotropic absorption as well as a background correction. The next step is to generate the pole figure data sets in measurement coordinates (ω,γ).

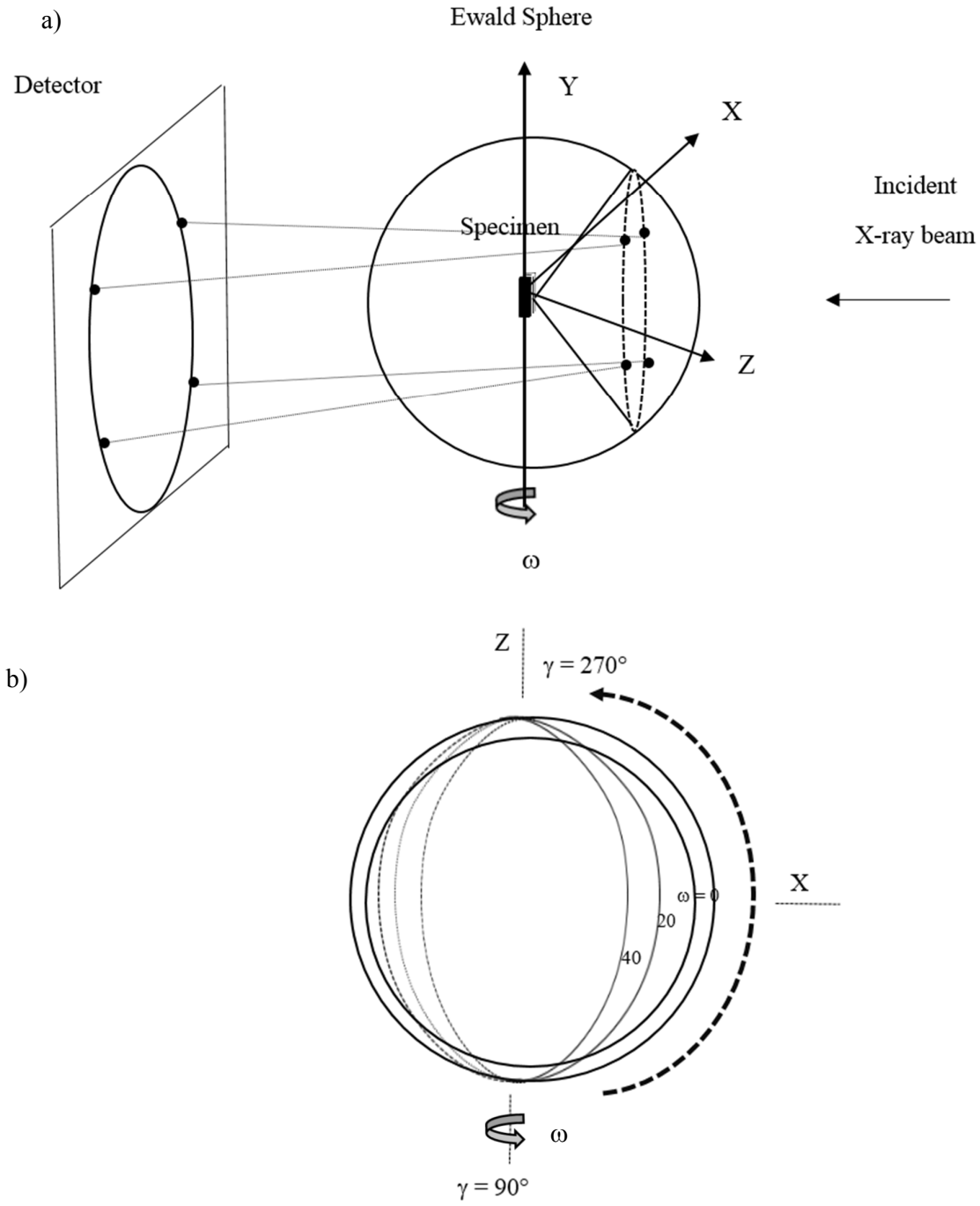

Figure 3.9-1: a) Pole figure measurements using Ewald sphere b) rotation of Debye-Scherrer rings at different ω-rotation angles.

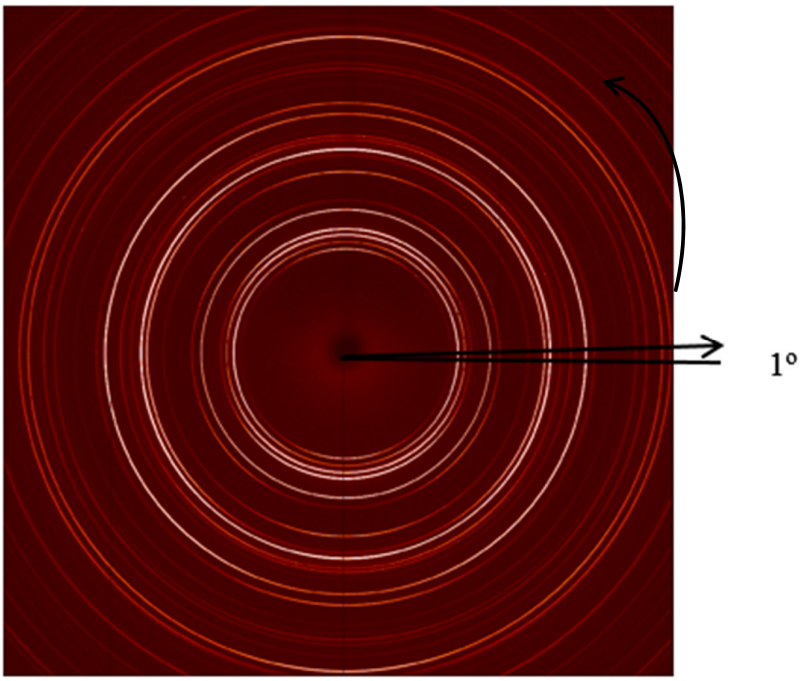

Figure 3.9-2: Production of diffraction pattern over 1 °

The data received from the above mentioned steps including the sample position {ψ, φ, ω} and diffraction geometry {γ, θ} should be converted into pole figure distance α and azimuth angle β via the equation 3.9-1.

Equation 3.9-1:

$$\begin{pmatrix} \sin\alpha.\cos\beta \\ \cos\alpha \\ \sin\alpha\sin\beta \end{pmatrix} = \begin{pmatrix} \cos\omega\cos\varphi & \sin\omega\cos\varphi & \sin\varphi\sin\chi \\ -\sin\omega\sin\varphi\cos\chi & +\cos\omega\sin\varphi\cos\chi & \\ -\cos\omega\sin\varphi & -\sin\omega\sin\varphi & \cos\varphi\sin\chi \\ -\sin\omega\cos\varphi\cos\chi & +\cos\omega\cos\varphi\cos\chi & \\ \sin\omega\sin\chi & -\cos\omega\sin\chi & \cos\chi \end{pmatrix} * \begin{pmatrix} -\sin\Theta \\ \cos\Theta\cos\gamma \\ \cos\theta\sin\gamma \end{pmatrix}$$

Later on, one should recalculate the experimental pole figure since the measured pole figures contain errors. The pole figures were then interpolated for representation in a regular 5°×5° grid format. The orientation distribution function (ODF) was calculated by an in-house program (Clausthal-ODF) written by Dahms which uses an Iterative Series Expansion Method (ISEM) [118].

The series expansion function uses the fact that a texture function f(g), as described in the theory of texture section (section 2.18), can be developed into a series of generalized spherical harmonic functions T_l^{mn} (g) (see equation 3.9-2) [100].

Equation 3.9-2:
$$f(g)=\sum_{l=0}^{l_{max}}\sum_{m=-1}^{l}\sum_{n=-1}^{l} C_l^{mn}\, T_l^{mn}\ (g)$$

This is a very general description of a series of functions, for more information, see Bunge [100]. For a cubic crystal symmetry 3 - 4 pole figures are sufficient to calculate the ODF and for a hexagonal crystal symmetry 5 - 6 pole figures are required. Accordingly, for the crystal symmetry of aluminum the ODF was calculated using the (111), (200) and (220) pole figures, while for hexagonal magnesium the $(10\bar{1}0)$, (0002), $(10\bar{1}1)$, $(10\bar{1}2)$, $(11\bar{2}0)$ and $(10\bar{1}3)$ were used to calculate the ODF. The degree of series expansion L_{max} was 22.

3.10 Texture gradient measurements of the extruded material

The aim was to determine the texture gradient along the TD. For the synchrotron texture measurements, test samples of 5 x 5 x 20 (length) mm³ were prepared and five positions were selected for texture measurements (positions Z1 to Z5, see Figure 3.10-1).

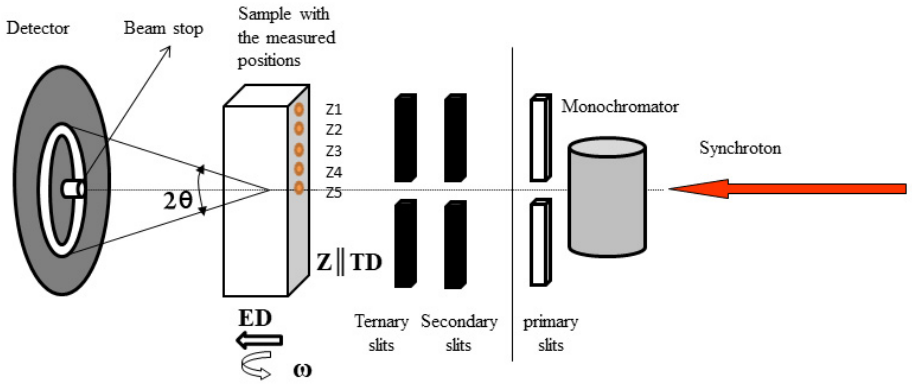

Figure 3.10-1: Texture measurement using synchrotron radiation.

The texture measurements were performed with high-energy synchrotron radiation using the high energy X-ray beam line HEMS@PetraIII DESY (Hamburg, Germany). A sketch of the setup is shown in Figure 3.10-1. The gauge volume depends on the beam cross-section which was 500 x 500 µm. The high penetration of the X-rays (87.7 keV energy), enabled the investigation of the 5 mm thick samples in transmission without any problem. The sample was fixed on an ω-stage that was mounted on an x-z-table (see Figure 3.10-1 and Figure 3.10-2). This arrangement enables to scan the sample along the z direction and rotate the specimen around the vertical ω-axis.

Using this setup, the extrusion direction was oriented parallel to the beam with the transverse direction pointing upwards (see Figure 3.10-1). Due to the high brilliance of the synchrotron beam, the investigations were completed after a relatively short measurement time.

An image plate detector (Perkin Elmer 1621) was positioned perpendicular to the transmitted beam at a distance of 1253 mm from the sample. Due to the low scattering angle obtained with the 0.14235 Å X-ray wavelength (87.7 keV) a set of complete Debye-Scherrer- rings containing information from both phases was collected on the detector. It can be assumed that this vertical position represents the upper surface of the specimen.

In order to find the exact position of the upper surface of the sample, the specimen was moved in 0.1 mm steps in a vertical direction during a “depth scan”. X-ray exposures (so called “single shots”) were taken at each position until the first diffraction spots were seen on the detector. It can be assumed that this vertical position represents the upper surface of th specimen. For obtaining complete pole figures, the sample was rotated around the ω-axis in steps of 5° from 0° to 180°; this resulted in 37 diffraction images for each z position. This type of texture measurement was performed for all selected 5 positions (Z1 to Z5). The first position (Z1) was 1mm from the surface. Positions Z2 to Z5 were 3.15 mm (Z2), 5.3 mm (Z3), 7.45 mm(Z4), and 9.6 mm (Z5) from the surface.

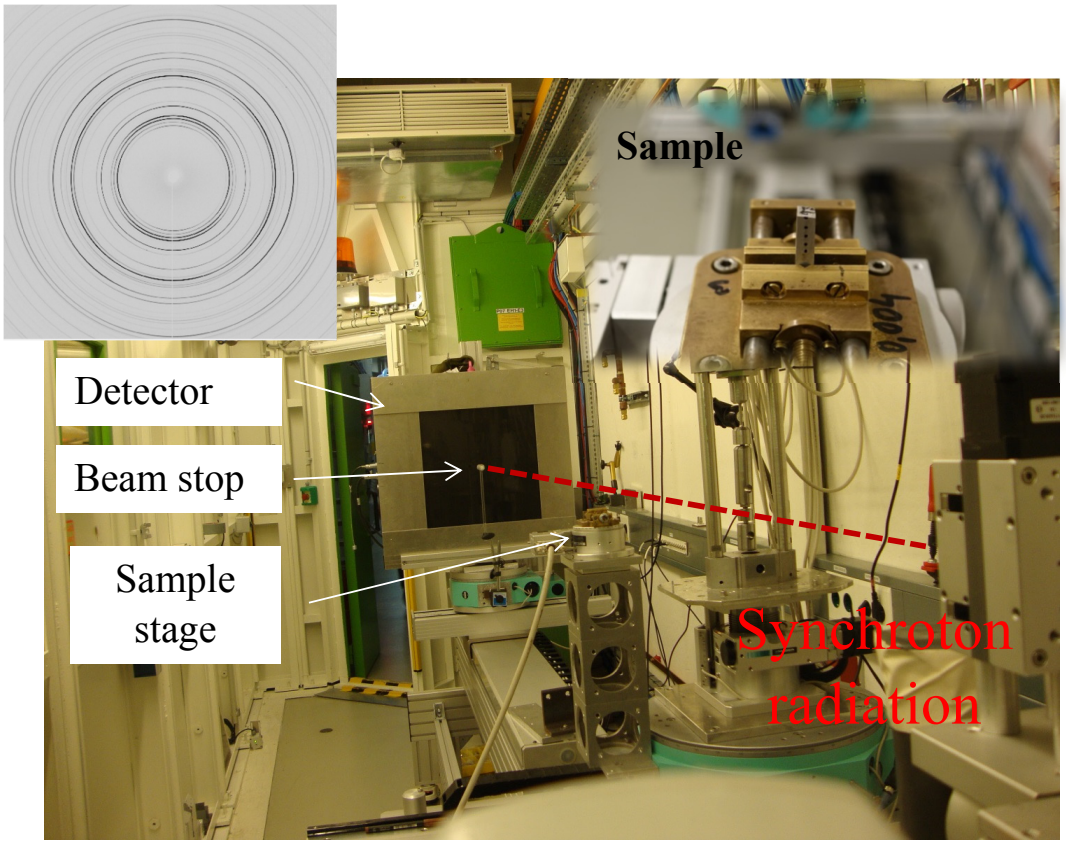

Figure 3.10-2: Photo of the beamline set-up used for the texture gradient measurements.

3.11 Texture gradient of the annealed samples

For the annealed samples the same measurement setup was used and the measurements were performed at the same positions that were used for the as received samples.

3.12 Texture gradient measurements made using a slit system

As will be discussed in section phase analysis, the Al40Mg60 material only consisted of the γ-phase after annealing at 400 °C for 12 hours. The cubic crystal structure of the γ- phase eases the calculation of the ODF. However, for texture measurement of the sample containing only the γ-phase, one has to solve two problems. Firstly, due to the very low intensity of some individual reflections, their intensity needed to be increased in order to decrease the error in

the ODF calculation. The intensity of the overlapping peak from the (411) and (330) reflections is very high compared to the other reflections and was thus masked in order to increase the intensity of the other reflections. Without such masking (see Fig. 3.12-1) there would be an overflow of the detector. Another problem is that reflections from low hkl planes, such as (110), are very close to those from air scattering of the primary beam. Increasing the sample to detector distance and using a second beam stop can help to reduce the influence of air scattering.

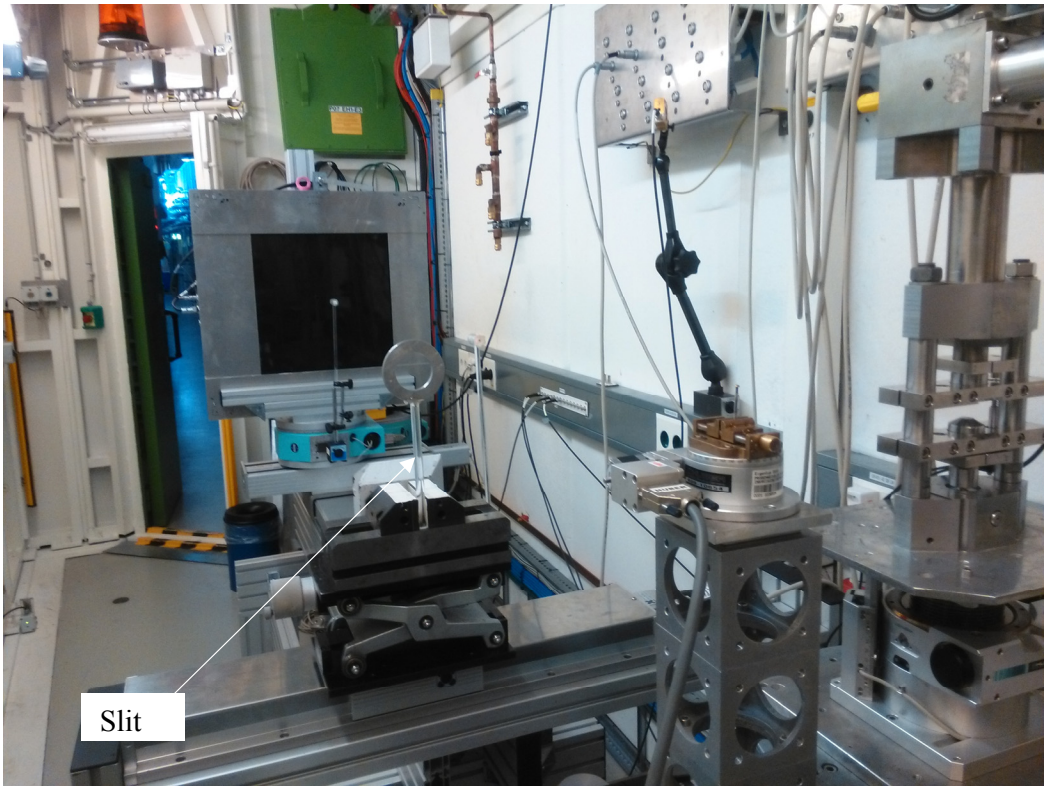

Figure 3.12-1: Experimental setup using the slit system.

4 Phase development during annealing

4.1 Phase analysis of the extruded materials

The diffraction pattern of the extruded Al40Mg60 and Al60Mg40 specimens are shown in Figures 4.1-1and 4.1-2. It should be mentioned that the phases were equally distributed over the cross section of the bar and the phase fraction was independent of position. In order to correct for the effect of texture on the peak intensity, quantitative phase analysis was performed on the sum of all 37 diffraction patterns taken for the pole figure measurements as discussed in the experimental section (section 3.7). Excellent agreement can be seen for each composition between the observed X-ray diffraction patterns and those calculated for the Al, Mg and the γ-phases. The crystallographic data for these phases was obtained from the International crystallography Database (ICD) and with the international table numbers 225, 194 and 227 for Al, Mg and γ-$Al_{12}Mg_{17}$-phases, respectively. The measured cell parameters are the same values as for pure elementary Al and Mg so that it can be concluded that no solid solution exists in the as received material. The material consists of Al, Mg and a very low fraction of γ-phase. As can be seen in Fig. 4.1-1and Fig. 4.1-2 this small amount of γ-phase (about 2 %) can be recognized by the (411) reflection, formed during the metallurgical processing so that it was already present in the as-received extruded material. Scudino et. al. [119] also found a small amount of the γ-phases at room temperature that formed during mechanical alloying, and discussed it in relation to the kinetics of phase formation during milling.

4.2 Phase development at 100 °C

As can be seen in Figure 4.2-1 and 4.2-2 for both Al40Mg60 and Al60Mg40 compositions, there is no differences in the composition of the phases in specimens after annealing at 100 °C for 2 and 12 h when compared to those in the initial materials. The phase compositions are the

same and consist of Al, Mg and a very low fraction of the γ-phase. This means that an annealing temperature of 100 °C is not high enough to provide a fast growth of the γ-phase. Moreover, annealing at 100 °C causes no peak broadening or peak shifts. However, for both compositions, the intensity of some peaks drops after annealing at 100 °C for 12 h compared to 2 h (Figure 4.2-3 and Figure 4.2-4).

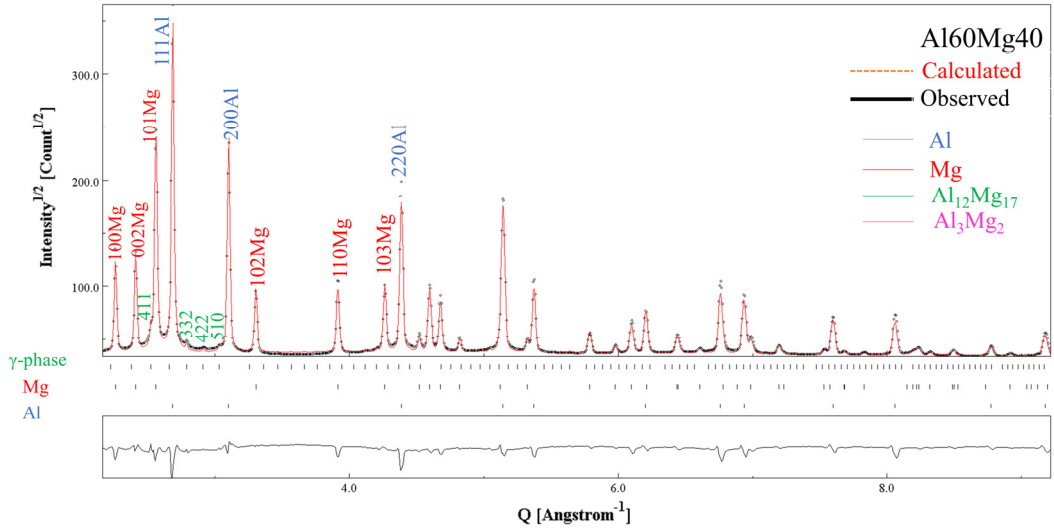

Figure 4.2-1: Rietveld refinement plot for the as received Al60Mg40 sample. Only in a selected range of reflections have been indexed.

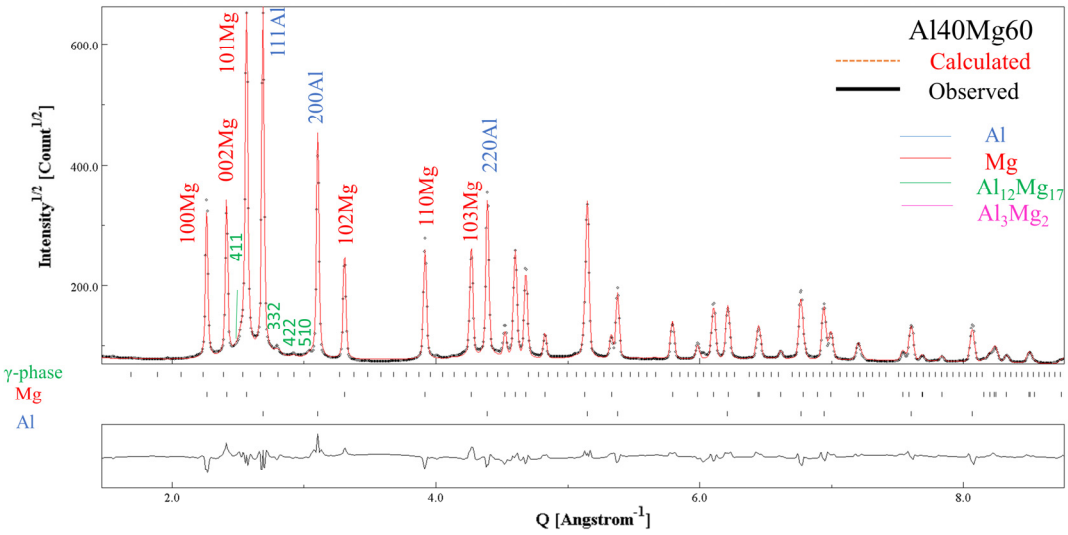

Figure 4.2-2: Rietveld refinement plot for the as received Al40Mg60 sample. Only in a selected range reflections have been indexed.

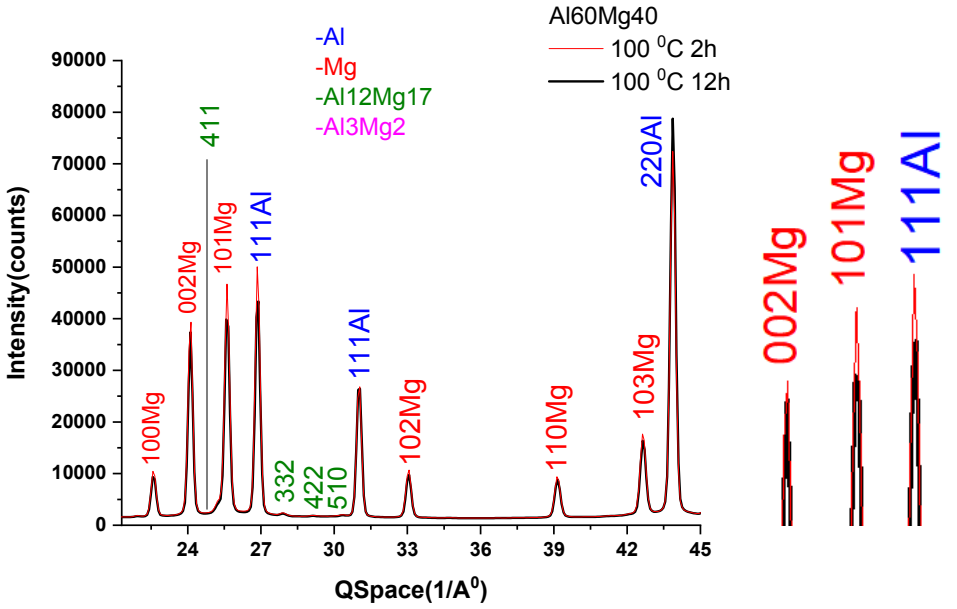

Figure 4.2-3: Indexed synchrotron radiation diffraction pattern of Al60Mg40 sample after annealing at 100 °C after 2 h and 12 h. No peaks other than those observed in the initial material were observed.

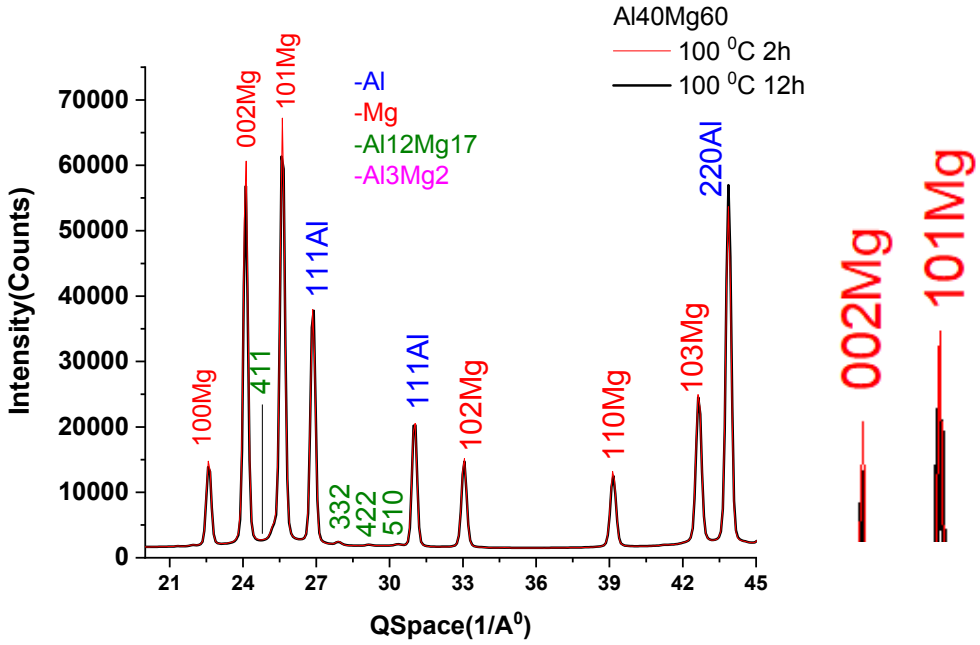

Figure 4.2-4: Indexed Synchrotron radiation diffraction pattern of Al40Mg60 sample annealed at 100 °C after 2 h and 12 h. No peaks other than those observed in the initial material were indicated. The healing of intern strain may cause the above described reduction in intensity.

4.3 Phase development at 200 °C

Annealing temperatures of 200 °C and 250 °C are interesting to study the formation of the γ and β-phases. Since 200 °C is high enough for γ-phase growth, a temperature of 250 °C has been selected to investigate if the growth of both the γ and β-phases can be observed.

As can be seen in the diffraction pattern for each composition (see Figure 4.3-1 and Figure 4.3-2) the fraction of the γ-phase increases with increasing annealing time from 2 to 12 h at 200 °C. The γ-phase grows at the expense of the Al and Mg phases. By isothermal annealing at 200 °C for 2 h and 12 h the growth rate and reaction kinetics could be determined. Figure 4.3-1 and Figure 4.3-2 show the diffraction patterns for each composition, Al40Mg60 and Al60Mg40, at room temperature after annealing at 200 °C for 2 and 12 h.

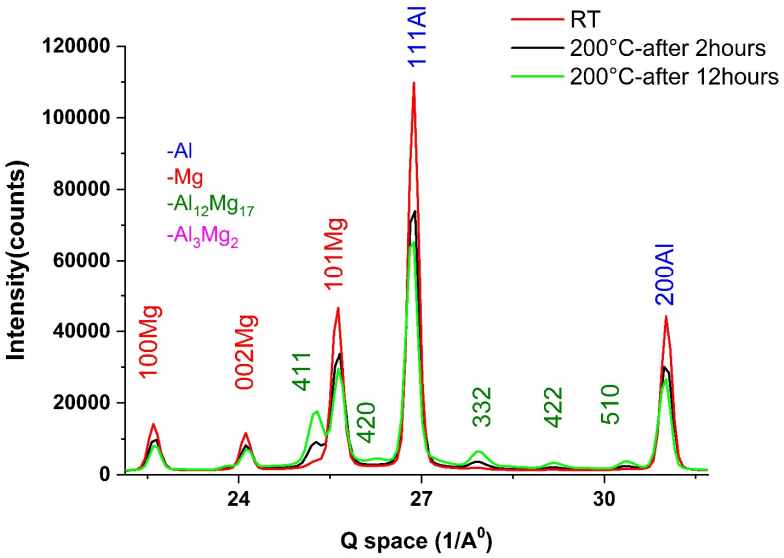

Figure 4.3-1: The diffraction pattern obtained from the Al60Mg40 sample annealed at 200 °C after 2 h and 12 h.

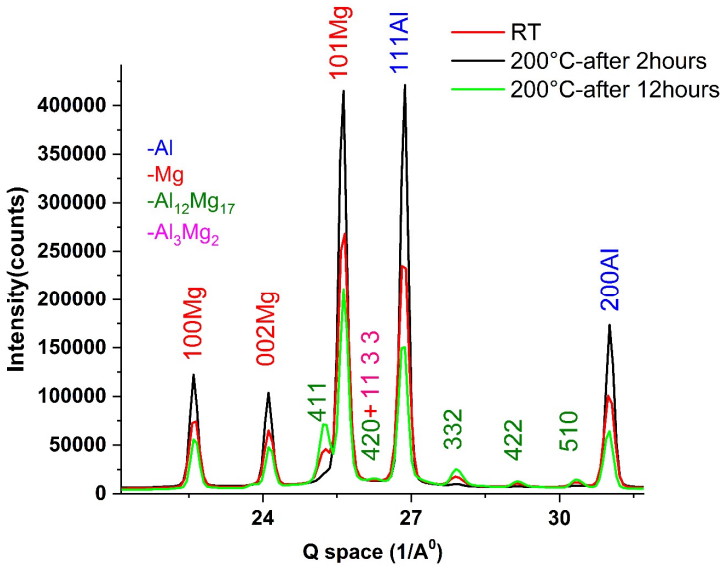

Figure 4.3-2: The diffraction pattern of Al40Mg60 sample annealed at 200 °C after 2 h and 12 h.

After 12 h annealing an increased background is observed around the (11 3 3) reflection of the β-phase. Since a β-phase peak would develop at this position after annealing at 250 °C, it is reasonable to interpret this with the formation of a very low fraction of the β-phase forming after annealing at 200 °C for 12 h.

4.4 Phase development at 250 °C

Annealing at 250 °C results in the β-phase being the major phase in both compositions. For both compositions at the beginning of annealing the amount of the β phase increased with annealing time. This trend continued for the Al60Mg40 compositions. For the Al40Mg60 composition the amount of γ-phase increased during annealing time between 2 h and 12 h (see Figure 4.4-1.). This latter observation might be explained by the higher thermodynamic stability of the γ phase in the Al40Mg60 composition as is indicated by the phase diagram (see Fig.4.9-2).

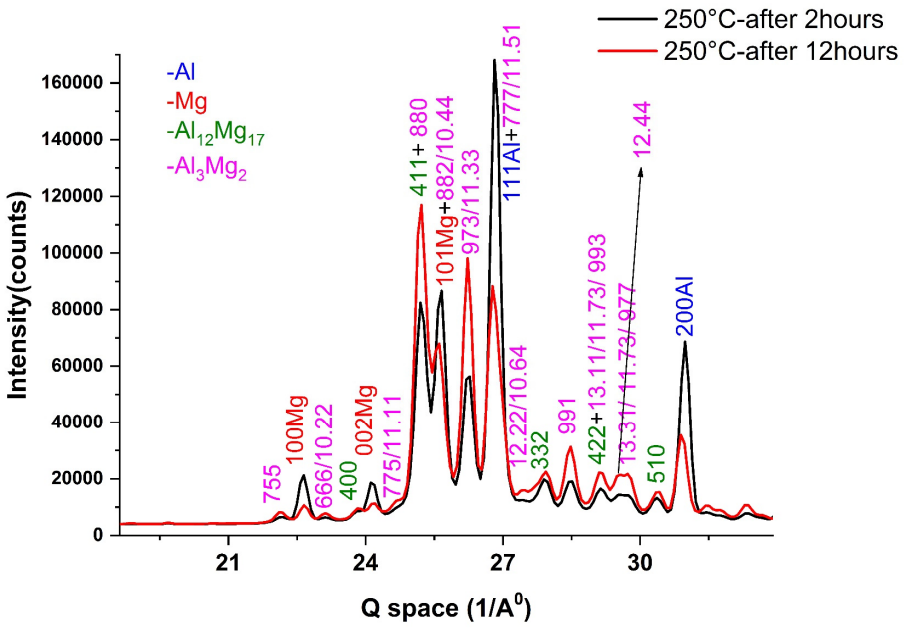

Figure 4.4-1: Diffraction patterns of Al60Mg40 sample after annealing at 250 °C for 2 h and 12 h from the ex situ measurements.

4.5 Advanced investigation concerning the phase selection between the γ-$Al_{12}Mg_{17}$ and β-Al_3Mg_2 phases

The results of ex situ phase analysis have shown that the γ- $Al_{12}Mg_{17}$- phase is the first phase to form in the Al-Mg system. In order to investigate the mechanism of formation and growth of the γ- and β phases an in-situ experiment (see section 3.5) was designed and performed. Figure 4-5.1 shows how the phases developed with annealing time at 200 °C in the Al60Mg40 composition. As can be seen the amount of γ- phase increases with annealing time. The XRD pattern has been fully indexed and consists of the Al, Mg and γ-phases. There is an excellent agreement between the observed X-ray diffraction pattern and that calculated for the γ-phase based on its crystal structure in the ICD database (number 158247). With increasing annealing time the intensity of the γ-phase reflections increase, which indicates an increase in the volume fraction of this phase. This intensity increase is combined with a move of the Al peaks to larger 2θ angles and peaks of the Mg reflections to smaller 2θ angles.

The γ- and the β- intermetallic phases were observed after annealing at 250 °C in both compositions. Figure 4-5.2 shows the XRD profiles for the Al60Mg40 composition during in situ measurements at 200 °C and 250 °C. The same phases were observed for both, the Al40Mg60 and Al60Mg40 composition.

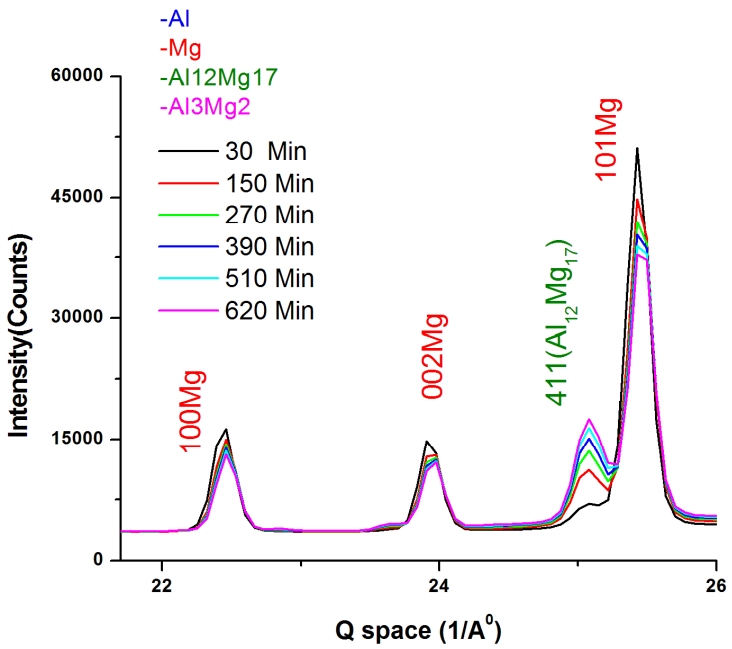

Figure 4-5.1: The diffraction pattern obtained in the in situ measurement of the Al60Mg40 sample at 200 °C.

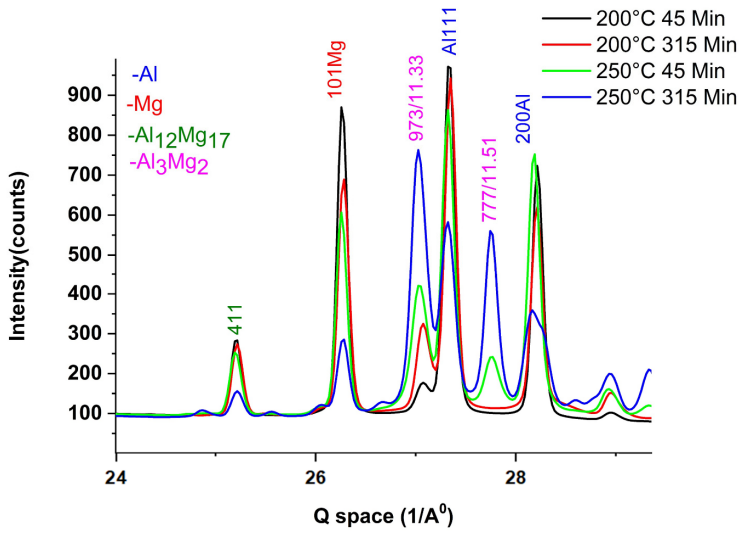

Figure 4-5.2: Comparison between the in-situ diffraction patterns obtained for the Al60Mg40 sample at 200 °C and 250 ° C.

4.5.1 The lattice parameter changes during in situ annealing at 200 °C

In Figures 4.5-3 and 4.5-4 the evolution of the lattice parameters determined by using the MAUD software package are shown for isothermal annealing at 200 °C as a function of the annealing time. The same trend was observed for both compositions. The lattice constants determined at room temperature do not deviate from those of the pure elements; thus implying that alloying has not taken place.

Lattice parameters at higher temperature depend on three factors, firstly the temperature. Secondly, diffusion can have an influence on the lattice parameters as a function of annealing time, when for example solid solutions or phase transitions occur. Thirdly, thermal stresses can arise due to different thermal expansion coefficients of the different phases. The development of the lattice constants of Aluminum and Magnesium can be described by two overlapping effects. On heating to the annealing temperature, there is thermal expansion due to the higher temperature, this results in an increase in the lattice constants for both the Al and the Mg phases. Since there is a further increase in the Al lattice constant (a) and a decrease in the Mg lattice constants (a and c) during isothermal annealing, another effect must be taking place. This effect is namely interdiffusion, which is the diffusion of Al into Mg and vice versa

in the interface layer of each other. Based on the phase diagram (see Fig.4.11-2), annealing at 200 °C results in up to 4 at.% Mg diffusing into Al which results in an Al(Mg) solid solution, while on the other side Mg can disolve up to 6 at.% Al and develops a Mg(Al) solid solution. Stress relaxation is believed to have taken place during heating to 200 °C and is not thought to contribute to the evolution of the lattice parameters during annealing.

The diffusion of Mg atoms, which have a bigger atomic size [120], into the Al lattice causes a tensile stress in Al and shifts the Al reflections to lower 2θ values which indicates an increase of the lattice constants of Al. Since Aluminum is smaller than Mg, it causes a compressive stress in Mg and shifts the Mg reflections to larger 2θ values and reduces the lattice constants of Mg.

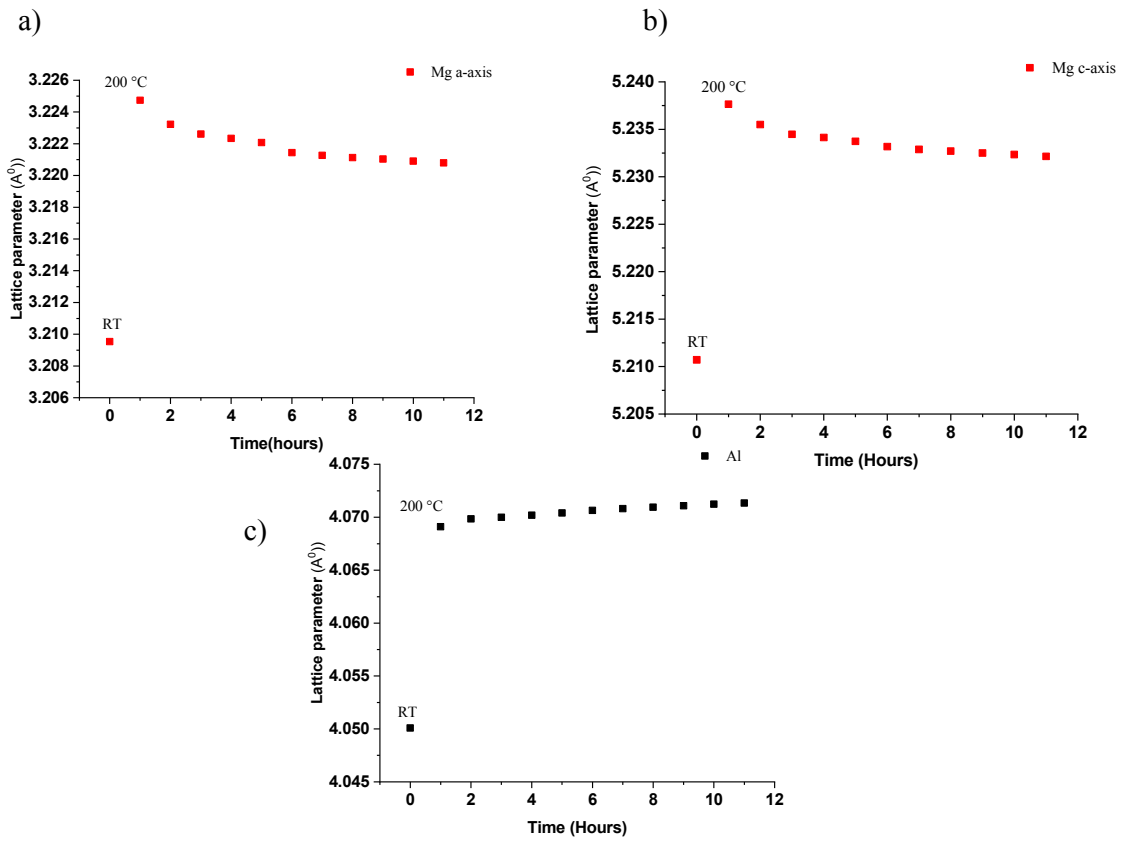

Figure 4.5-3: Lattice parameter evolution in the Al60Mg40 sample during heating up to 200 °C and during in situ holding at 200 °C, a) Mg a axis, b) Mg c axis and c) Al lattice parameter.

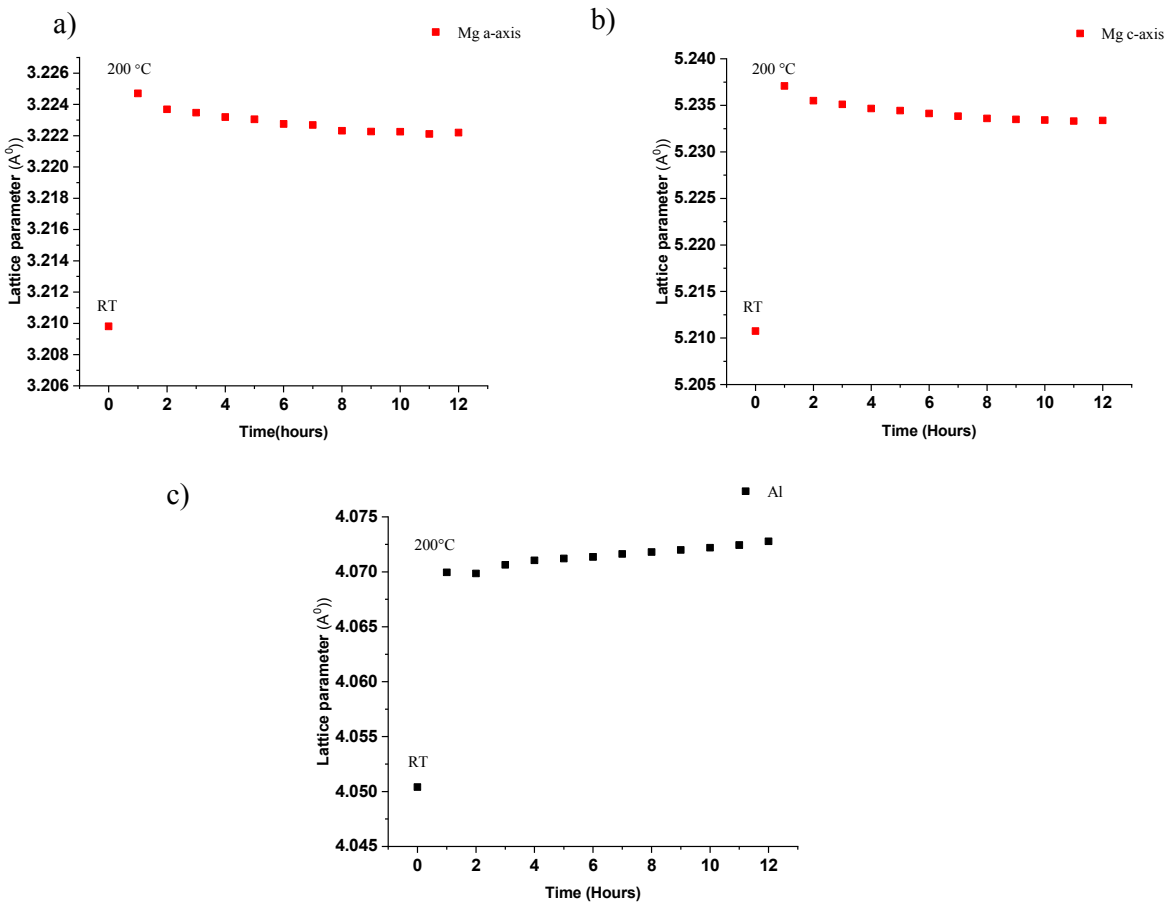

Figure 4.5-4: Lattice parameter evolution in the Al40Mg60 sample during heating up to 200 °C and during in situ holding at 200 °C, a) Mg a axis, b) Mg c axis and c) Al lattice parameter.

4.5.2 Quantitative phase analysis

In order to correct for the effect of texture on the intensity, quantitative phase analysis was carried out on the sum of the 37 diffraction patterns taken for the texture measurements as mentioned before. The detector images were converted to one-dimensional intensity versus 2θ spectra using the FIT2D software version 12_077 [117]. The 37 pictures were added together to eliminate the effect of the texture. For the Rietveld refinement method [114] the Materials Analysis Using Diffraction (MAUD) software version 2.8 was used [121]. The instrumental broadening was calibrated by using a standard NIST LaB_6 powder with the reference number 660c.The quality of the fit was indicated by a weighted profile R-factor (R_{wp}) and the

goodness of the fit. All fits were also checked graphically. The resulting phase fractions for in situ annealing at 200°C can be seen in Figure 4.5-5 and Figure 4.5-6.

A continuous linear growth relationship with time can be observed between the increasing fraction of γ-phase and the decreasing fraction of Al and Mg phases (Figure 4.5-5 and Figure 4.5-6).

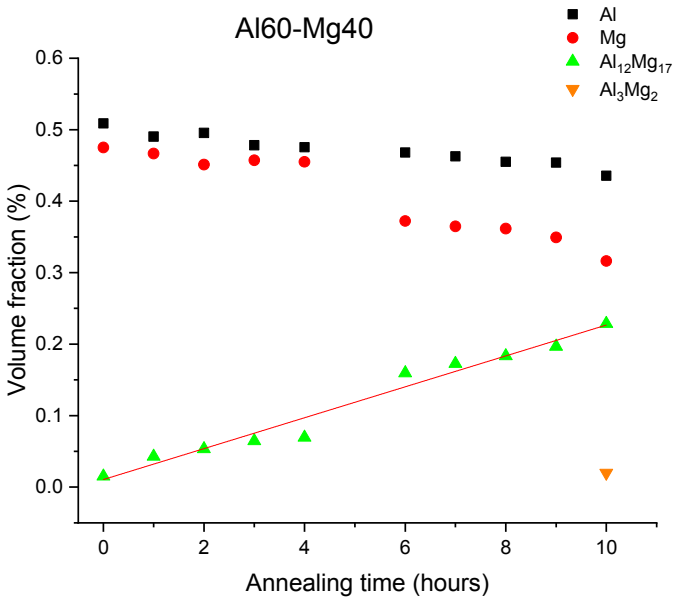

Figure 4.5-5: The results of quantitative phase analysis for the Al60Mg40 as a function of annealing time at 200 °C.

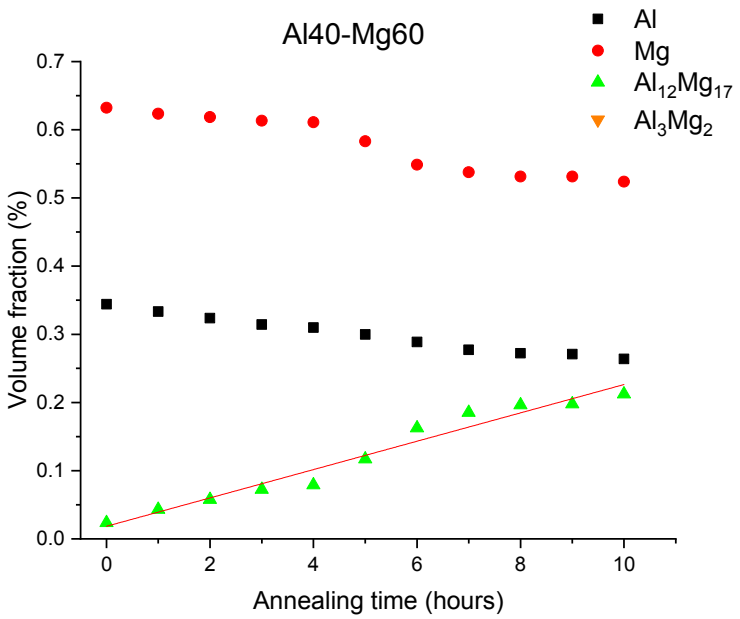

Figure 4.5-6: The result of quantitative phase analysis for the annealing at 200 °C for Al40Mg60.

4.6 Phase development at 300 °C

It can be assumed that a thermodynamic equilibrium will be achieved faster at 300 °C than at lower temperatures. This assumption is consistent with the results of the qualitative phase analysis after annealing of the Al40Mg60 composition (see Figure 4.6-2), in which the γ-phase is the main phase formed, and for the composition Al60Mg40 (see Figure 4.6-1) that contains the β-phase as the main phase. For the Al40Mg60 composition, four phases, the Al and Mg as well as γ-phase and the β-phase are present after annealing at 300 °C for 2 h, although the phase diagram indicates this temperature to be a single-phase region. After annealing for 10 h, the transformation to the γ-phase continues at the expense of the β-phase and to a lesser degree the Al and Mg phases. In the sample annealed for 12 h at 300 °C a very low fraction of the Al phase can still be detected by the presence of the (111) Al reflection. Applying the Rietveld refinement method shows that there is no change in the crystal structure of either the γ- and the β-phases after 12 h at 300 °C.

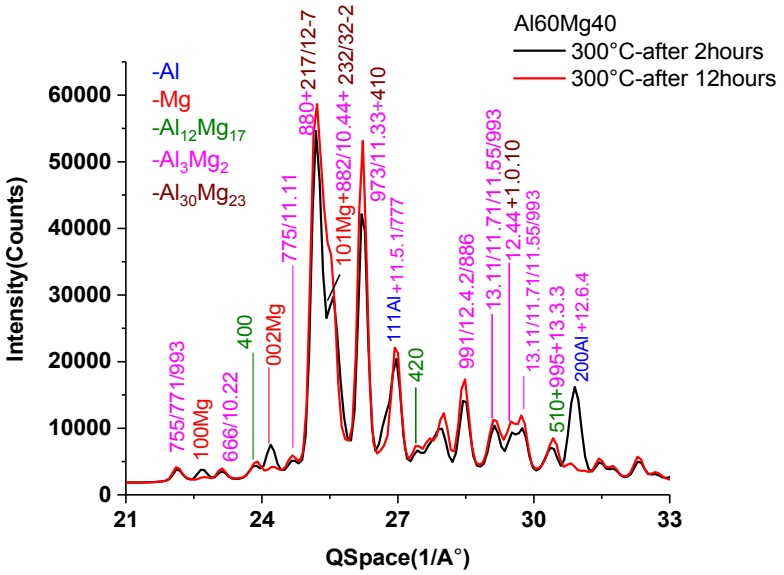

Figure 4.6-1: Indexed diffraction patterns obtained from the Al60Mg40 composition after annealing at 300 °C for 2 and 12 h.

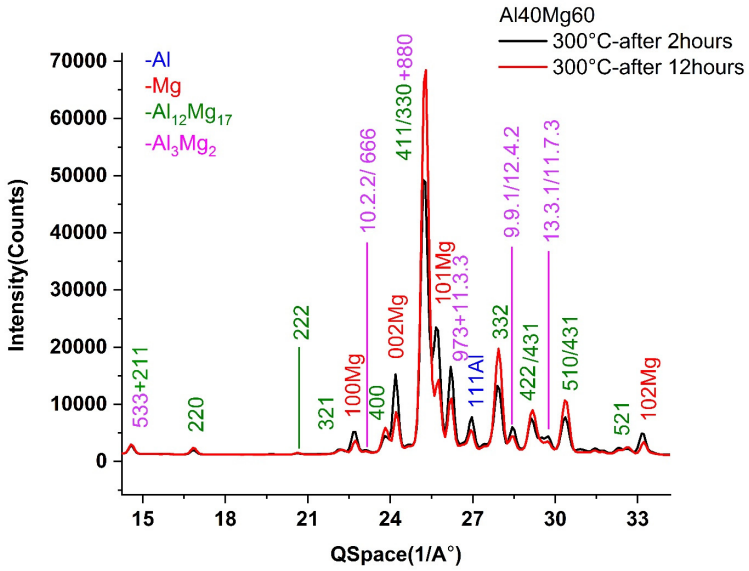

Figure 4.6-2: Indexed diffraction patterns obtained from the Al40Mg60 composition after annealing at 300 °C for 2 and 12 h.

In the sample Al60Mg40 after annealing at 300 °C for 2 h, there are four phases namely Al, Mg, γ-phase and the β-phase. After annealing for 12 h at this temperature the ε-phase-$Al_{30}Mg_{23}$ has also formed. The existence of the ε-phase was verified by Rietveld refinement and this phase remained present after annealing for 12 h at 350 °C.As Czeppe et al. [5] suggested that the sluggish formation of the ε-phase makes it difficult to predict the lower temperature of formation. Moreover, for the sample annealed at 300 °C the β- and γ-phases as well as a very low fraction of Al and Mg are present, as can be seen in Figure 4.6-3.

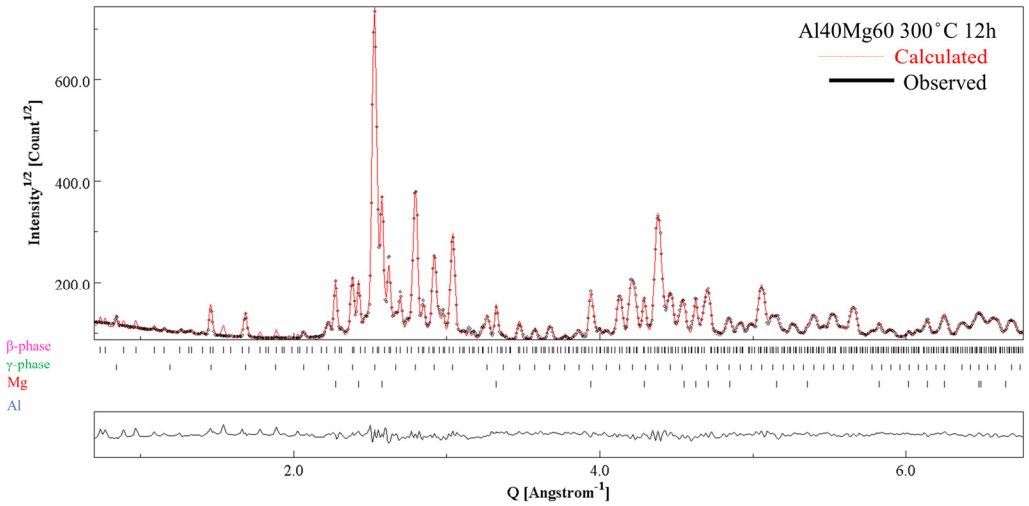

Figure 4.6-3: Rietveld refinement for the diffraction pattern obtained for the Al40Mg60 composition after annealing for 12 h at 300 °C.

4.7 Phase development at 350 °C

It is found that after annealing at 350 °C the material achieves for both compositions almost completely the phase equilibrium. For the Al40Mg60 composition annealed at 350 °C for 2 h (see Figure 4.7-2), the (111) Al reflection disappeared. This means that all the Al has transformed completely to the γ-phase. Only very low fractions of the Mg and β-phases remain. For the Al60Mg40 composition the Al and Mg phases completely disappear but the γ- and β-phases and a very low fraction of the ε-phase still are present after annealing at 350 °C for 2h (see Figure 4.7-1). For a composition near 56 at % Al that was annealed at 390 °C for 236 h, both Su et al. [3] and Liang et al. [122] observed that the ε-phase was formed which based on the phase diagram (phase diagram see Fig.4.9-2) has a very narrow composition range. On annealing at 410 °C, they observed the presence of the ε, γ- and β-phases, which is consistent with the assessed phase diagram (see Fig.4.9-2).

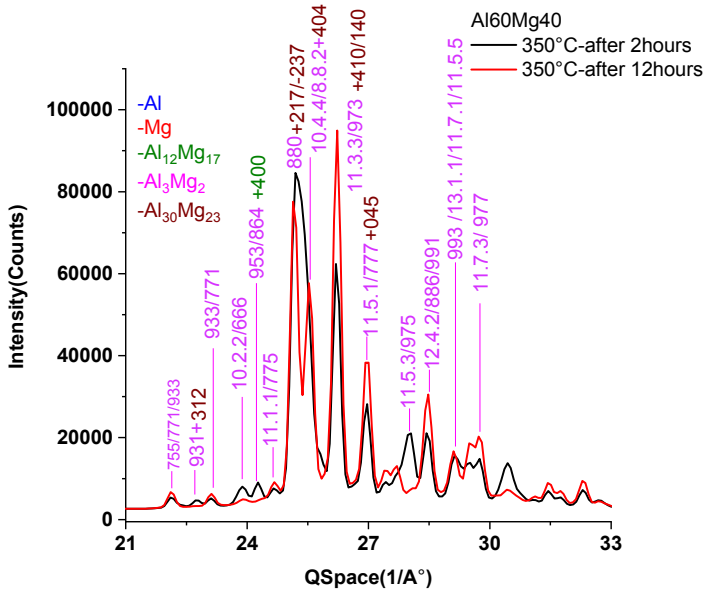

Figure 4.7-1: Indexed diffraction patterns obtained for the Al60Mg40 composition after annealing at 350 °C for different times.

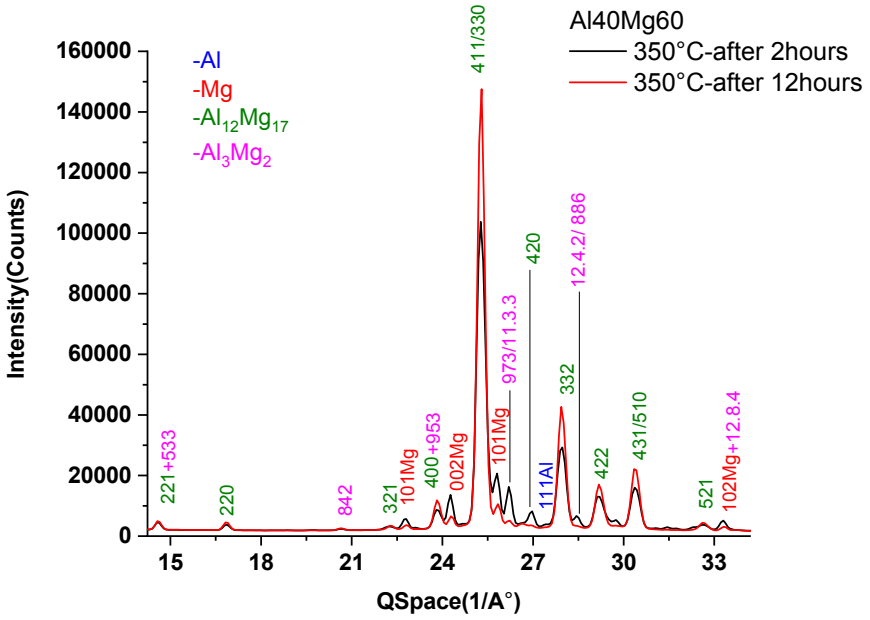

Figure 4.7-2: Indexed diffraction patterns obtained for the Al40Mg60 composition after annealing at 350 °C for different times.

4.8 Phase development at 400 °C

After annealing at 400 °C the specimens of both, the Al60Mg40 and Al40Mg60 compositions, reach the thermodynamic equilibrium. For the Al40Mg60 composition annealed at 400 °C for 2h (see Figure 4.8-2 and Figure 4.8-5) some Mg still remained in the material, but when annealed for 12 h (see Figure 4.8-2 and 4.8-6) this Mg was completely transformed to the γ-phase. This indicates that a 2 h annealing at this temperature is not sufficient to transform all the Mg to the γ-phase. The Rietveld refinement method also shows a small difference in the intensity between the calculated and the experimental data for some reflections of the γ-phase, as can be seen in Figure 4.8-6. Since the effect of texture was corrected, and the material does not have a strong texture after annealing at 400 °C, such intensity differences (between the calculated and experimental diffraction patterns) may be related to the site occupancy and a disordered crystal structure of the γ-phase [54]. Complete transformation into the γ-phase takes place by the diffusion of Mg, which is the mobile element, and the γ-phase is the only intermetallic phase formed. After annealing the

Al60Mg40 specimen (with 57 at. % Al) at 400 °C for 2 h (see Figure 4.8-1 and Figure 4.8-3) the observed phases correspond to the result found by Su et al. [3] and Liang et al. [122]. They observed for a Mg-56 at% Al alloy annealed at 410 °C for 480 h and at 420 °C, for 483 and 240 h and 430 °C for 483 h both the β- and γ-phases. This can be seen in Table 4.9-4. The remaining γ-phase fraction, will fall on further annealing and transform completely to the β- phase and the system will reach its thermodynamic equilibrium. This means that the observed phases for both compositions Al60Mg40 and Al40Mg60 after annealing at 400 °C for 12 h correspond to those expected by thermodynamic equilibrium (see Figure 4.8-4).

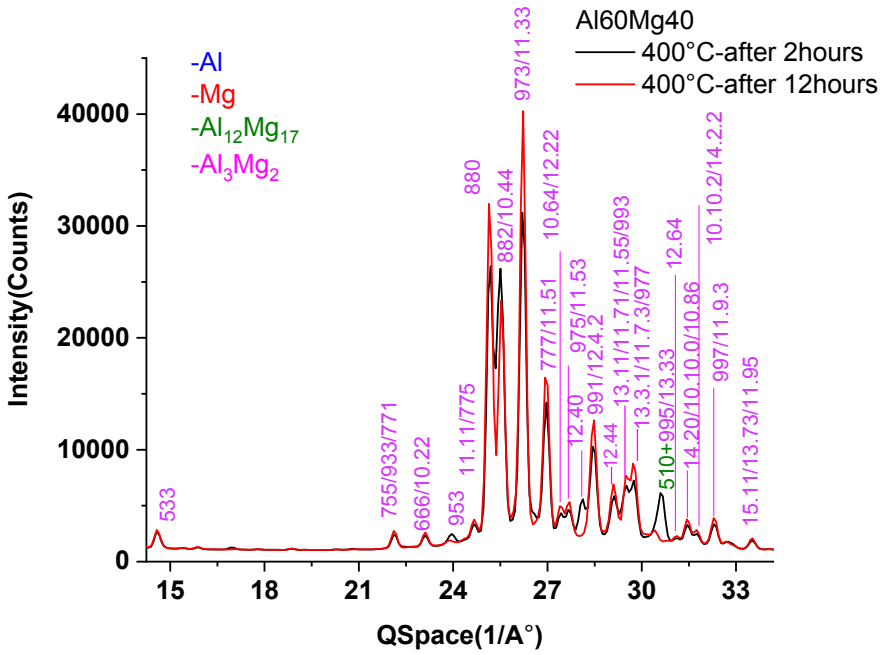

Figure 4.8-1: Indexed diffraction pattern obtained for the Al60Mg40 composition after annealing at 400 °C for different times.

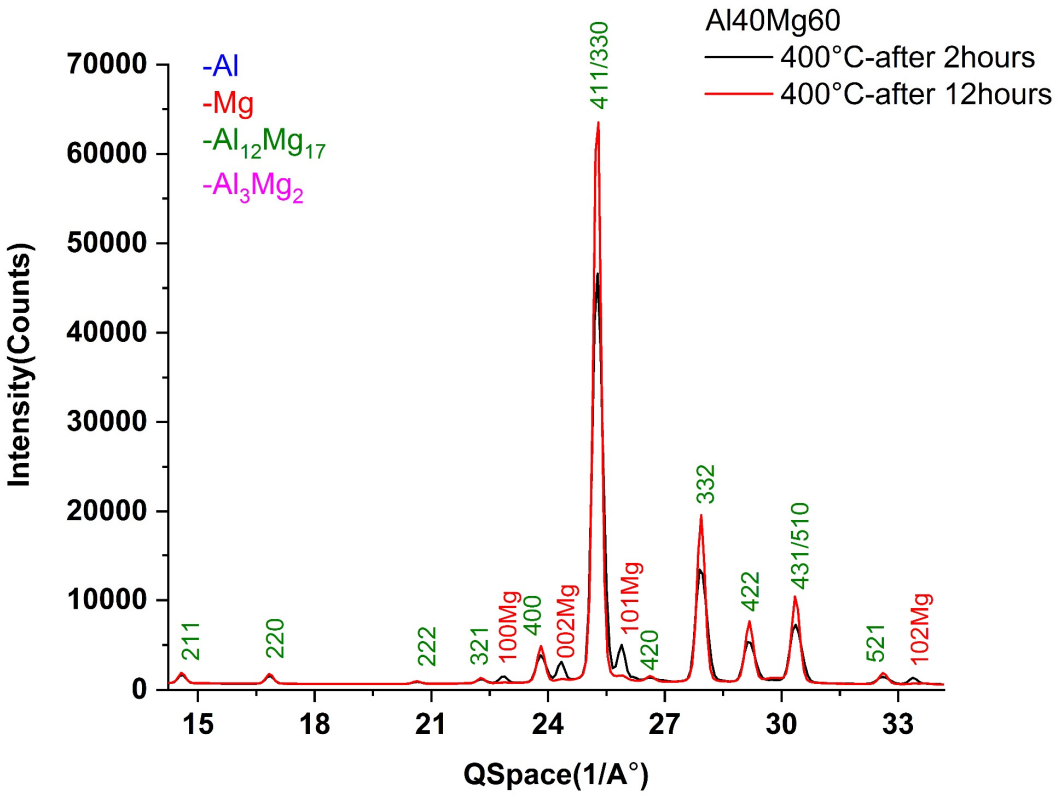

Figure 4.8-2: Indexed diffraction patterns obtained for the Al40Mg60 composition after annealing at 400 °C for different times.

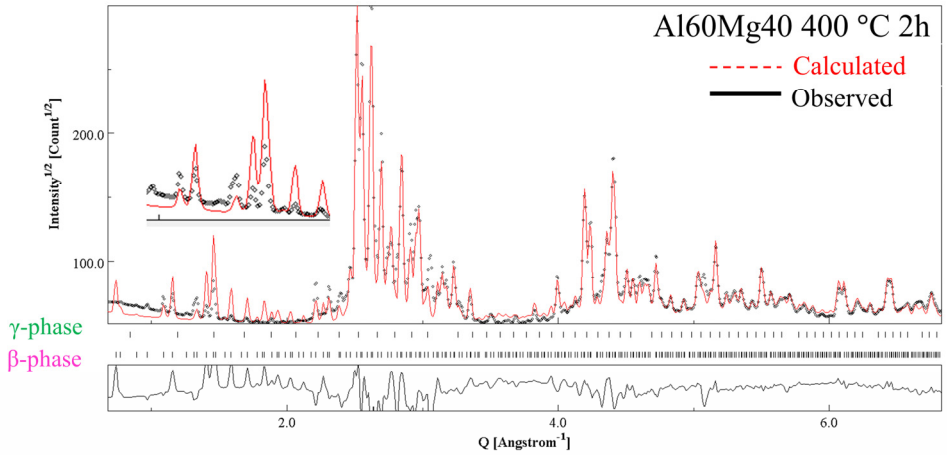

Figure 4.8-3: The Rietveld refinement plot for the Al60Mg40 composition after annealing at 400 °C for 2 h.

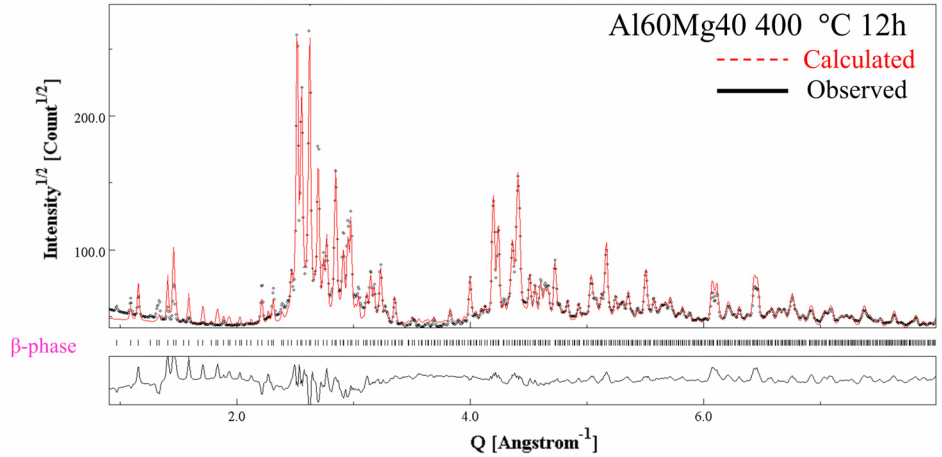

Figure 4.8-4: Rietveld refinement plot for the Al60Mg40 composition after annealing at 400 °C for 12 h.

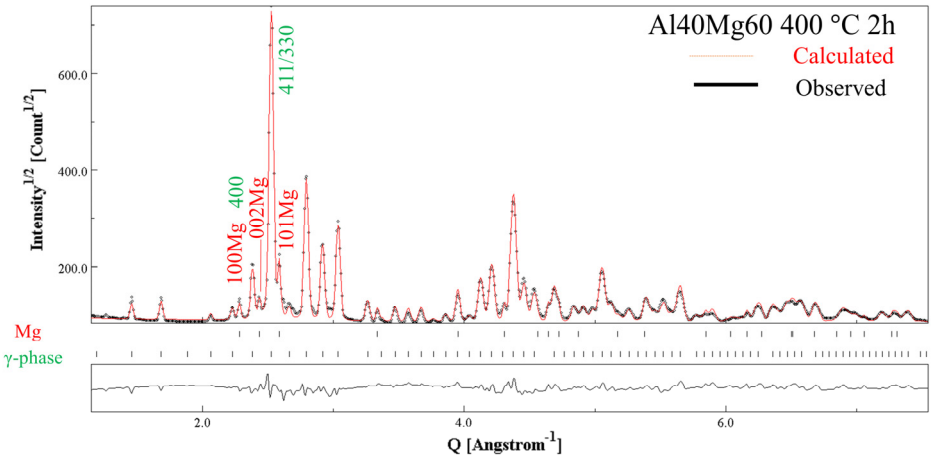

Figure 4.8-5: Rietveld refinement plot of the Al40Mg60 composition after annealing at 400 °C for 2 h.

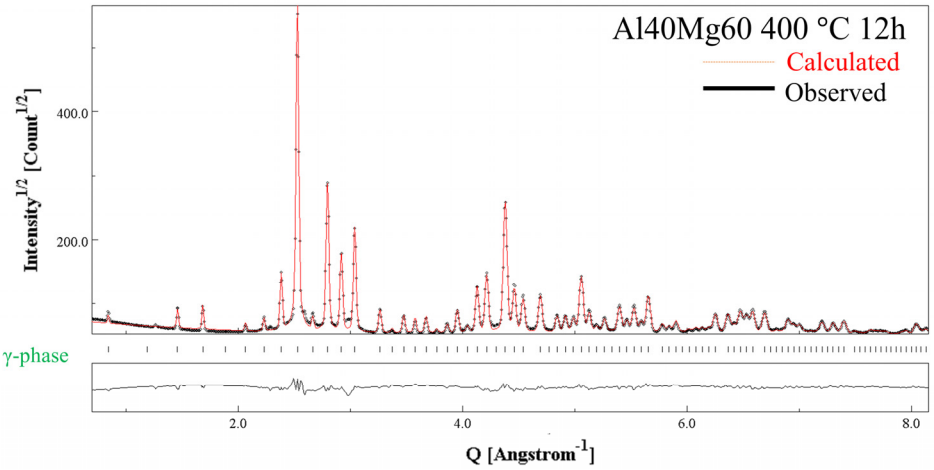

Figure 4.8-6: Rietveld refinement plot of the Al40Mg60 composition after annealing at 400 °C for 12 h.

4.9 Discussion of phase analysis

During the reaction of two solid metals with each other in a binary system, the formation of an intermediate phase, which is in equilibrium at the temperature of phase formation, is anticipated [123]. However, in many reactions, phase formation depends on the solubility range, diffusion coefficients of atomic species and thermodynamics [123-126]. From the diffusion point of view, when two phases are coupled, the growth of a specific phase depends on the diffusivity of species within it and its neighboring phases. The diffusion rate between

two phases depends on amongst others factors the grain size, grain boundary migration and dislocation density. Moreover, each atomic species tries to surround itself with the maximum number of unlike atoms [127].

Vacancy motion resulting from concentration gradients leads to a diffusion flux of atoms, called interdiffusion, which has been discussed in the theoretical section and is temperature and concentration-dependent. In the Al-Mg system, based on previously mentioned results, it can be concluded that the reaction between Al and Mg causes the diffusion of Al into Mg and Mg into Al which is then followed by nucleation of the γ-phase. After formation and growth of the γ-phase, the β-phase is formed.

For both compositions, Al60Mg40 and Al40Mg60, only the formation the γ- and β-phase was observed over the temperature range 200 and 250 °C. There are examples in the literature that represent the intermetallic phase formation between aluminum and magnesium in the solid state experimentally and a number of kinetic equations and activation energies have been reported. The formation of the γ- and the β-phases were observed in Aluminum 6082 that had been diffusion welded to magnesium AZ31 [13] and also in studies using a diffusion couple assembly or other bonding methods as described by Brennan et. al [22] [128], Fujikawa et al. [25] and Tanguep Njiokep et al. [129]. Another result was that the Mg-rich γ-phase was observed on the Mg side while the Al-rich β-phase was observed on the Al side [21][49].
A principal difference between the diffusion couple study and phase reaction in composites is that due to the high density of boundaries between Al and Mg grains, the annealing time is very short until the first reactions can be observed. However, Su et. al [3] suggested 250 °C as a lower temperature limit for the formation of the ε-phase for a composition around 44 at.% Mg. After 12h annealing at 250 °C the existence of the ε-phase was not observed in the Al60Mg40 composition, which has nearly 42.5 at.% Mg. The reason that the ε-phase was not observed can be explained by thermodynamically and kinetically unfavorable conditions in

the temperature range lower than 250 °C [5]. Moreover, Czeppe et. al [5] believed that the ε-phase did not form because of its very small solubility range and its sluggish formation. As mentioned in the introduction, the β-phase is thought to undergo a first order phase transformation to a β'-phase with 293 atoms per unit cell [6] [49]. This β' has the space group R3m and the international table number 160, which has no inversion symmetry. Its lattice parameters are a = 11.9968 Å and c = 48.9114 Å. The crystal structure of the β phase was investigated first by Samson [48] and the β' phase was reinvestigated recently by Feuerbach et al. [49]. The present in-situ experiment do not show any β' reflections and also no other metastable phases could be confirmed.

The sequence of phases for reactions in Al40Mg60 and Al60Mg40 metal matrix composites was found to begin with the formation of the γ-phase followed by the formation of the β-phase. To the author's knowledge, the current study is the first in situ-investigation that has observed the formation and growth of the γ-phase as the first phase. It should be mentioned that in some previous theoretical modelling work like in the study on ultrasonic welding of Aluminum 6111 to MgAZ31 alloys [130], the formation of the γ-phase prior to the β-phase was suggested. Also from the general model proposed by Philibert [123] the formation of the γ-phase can be deduced. However, many previous investigations like the diffusion couple study by Tanguep Njiokep et al. [129] reported a simultaneous growth of both the γ and the β-phase. Later on, Brenann et. al. [128] and Funamizo and Watanabe [21] observed a difference in their investigation after comparing the value of the activation energy for interdiffusion and the layer growth. Funamizu and Watanabe [21] observed a linear concentration profile for the β- and γ-phases, which formed in-between Al and Mg. In their study, they suggested a ten times higher interdiffusion coefficient for the β-phase than the γ-phase. Brenann et al. [128] investigated the kinetics more intensively and based on layer growth they determined an activation energy of ~165 kJ/mole for the growth and an activation energy for an effective interdiffussion of ~123 kJ/mole, and for an integrated interdiffusion a value of ~147 kJ/mole,

whereupon these values for the β-phase are nearly the same. They suggested that this difference may indicate that a parabolic growth does not occur for the growth of the γ-and β-phases and the growth of γ-phase may deviate from a pure diffusion controlled mechanism. Moreover, applying Rietveld refinement showed that there was a linear relationship between the volume fractions of the γ-phase and annealing time. The volume fraction of the γ-phase increased while the volume fraction of Al and Mg decreased. In a diffusion couple between the aluminum alloy 1060 and pure magnesium in the temperature ranges 300 - 400 °C Xiao et. al suggested a mixed grain boundary and lattice diffusion mechanism for the formation of the γ-phase and a diffusion-controlled mechanism for the formation of the β-phase [81]. In principle, two cases of migrating interfaces can be distinguished. Firstly, there is a very slowly moving boundary, the motion of which is largely independent on the diffusion rate and the growth is described as interface controlled. Secondly, a very highly movable boundary can occur, which moves as rapidly as the rate of diffusion. The growth rate then is determined almost completely by diffusion and categorized as diffusion controlled [26].

As can be seen in the Figures 4.7-1 and 4.7-2, the results of the quantitative phase analysis show that the growth of the γ-phase is linear. There is agreement but also some minor discrepancies to the value of the previously reported experimental observations in that the β-phase has a higher growth rate constant. Brennan et al. [128] reported an activation energy of 165 ($\frac{\text{KJ}}{\text{mol}}$) and 85 ($\frac{\text{KJ}}{\text{mol}}$) for the γ-phase and β-phase, respectively. The results are consistent with the values reported by Tanguep et al. [129] and, Li et al. [131]. They also reported a higher interdiffusion coefficient and a lower activation energy for both, growth and interdiffusion of the β-phase compared to the γ-phase [128].

A comparison between the activation energies and pre-exponential factors based on and Brennan can be seen in table 4.9-1.

This result can be interpreted by the fact that the growth of the γ-phase is dominated by the interface migration kinetics rather than by diffusion and indicated that there is a nucleation barrier to the formation of the β-phase. Tanguep Njiokep et. al. [129] and Funamizo and Watanabe [21] also suggested for the β-phase a completely diffusion-controlled mechanism. It was suggested in both a diffusion couple study [128] and diffusion welding study of Al and Mg [130] that during this kind of phase formation the reaction product grows toward the Mg rather than towards the Al, indicating a Kirkendall effect. This kind of kinetic behavior was also observed in the binary systems Cu-Sn. In the Cu-Sn binary system by using a diffusion couple, the formation of the two intermetallic ε- and γ-phases was observed in the temperature range 250 °C to 350 °C. An interface reaction and volume diffusion rate-controlling process was reported. After comparing the diffusion rate it was indicated that the reaction is controlled by grain boundary diffusion and at the second stage is controlled by volume diffusion [132].

Table 4.9-1: A comparison of the activation energy and growth constants for the γ- and β-phases determined in different studies.

Phase	K_0 (m^2S^{-1})	Q ($kJmol^{-1}$)	Reference
β	3.5×10^{-8}	69	Tanguep Nijokep [129]
β	2.2×10^{-8}	57	Li [131]
β	2.2×10^{-6}	85.9	Brennan [128]
γ	0.1	165	Tanguep Nijokep [129]
γ	0.4	106	Li [131]
γ	0.36	165.1	Brennan [128]

Figure 4.9-1 represents schematically the first step of phase formation in the binary Al-Mg system based on the result of this investigation.

A general overview of phase development for the Al60Mg40 and Al40Mg60 compositions can be found in Table 4.9-2 and Table 4.9-3 and a quantitative description is given in Figures 4.9-3 and 4.9-4.

As can be seen in Tables 4.9-2 and 4.9-3, the β-phase grows in both compositions after annealing at 250 °C for 2 h. On further annealing at 250 °C for 12 h the β-phase is the majority intermetallic phase that developed in the Al60Mg40 composition, whereas in the Al40Mg60 composition the γ-phase was predominant. Besides these two phases, the Al and Mg phases are still present in both compositions.

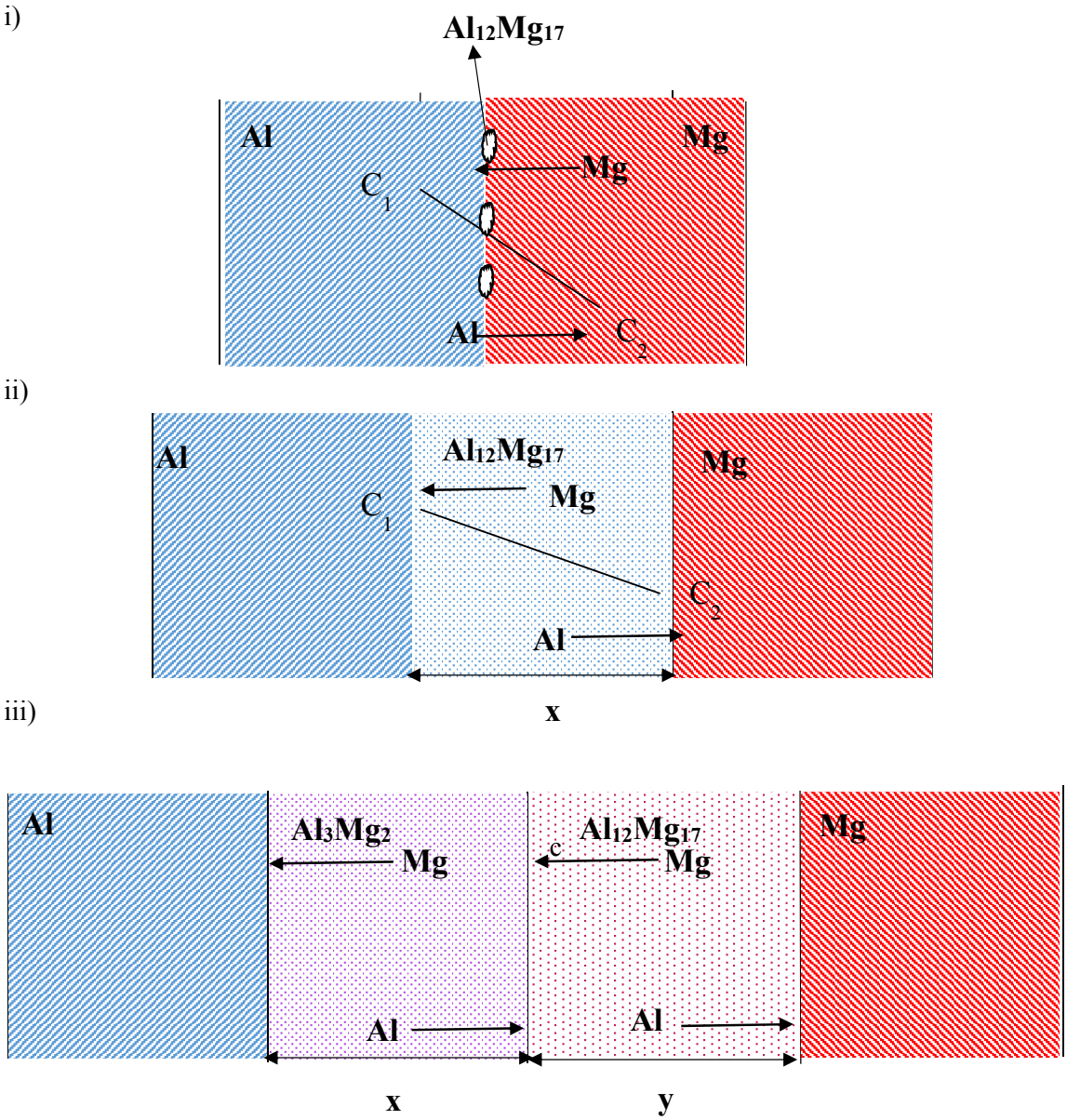

Figure 4.9-1. Schematic representation of phase formation in the binary Al-Mg system i) Nucleation of the $Al_{12}Mg_{17}$ ii) growth of the $Al_{12}Mg_{17}$ and iii) growth of the Al_3Mg_2 phase after the $Al_{12}Mg_{17}$ has grown to the critical thickness.

This indicates that in spite of the higher growth rate constant of the β-phase, the Al40Mg60 composition facilitates the formation of the γ-phase and the Al60Mg40 composition the formation of the β-phase. The alloy compositions are rather close to the stoichiometric compositions of the respective phases.

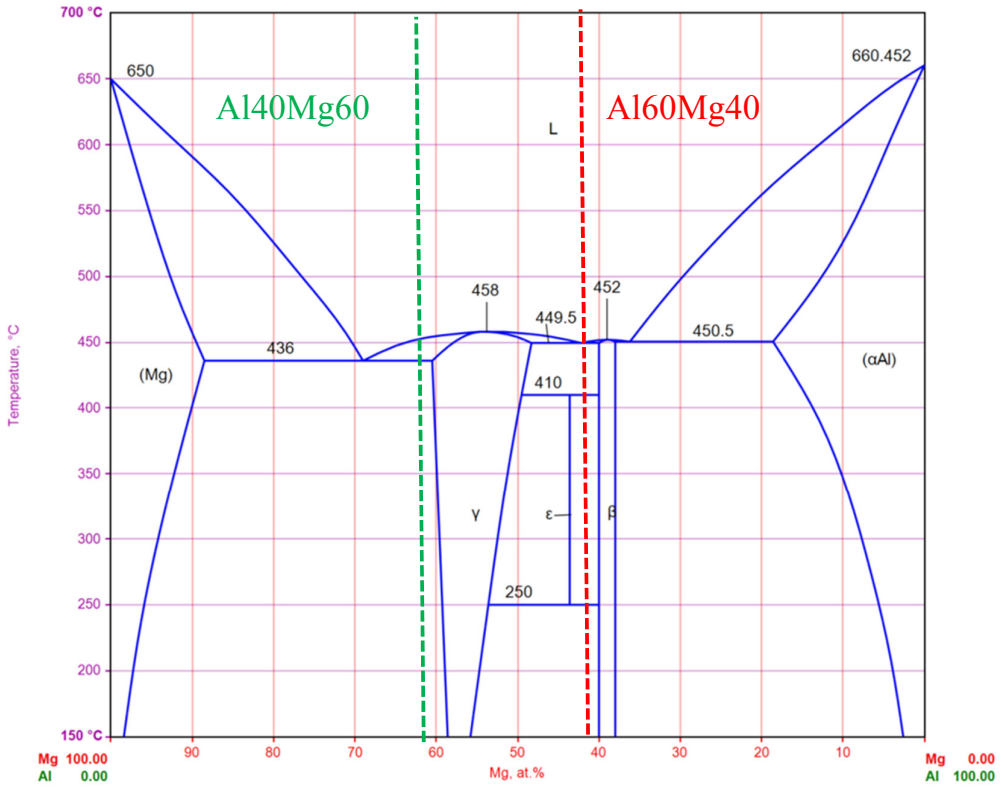

Figure 4.9-2: The phase diagram based on the assessments of Liang et al. [122] and Murray [1] according to MSI Eureka.

Table 4.9-2*:* Summary of the phases after annealing as determined by ex situ analysis of the Al60Mg40 composition (S strong, W weak, VW very weak)

T (°C)	Time (h)	Al	Mg	$Al_{12}Mg_{17}$ (γ-phase)	Al_3Mg_2 (β-hase)	$Al_{30}Mg_{23}$ ε -phase
100	2	S	S	VW		
	12	S	S	VW		
200	2	S	S	W		
	12	S	S	S	VW	
250	2	S	S	S	S	
	12	S	S	W	S	
300	2	W	S	S	S	
	12	VW	S	S	S	
350	2		S	S	W	
	12		W	S	VW	
400	2		VW	S		
	12			S		

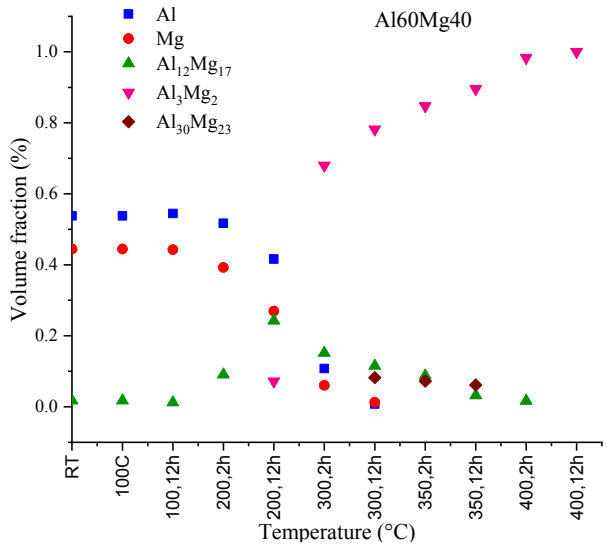

Figure 4.9-3: The quantitative phase analysis results for the Al60Mg40 composition.

Table 4.9-3: Summary of the phases after annealing as determined by ex situ analysis of the Al40Mg60composition (S strong, W weak, VW very weak)

T(˚C)	Time (hours)	Al	Mg	$Al_{12}Mg_{17}$ (γ-phase)	Al_3Mg_2 (β-hase)	$Al_{30}Mg_{23}$ ε -phase
100	2	S	S	VW		
	12	S	S	VW		
200	2	S	S	W		
	12	S	S	S	VW	
250	2	S	S	S	W	
	12	S	S	S	S	
300	2	W	W	S	S	
	12	VW	VW	S	S	W
350	2			S	S	W
	12			S	S	VW
400	2			W	S	
400	12				S	

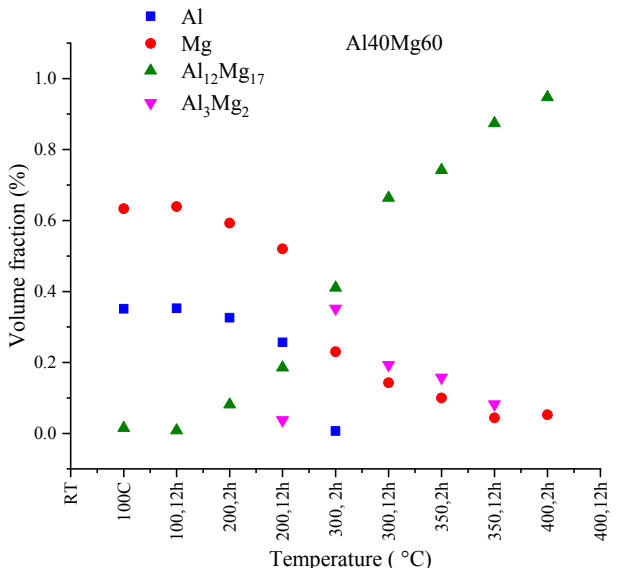

Figure 4.9-4: The quantitative phase analysis result for the composition Al40Mg60.

For the Al40Mg60 composition the growth of the γ-phase continues at 300 °C and the amount of Al-phase decreases and this trend is continued by further isothermal annealing at 300 °C. The analysis of material annealed at 300 °C by Rietveld refinement shows disordering of the γ-phase and β-phases as evidenced by the intensity of some reflections. As mentioned in section 2.1 the β -phase has an extended homogeneity range [54]. The crystal structure of the β-phase in a fully occupied unit cell contains 1832 atoms, where a partially occupied unit cell with 1168 atoms per unit cell was observed. This significant number of vacancies is probably one reason for the deviation between the calculated results and the experimental observation in this investigation, which were obtained by applying Rietveld refinement. As mentioned earlier, the ε-phase was observed as third phase in the Al60Mg40 composition after annealing for 12 h at 300 °C, and still existed up to 350 °C. Brubaker et. al. [133] also observed ε-phase over the temperature range 360 °C to 370 °C in an Al-Mg diffusion couple. Czeppe et. al. [5] attempted to clarify the discrepancies in the literature for the central part of Al-Mg phase diagram. They suggested an upper temperature limit for the presence of the ε-phase to be 427 °C. The ε-phase has a very narrow solubility range and is thermodynamically and/or kinetically unfavorable to form [5]. It should be also mentioned that the diffusion layer of the ε-phase is too narrow to be detected with methods such as SEM [5]. There is a complete consumption of the Al phase after annealing at 350 °C for 2h, in spite of the remaining presence of the Mg phase. This could be explained by Al having a higher diffusion coefficient than Mg and therefore being consumed faster. After consumption of the pure Al phase, the β-phase serves as a source for Al to facilitate the formation of the γ-phase.

The Al40Mg60 composition achieves thermodynamic equilibrium after annealing at 400 °C for 2 h, which is in agreement with the phase diagram of Okamoto [4] and the assessed phase diagram of Liu and Murray [1]. By further isothermal annealing the system reached its thermodynamic equilibrium with its composition. For the Al60Mg40 composition, the

thermodynamic equilibrium is attained after annealing at 400 °C for 2 h. However, there is a small difference in the findings between the studies of Su et al. [3], Liang et al. [122] and those of this investigation (see Table 4.9-4). Those studies observed the γ+β two-phase region at 420 °C. However, Brubaker et al. [133] found for γ+β to be in thermodynamic equilibrium when it was annealed at 375 °C for 14 days.

Table 4.9-4: Summary of the result reported by Su et al. [3] and Liang et al. [122] after annealing.

Nominal Compositions (at.%)	Annealing Treatments	Su et al. [3]	Liang et al.[122]
56	410 °C/480 h	β+γ+ε	β+γ+ε
56	420 °C/240 h	β	*β*
56	420 °C/483 h	γ+ β	γ+ β
56	430 °C/483 h	γ+ β	γ+ β

Both Su et al. [3] and Liang et al. [122] have found only the β-phase for a composition near 61 at.% Al after annealing at 420 °C for 240 h. However, Brubaker [133] found both the γ and β-phases present within the temperature range of 375 to 420 °C. Su et al. [3] and Liang et al. [122] suggested a two phase γ and β-phase region exists over the temperature range 420 - 430 °C. In their investigation a three phase region was suggested at a temperature of 410 °C.

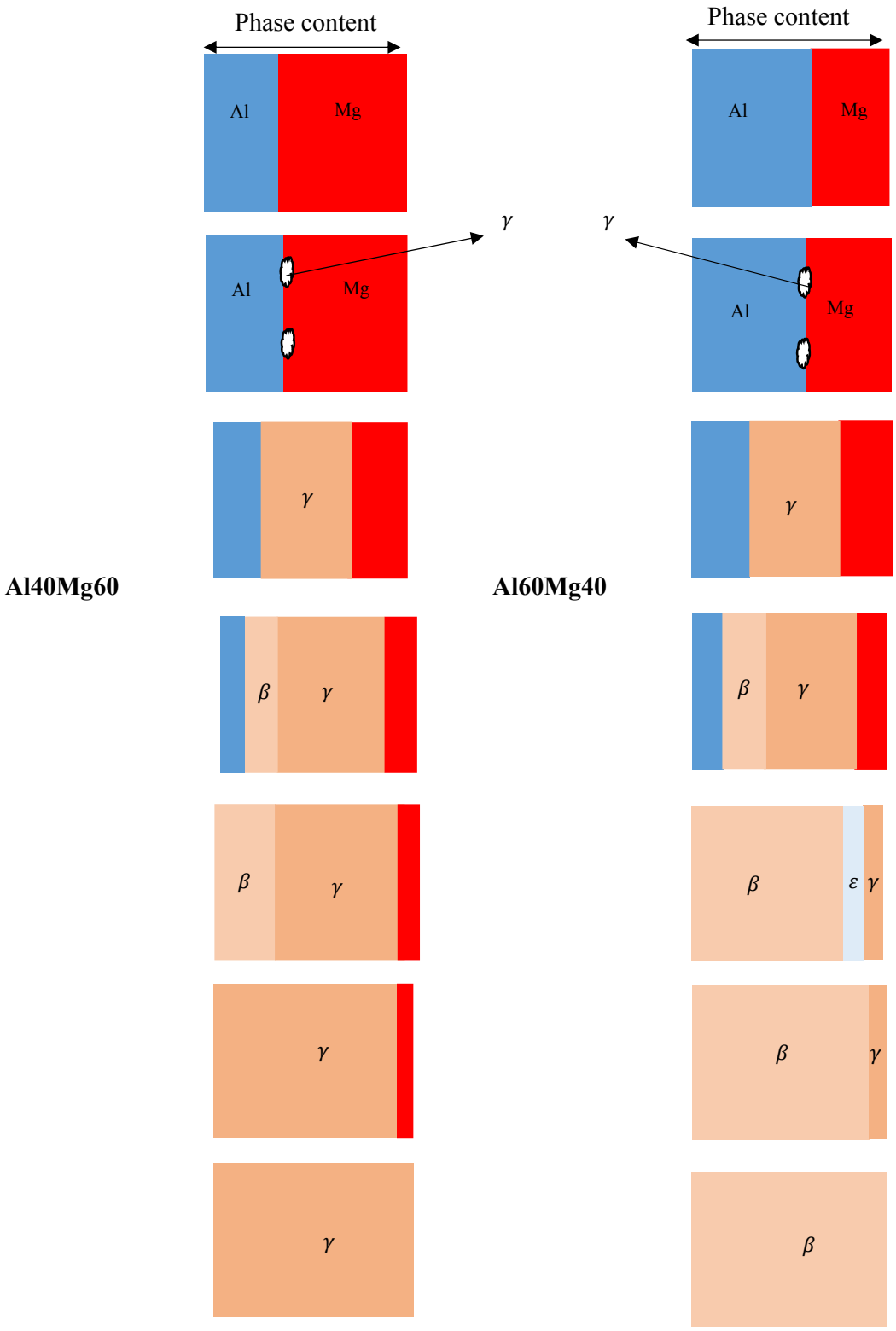

Figure 4.9-5. A schematic overview on phase growth for both, the Al40Mg60 and Al60Mg40 composition.

As can be seen in Tables 4.9-2 and 4.9-3 the β-phase is stable for the Al40Mg60 composition over the temperature range 250 °C to 350 °C and over the temperature range 200 °C to 350 °C for the composition Al60Mg40. The γ-phase is stable from room temperature to 400 °C for the Al40Mg60 composition and also up to 400 °C for the Al60Mg40 composition for an annealing times up to 2 h.

The phases present after annealing at 400 °C for 2 h is in fairly good agreement with the assessed phase diagram of Liang et al. [122] and Murray [1] showing that the phase diagram of Okamoto and Murray needed revisiting. For a complete overview please see Fig 4.9-5.

5 Texture development

5.1 Initial material

The initial material were rectangular bars, which had been extruded at room temperature. Optical micrographs taken from extruded bars with compositions of Al60Mg40 and Al40Mg60 are shown in Figure 5.1-1 to 5.1-2.The position on the samples from where the microstructure and hardness were investigated are indicated in Figure 5.1-3. The extruded bar cross-sections typically exhibited pancake-shaped Al-particles, that were surrounded by Mg (see Figure 5.1-1 to 5.1-2). These cross sections showed that the particles were elongated in the transverse direction (TD). These polycrystalline Al particles were observed in fine as well as coarse aggregates. The EBSD measurements (see Figure 5.1-6) revealed a large variation in the grain size. Going closer to the surface of the extruded bars (for more details see the Figures for both Al40Mg60 and Al60Mg40 compositions in the Appendix (see Figure 1 and 2 in Appendix), the pancake shape was reduced or even disappeared and there was a tendency for some Al particles to elongate in the normal direction (ND). Closer to the surface, both the Al as well as the Mg particles became smaller when viewed along the extrusion direction. It can be concluded, that along the whole extruded cross-section, a homogeneous distribution of Al and Mg-particles developed during the powder metallurgical processing and extrusion.

Z1: 1mm

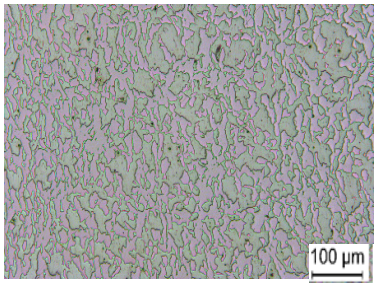

Z2: 3.15mm

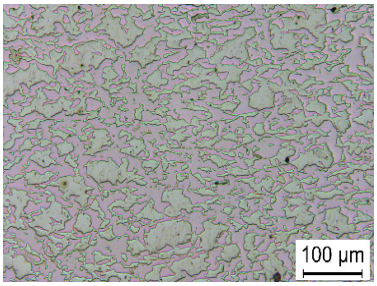

Z3: 5.3 mm

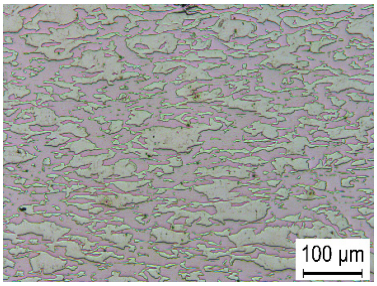

Z4: 7.45mm

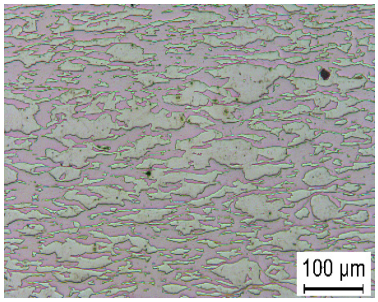

Z5: 9.6mm

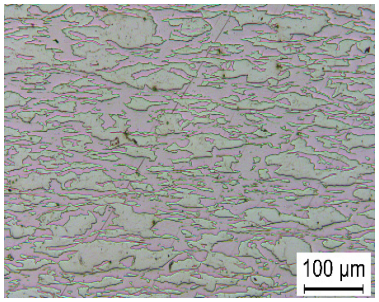

Figure 5.1-1: The microstructure in the TD direction of the Al60Mg40 specimen.

Z1:1mm

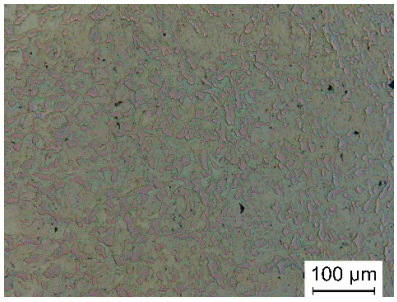

Z2: 3.15mm

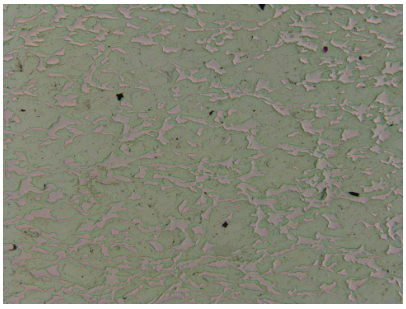

Z3: 5.3 mm

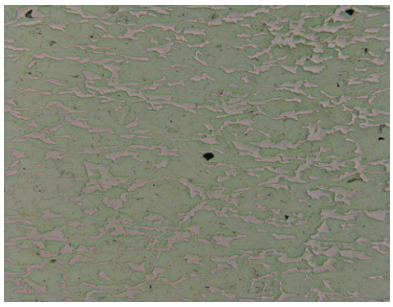

Z4: 7.45mm

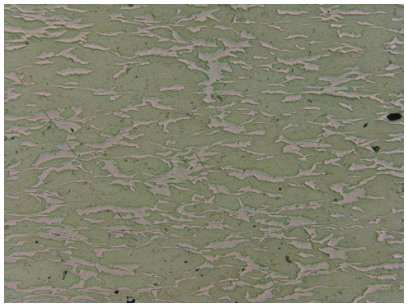

Z5: 9.6mm

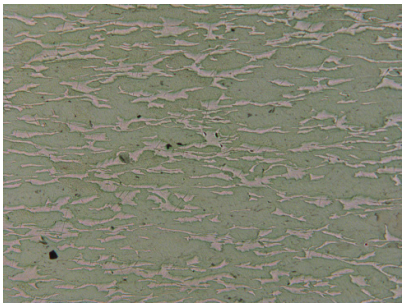

Figure 5.1-2:
The microstructure in the TD direction of the Al4Mg60 specimen.

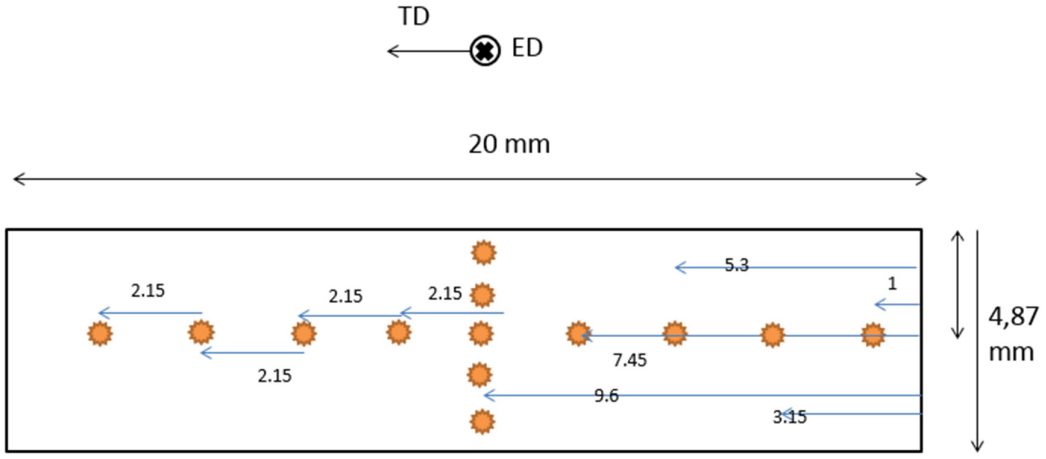

Figure 5.1-3: The positions on the extruded bars where the microstructure and hardness were investigated for both compositions Al60Mg40 and Al40Mg60.

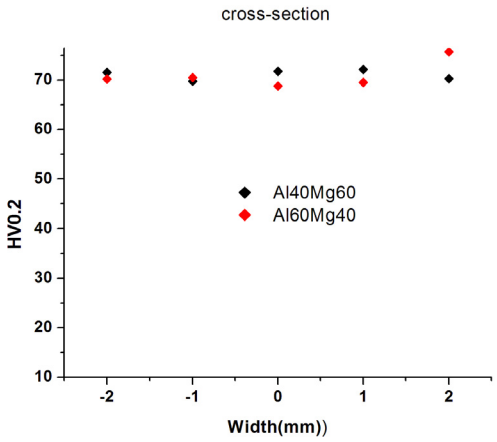

Figure 5.1-4: The hardness values over the cross-section of Al60Mg40 and Al40Mg60 from top to down.

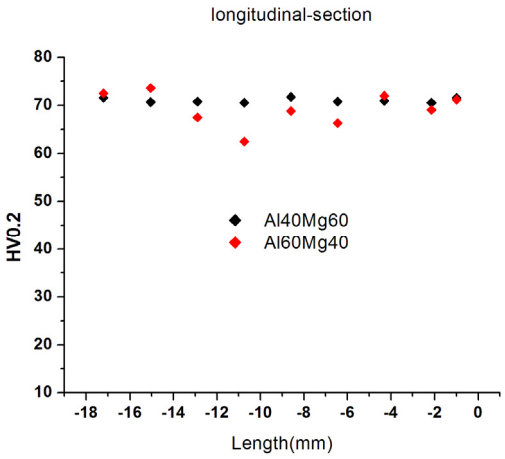

Figure 5.1-5: The hardness values along the longitudinal-section of Al60Mg40 and Al40Mg60 in the TD direction.

The microhardness measurements were carried out at the same positions as where the microstructure investigation and the results are shown in Figures 5.1-4 and 5.1-5. Generally, for both materials, the microhardness is in a band between HV 66 ± 2 and 72 ± 2 along the TD and between 69 ± 2 and 75 ± 2 along the ND over the cross section of both specimens.

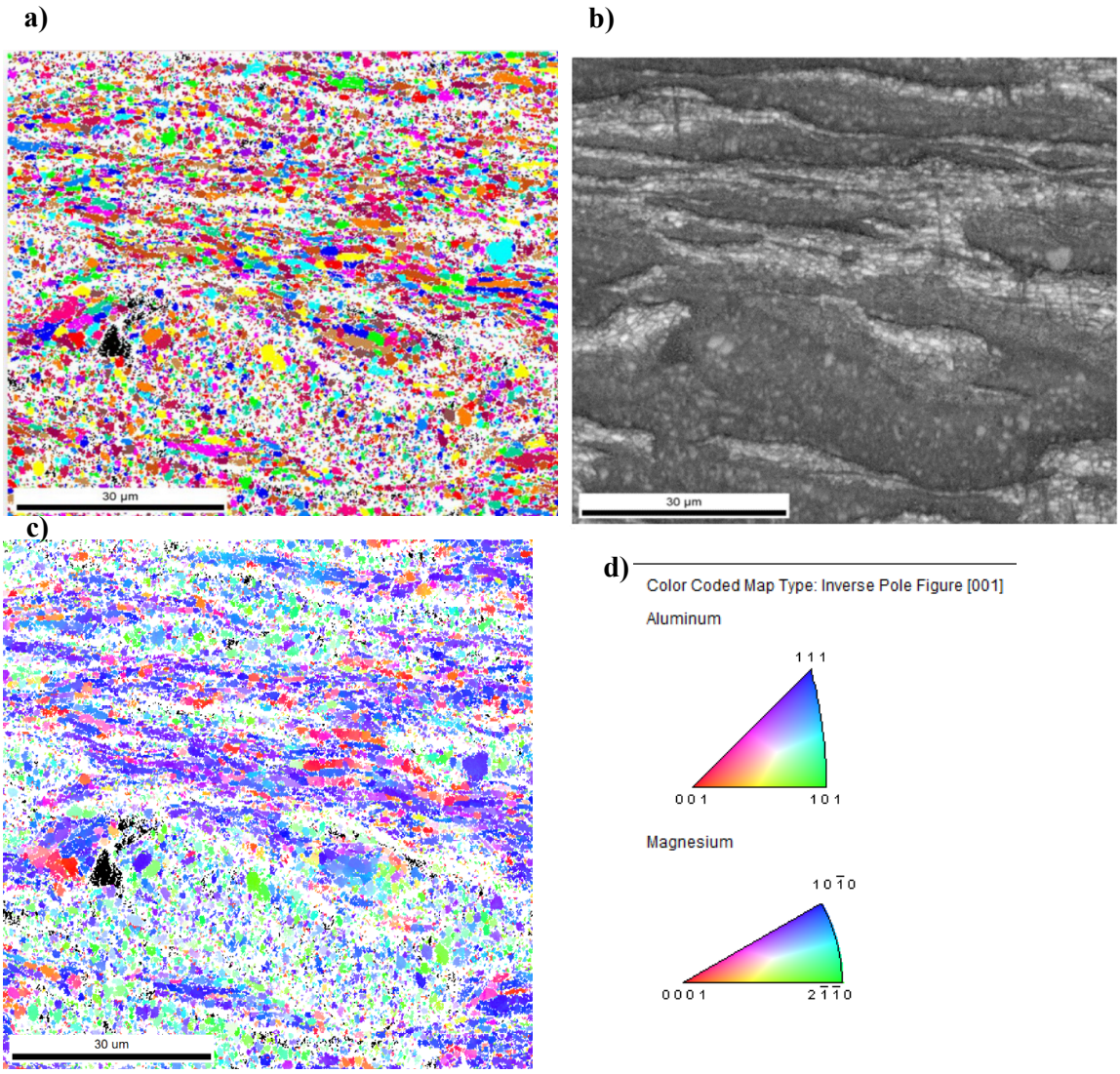

Figure 5.1-6: a) Unique color map, b) Image quality map and c) The inverse pole figure map d) color coded contour. All obtained by EBSD for the position Z5 of the extruded Al60Mg40 bar. In the image quality map the phase with a darker color is Mg and the brighter one is Al.

The large variation in the grain size was similar for both composition, Al60Mg40 and Al40Mg60. Due to the better quality of the sample with a higher Mg content, the EBSD result of Al60Mg40 specimen at the middle section is shown here.

5.2 Texture of the initial materials after extrusion

Due to the previous investigations and the microstructures obtained in different positions, it was interesting to investigate the texture gradient along the TD direction. Earlier

investigations indicated that five positions would be sufficient to cover the texture gradient over the area of interest. The positions at which measurements were made were Z1=1 mm, Z2 = 3.15 mm, Z3 = 5.3 mm, Z4 = 7.45 mm, and Z =9.6 mm below the surface.

5.2.1 Texture gradient of the Al-phase

Figure 5.2-1 shows pole figures for Aluminum, obtained by synchrotron measurements determined at the positions Z1 and Z5 of both the Al60Mg40 and the Al40Mg60 extruded bars in Figure 5.2-2. The symmetry in these pole figures is obvious. Later it will be shown that a similar symmetry does not exist in the corresponding Mg pole figures. This was also the case for the Al-phase of the Al40Mg60 specimen, but the texture sharpness was decreased. Table 5.2-1 presents a comparison between the texture sharpness for Al across the extruded bars.

		(111)	(200)	(220)	V_{max}/F_{max}
Al40Mg60	Z1	7.02	3.87	4.12	14.32/11.35
	Z2	10.12	3.18	3.26	12.19/11.18
	Z3	6.98	3.06	3.89	10.86/9.48
	Z4	9.52	3.68	4.65	14.43/12.36
	Z5	5.97	3.13	3.81	10.13/8.94
Al60Mg40	Z1	11.39	4.02	3.79	15.40/13.32
	Z2	13.34	3.76	4.04	16.77/15.08
	Z3	8.04	3.62	4.76	14.48/11.64
	Z4	6.73	3.56	4.72	13.04/10.58
	Z5	6.45	3.65	4.68	12.72/10.52

Table 5.2-1: A comparison between the texture sharpness of Al in the two extruded compositions, namely Al40Mg60 and Al60Mg40.

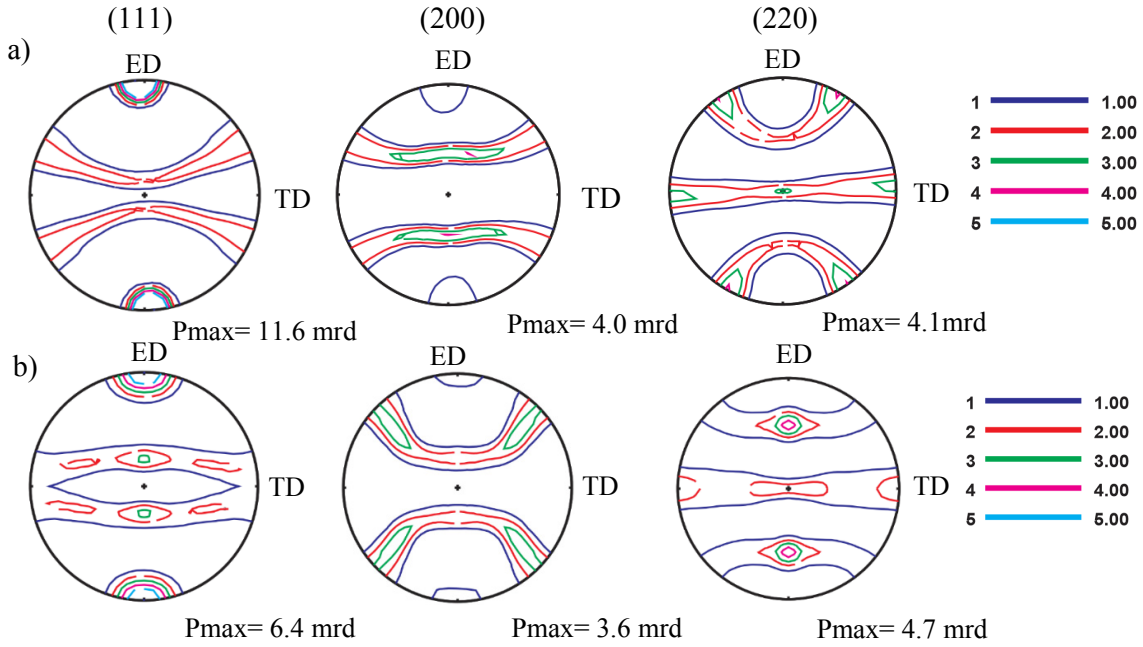

Figure 5.2-1. (111), (200) and (220) pole figures of Aluminum determined for the Al60Mg40 composition a) measured at the surface (position Z1) and b) measured in the middle section (position Z5) by synchrotron radiation.

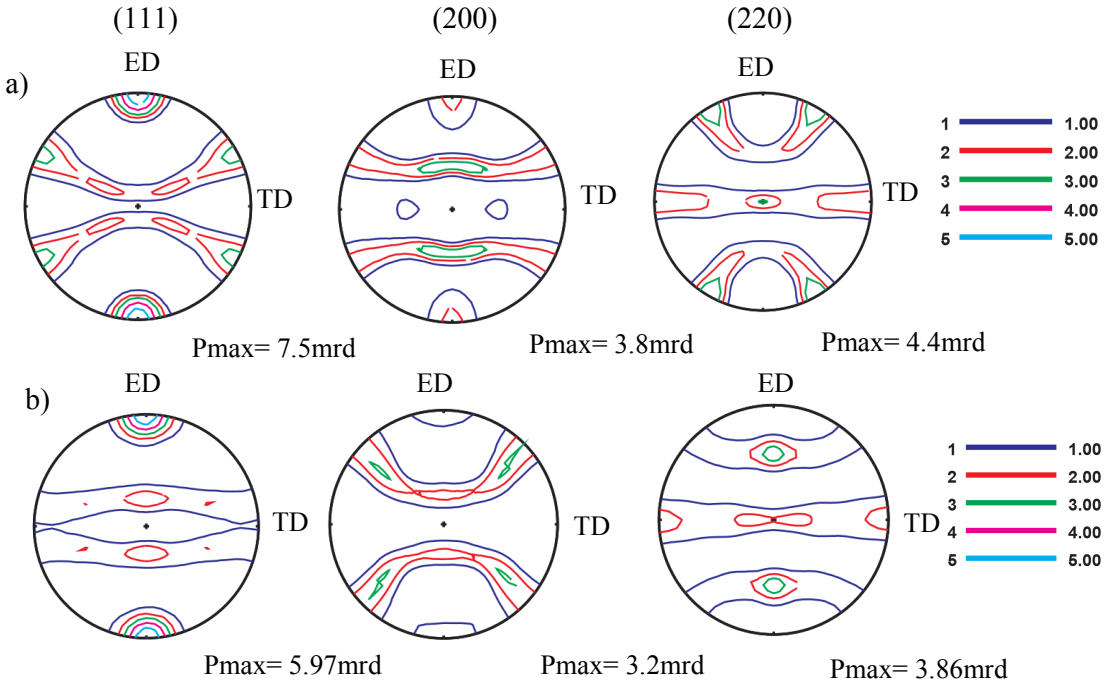

Figure 5.2-2 (111), (200) and (220) pole figures of Aluminum determined for the Al40Mg60 composition a) measured at the surface (position Z1) and b) measured at the middle section (position Z5) by synchrotron radiation.

The ODF sections reveal more information concerning the texture gradients within the extruded Al60Mg40 bar as shown in Figure 5.2-5. Between the central part of the rectangular extrudate (positions Z3, Z4 and Z5) and the surface there is a transition in the texture. Going towards the surface two main texture effects can be observed. Firstly, the texture sharpness increases from the center to the surface of the bar. This can be seen by means of the so called β-fiber (see Figure 5.2-3), which runs from the copper component {112} <111> ($\varphi_1 = 90°$, $\Phi = 35°$, $\varphi_2 = 45°$) to the brass component. Secondly, a rotation of the β-fiber can be seen in the central part of the ideal <111> fiber parallel to the ED (see Figure 5.2-3). A rotation can also be seen quite well in the α-fiber (see Figure 5.2-4). In the α-fiber the brass component {110} <112> shifts to the G/B component {110} <111>. The same reorientation is also observed for the S component {123} <634> ($\varphi_1 = 59°$, $\Phi = 34°$, $\varphi_2 = 63°$), which rotates towards the S* component.

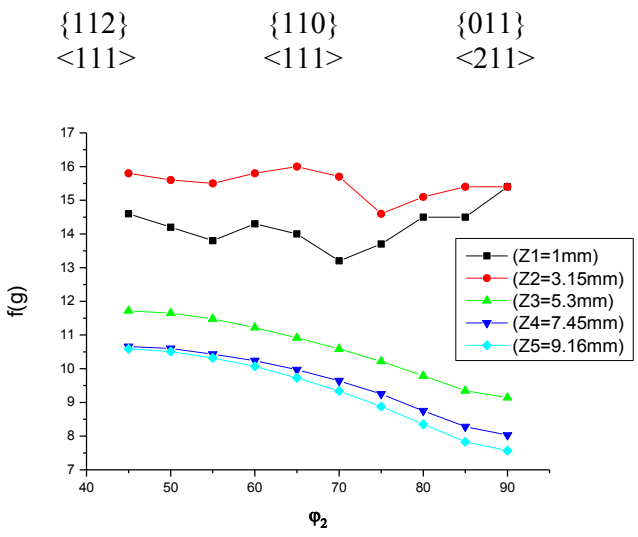

Figure 5.2-3: The β-fiber plot of positions Z1 to Z5.

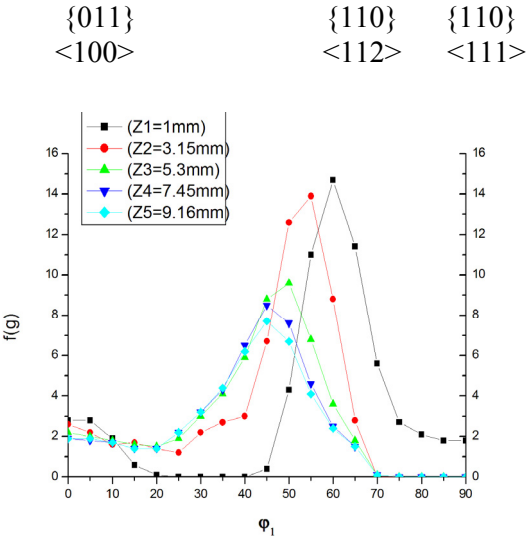

Figure 5.2-4: α-fiber plot of positions Z1 to Z5.

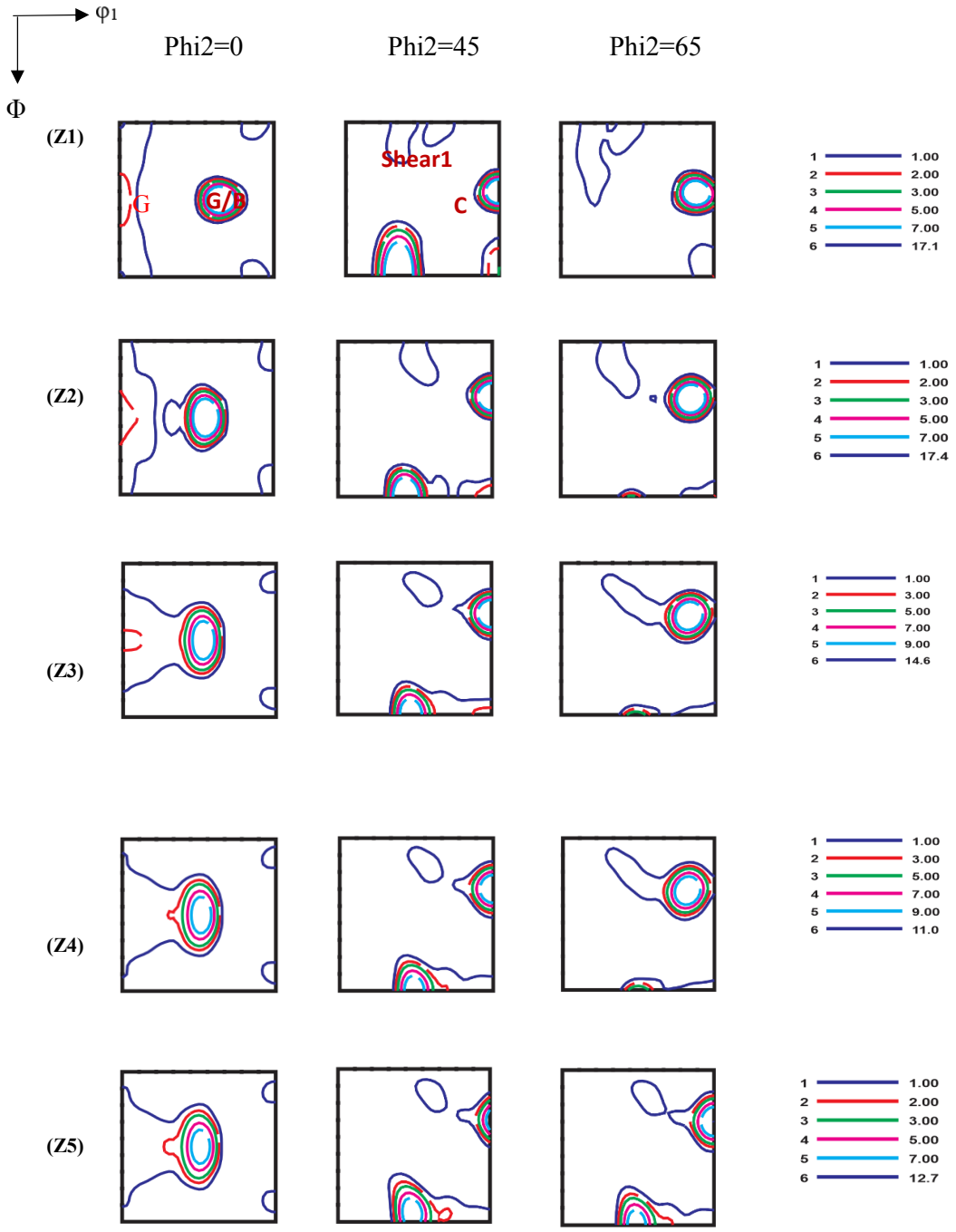

Figure 5.2-5: ODF sections at specific φ_2 sections for Al in the cold extruded Al60Mg40 rectangular bar. Z1) 1 mm below the surface, Z2) 3.15 mm below the surface, Z3) 5.3 mm below the surface, Z4) 7.45 mm below the surface and, Z5) 9.6 mm below the surface.

The Goss component is a minor texture component, which varies between 1.8 mrd up to 3.0 mrd. At the TD surface of the extruded bar a shear component, seen by splitting of the cube

component (φ_1 = 45°, Φ = 0°, φ_2 = 4 5°) indicates that there was friction at the surface during the extrusion process. This texture evolution is also characteristic for the Al40Mg60 extruded bar. However, due to the lower Al content (40 wt. %) the texture of Aluminum is weaker than in Al60Mg40. The difference in compositions on the texture has an effect on the sharpness of the texture.

5.3 Texture gradients of the Mg-phase

Compared to Al, the Mg texture gradient is stronger (see Figure 5.3-1 5.3-2), and is more dependent on sample position. On one hand the double peak of the split <0001> fiber exists along the whole gradient. On the other hand a continuous rotation of the two <0001> fibers towards the TD is visible. Moreover, the ideal component is stable in the main part of the sample (Z5 → Z3) and only diminishes near the surface of the extruded bar, while the partial <10$\bar{1}$0> fiber parallel to the ED gets stronger and is enhanced to a complete fiber. At the middle section the texture components are a split <0001> fiber parallel to the ND with a tilt of about ±10° in the ED. This behavior is typical for rare-earth containing magnesium alloys that have undergone plane strain deformation; it was observed for Mg-WE43 [134] and rare earth Mg-alloys [135]. In addition to the <0001>∥ND, the other components are the ideal {0001} <10$\bar{1}$0> and the partial <10$\bar{1}$0> fiber parallel to the ED with a scatter of nearly ±75° in the TD.

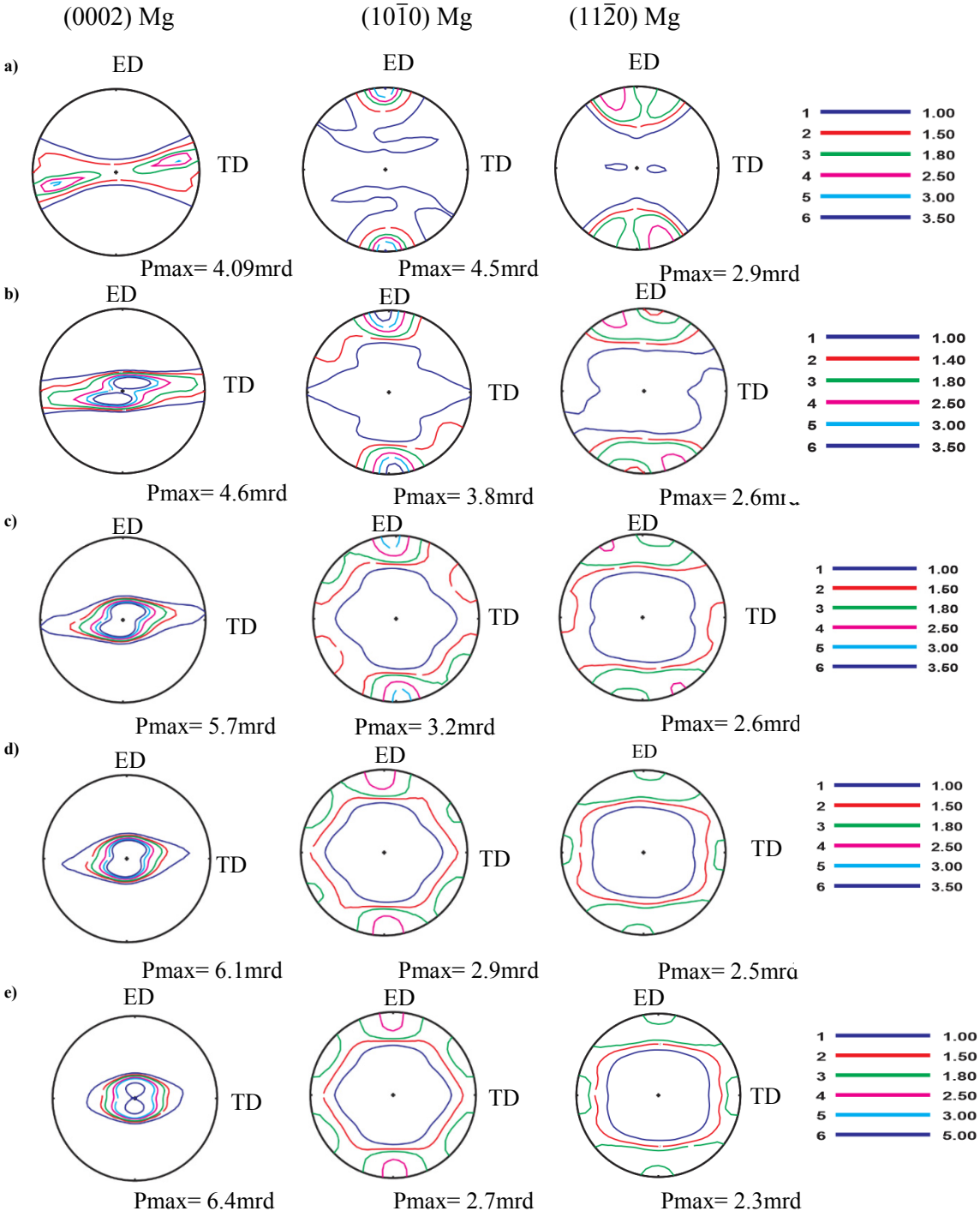

Figure 5.3-1: Texture gradients in Al60Mg40, presented by (0002), (10$\bar{1}$0) and (11$\bar{2}$0) Mg pole figures ; a) 1 mm , b) 3.15 mm , c) 5.3 mm d) 7.45 mm and e) 9.6 mm below the surface.

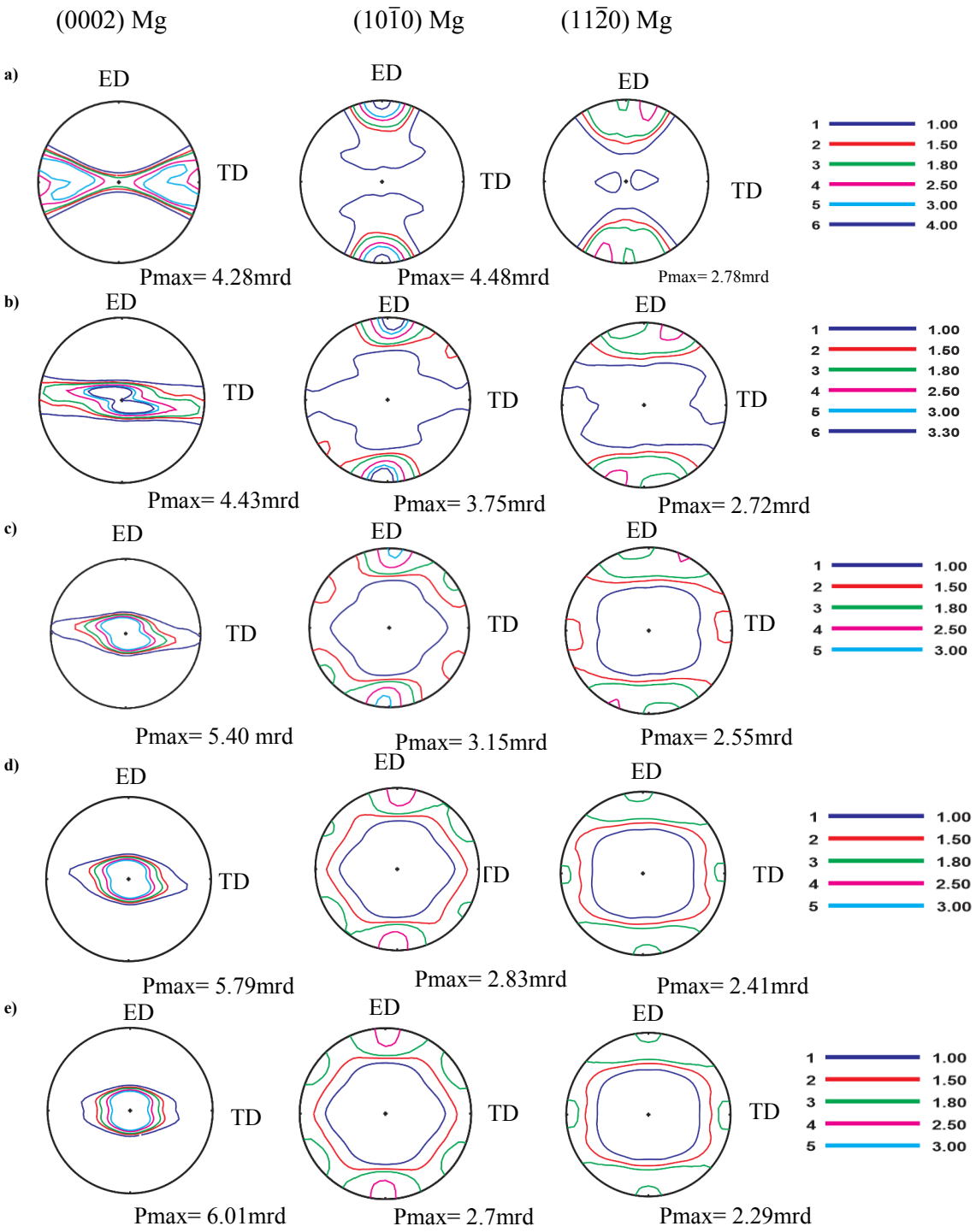

Figure 5.3-2: Texture gradients in Al40Mg60, presented by (0002), (10-10) and (11$\bar{2}$0) Mg pole figures ; a) 1 mm , b) 3.15 mm , c) 5.3 mm d) 7.45 mm and e) 9.6 mm below the surface.

5.4 Discussion of the texture gradient

The co-deformation of an Al60Mg40 composite during bar profile extrusion leads to a remarkable texture gradient in the transverse direction. This may result on one hand from the friction at the extrusion die and secondly from the co-deformation of cubic Al with hexagonal Mg. Al has excellent room temperature formability compared to the problematic room temperature formability of Mg. Room temperature extrusion in Al-Mg composites was only possible when using a sufficiently high Al content. The detailed information about the deformation mechanism in Mg and Al are provided in the section 2.5 and 2.9. At the surface, the Al matrix shows a strong <111> fiber and a very weak <100> fiber. This kind of texture was usually observed after wire drawing and rod extrusion as well as after uniaxial tensile loading [136]. In the middle section of the bar, one can observe a typical plane-strain deformation texture (see Figures 5.4-1, 5.4-2) that is similar to the sheet rolling texture of different Al alloys which have the copper type texture [38]. Three typical rolling texture components exist, namely copper, S and brass. The texture gradient in the Al matrix can be described by a rotation of the ß-fiber towards the <111> fiber parallel to the ED. This rotation can be clearly seen in the shift of the brass texture component (central area-Z5) towards the G/B texture component (TD surface) in the α-fiber (see Fig 5.2-4). Simultaneously, a weak <100> fiber parallel to the ED was present near the TD surface. These two types of texture in the bulk of an extrudate and near the surface were also described for an L-profile extrudate of an Al-Li alloy in [137]. The authors found that having a plane-strain kind of texture resulted in a 20 % increase in strength compared to a uniaxial kind of texture. This kind of texture development was mainly attributed to local strain variation during the extrusion process [138] and the related activation of slip systems as reported in [38]. One key point is the extrusion asymmetry ratio of width to thickness (W/T). In rectangular shaped extrusions, compression is much greater in the ND than in the TD.

Beside rotation of the texture components, which are weak in the central area and stronger closer to the surface, the texture sharpness also varies strongly from the central region to the surface. As an example, for the Al60Mg40 composition, the copper component increases from 10.4 mrd in the center to 14.8 mrd near the TD surface, while the brass component rises from 7.6 mrd to 15.4 mrd. Similar to an investigation of Zhong et al.[139], on a rolled Al7020 plate, the strongest texture is not directly at the surface but in a certain distance that is related to the sample cross-section.

The texture gradient (see Figures 5.3-1 and 5.3-2) is more pronounced in the Mg-phase than in the Al-phase. The Mg-texture in the central region of the extrudate shows a different type of texture development (see Fig. 5.3-1 and 5.3-2) compared to Al. The double pole in the (0002) pole figure, which can be described as two <0001> fibers ‖ND with a tilt of ±10° can be related to a remarkable contribution of <c+a> glide to deformation. This spreading texture which has various tilt angles was mostly observed in rare earth (RE) Mg alloys [137] and also in some non-RE Mg alloys [140] and provides an improvement in ductility and formability [140]. It is known that the CRSS ratio of basal to <c+a> glide is important for the splitting angle of the central pole [141]. It appears that the neighborhood of Al grains influences the CRSS of <c+a> glide in such a way that <c+a> glide is intensified resulting in this type of texture being developed. Other Mg grains, having non-favored orientations for <c+a> glide, develop the ideal {0001} <10$\bar{1}$0> texture component. Steiner et al. [142] report that prismatic glide in addition to basal glide was obtained during the modeling of plain strain compression. Depending on the ratio of active prismatic glide versus active basal glide, a third texture component that could sometimes be observed in Mg, is the partial <10$\bar{1}$0> fiber in the ED. This partial fiber in the ED or RD is a common texture component related to the balance between basal and prismatic glide when there is only a small contribution from prismatic glide. This kind of fibre forms under restricted degrees of freedom and results in a complete

orientation girdle around the fiber axis. For an ideal round extrusion this fiber is ideal and has an orientation girdle from +TD to -TD in the (0002) pole figure with a nearly constant intensity distribution along the girdle. In the present case this girdle is incomplete with a scatter around ND towards the +TD and -TD. The degree of scatter depends on the aspect ratio of the width to the thickness of the extruded bar or on the pass reduction parameters during rolling [143]. Thin rolled sheets with high width/thickness reduction show no scatter and no <10$\bar{1}$0> partial fiber [143]. The texture gradient indicates that the three Mg-texture components behave differently. The ideal texture component {0001} <10$\bar{1}$0> is present only in the central region of the extrudate, where the die angle has little or even no influence. The contribution of prismatic glide is higher in the central region than closer to the TD surface. Whereas the partial fiber gets stronger from the central region towards the TD surface and develops a complete <10$\bar{1}$0> fiber parallel to the ED (see Figure 5.3-1 and Figure 5.3-2) when basal glide in combination with prismatic glide was active. The evolution of the split texture component, which shows a rotation of the two poles toward +TD and -TD is remarkable. The rotation angle in the central bar region (positions Z5 to Z4) is moderate but very strong close to the TD surface (Z1). Similar to the texture gradient in the Al-phase, the β-fiber rotates to the <111> fiber, and arises due to local strain variations. Figure 5.4-1 shows the rotation of the Mg crystal from the surface to the middle section.

It can be concluded that rectangular extrusion is a deformation process, classed as being intermediate between round extrusion and rolling. Therefore, the texture gradients obtained by high-resolution synchrotron diffraction show more texture diversity than after round extrusion or rolling. The high deformation symmetry of round extrusion suppresses many texture details due to rotational pole figure symmetry. Rolling to a high reduction often only results in a strong preferred orientation of major texture components. In the Al-phase a texture gradient with a moderate sharpness in the central region and a much stronger texture close to the TD

surface of the extruded bar were detected. The typical β-fiber that was seen in the rolled Al in the center rotates to a <111> fiber parallel to the ED at the surface. For Mg the texture is much weaker than for Al but stronger at the center than close to the surface of the bar. For Mg a {0001} <10$\bar{1}$0> texture component is present in the central region which disappears at the TD surface. The weak partial <10$\bar{1}$0> fiber parallel to the ED in the central region develops a complete fiber on moving closer to the TD-surface. The typical double pole in the basal pole figure, resulting from <c+a> glide, rotates from the ND to the TD and is most probably related to the local strain field. For Mg, as a material with a c/a ratio close to the ideal c/a ratio of the hexagonal close-packed structure, the basal plane tends to orient parallel to the transport plane of the deformation process.

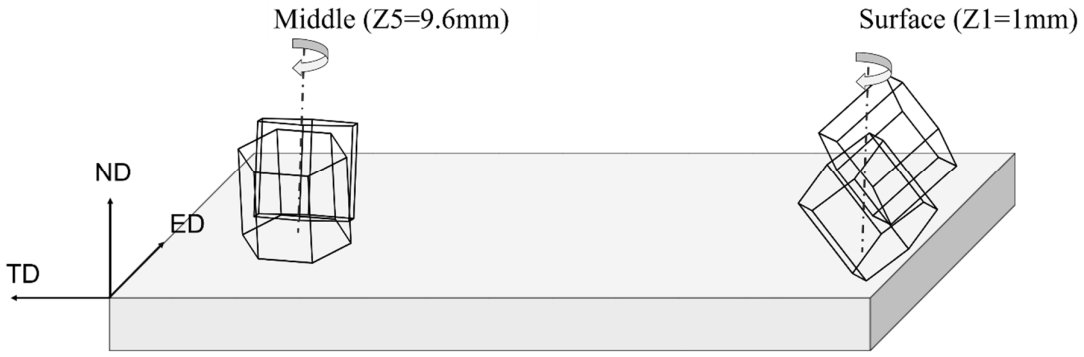

Figure 5.4-1 A Schematic representation of Mg crystals rotation from the surface to the middle section.

5.5 Texture development up to 200˚C

The room temperature texture was measured at all 5 positions (Z1 to Z5), as discussed earlier. Since at higher temperatures the central bar region is more interesting (and the sample has the biggest volume), only the texture in the central region (Z5) of the extruded bar will be discussed in the following. During heating to 200˚C a phase transformation has already started as can be concluded by the increase in the amount of the γ-phase as discussed in the section 4.3 (see Figures 5.5-1 and 5.5-2). The texture of the product phase does not significantly change the overall texture compared to room temperature. For both as-extruded

bar compositions, the magnesium phase has two texture components, the partial <0001> parallel to the ND and the partial <10-10> parallel to the ED components. These components were observed in the middle section of the extruded bar and remained after annealing at 200 °C for 12 h as can be seen in in Figure 5.5-3 and Figure 5.5-4. However, the partial $<10\bar{1}0>$ component parallel to the ED fiber decreases during annealing. In the as-received material two ideal $\{0001\}$ $<10\bar{1}0>$ texture components overlap. After annealing this component transforms to a $\{0001\}$ $<10\bar{2}0>$ texture component by a 30° rotation.

Moreover, a 30˚rotation of the maximum intensity of the (0002) pole figure from the ND direction and a decrease in the texture sharpness was observed. In a series of growth selection experiments for Zn single crystals, it was observed that recrystallized grains would grow preferentially 30˚rotated around <0001> with respect to the deformed matrix. This kind of texture thus indicates that recrystallized grains have grown. This weakening in texture and increase in the angular distance between the two maxima was observed also in the recrystallization of magnesium alloys [144] indicating that recrystallization is a result of nucleation of new grains in strain-free grains and their subsequent growth [145].

In the Al phase which has a FCC structure, recrystallization is generally different to hexagonal structured materials. The texture found after the heat treatment at 200 °C is very similar to that of the initial material. The maximum random density decreases from 5.9 mrd to 5.1 mrd and from 3.8 mrd to 3.3 mrd in the (111) and (220) pole figures respectively (see Figure 5.5-5 and Figure 5.5-6).

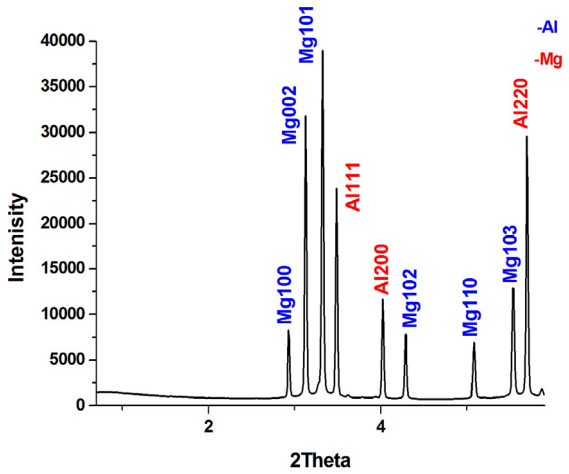

Figure 5.5-1: Diffraction pattern of the as-received cold extruded Al40Mg60 specimen.

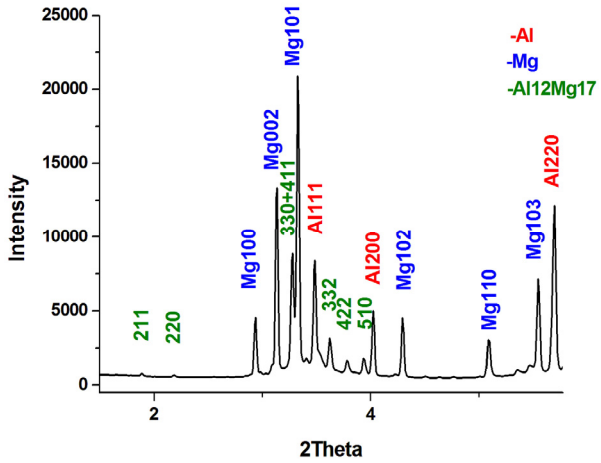

Figure 5.5-2: Diffraction pattern of the extruded Al40Mg60 specimen after annealing at 200 °C for 12 h.

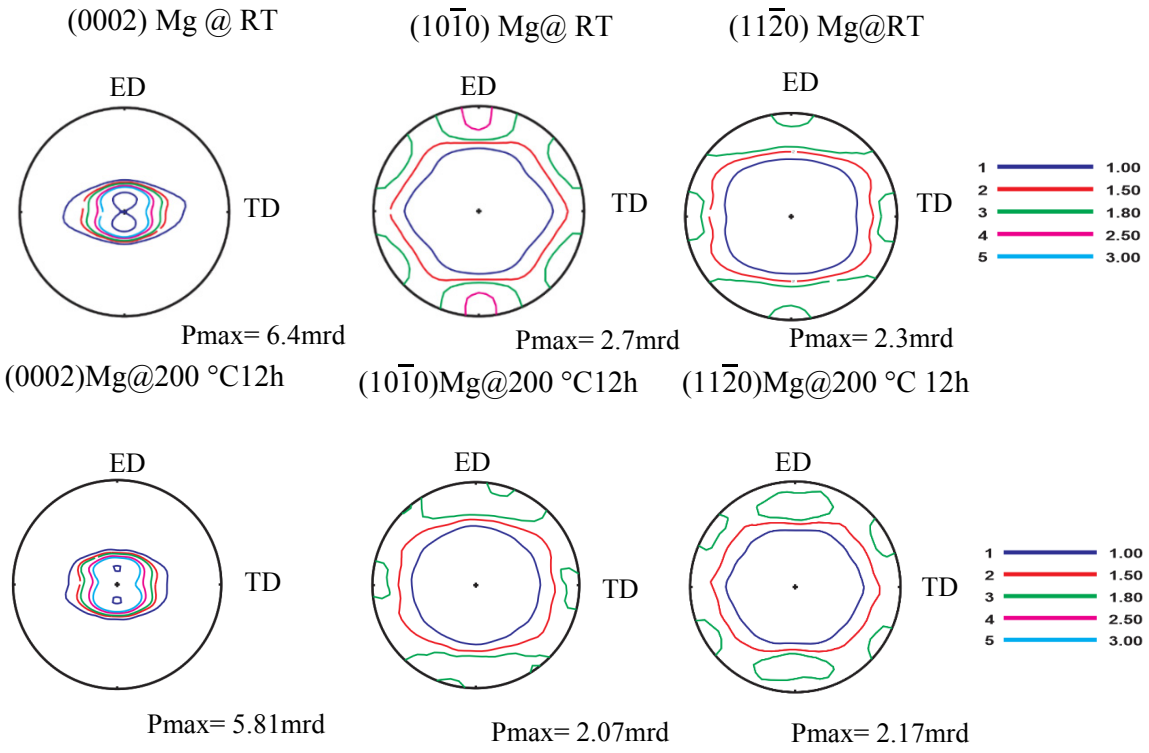

Figure 5.5-3: Texture development of the Mg phase in the Al60Mg40 composition before and after annealing at 200 ° C for 12 h.

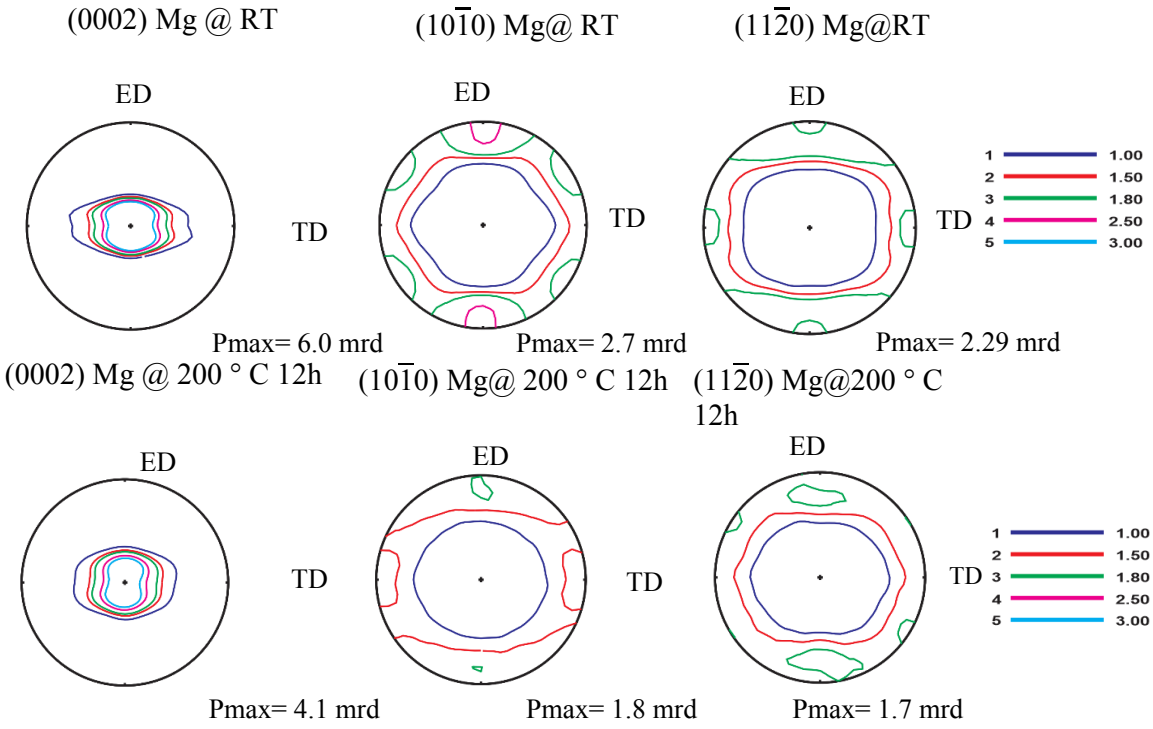

Figure 5.5-4: Texture development of the Mg phase in Al40Mg60 before and after annealing at 200 ° C for 12 h.

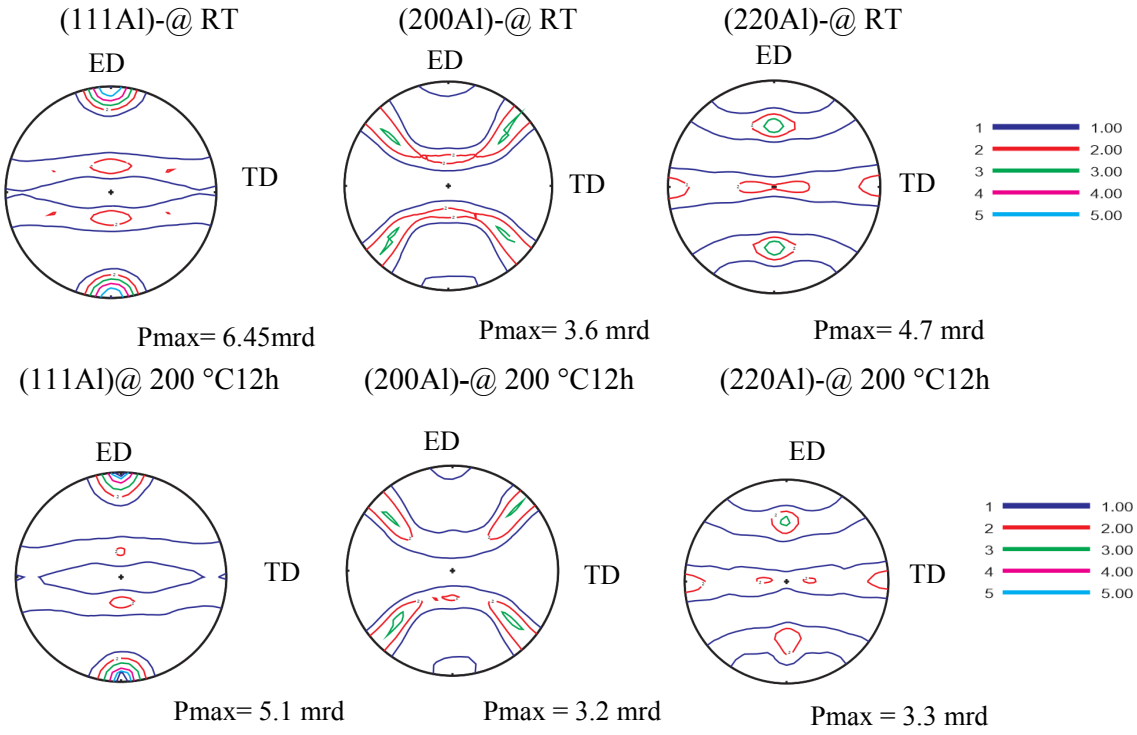

Figure 5.5-5: Texture development of the Al phase in the composition Al60Mg40 before and after annealing at 200 ° C for 12 h.

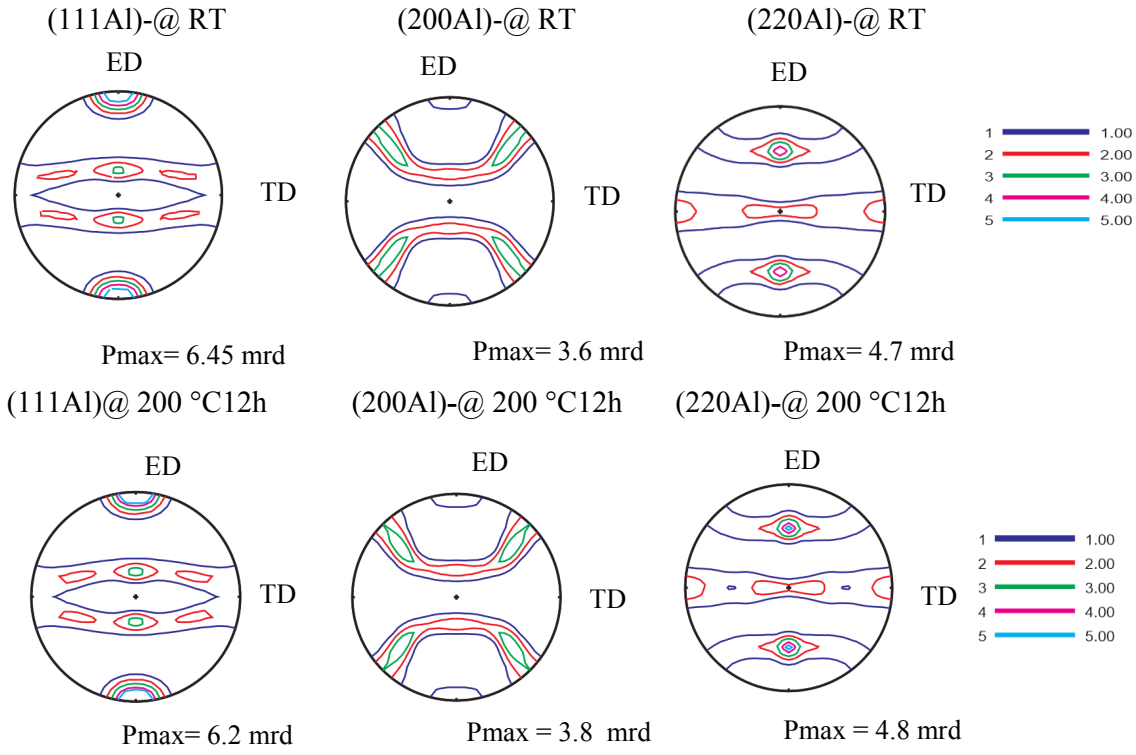

Figure 5.5-6: Texture development of the Al phase in the Al60Mg40 composition before and after annealing at 200 ° C for 12 h.

The φ_2 sections of the ODF (φ_1,ϕ, φ_2) revealed more information concerning the texture development (see Figure 5.5-7). Upon heating to 200 °C both compositions show an ED-rotated cube texture (100-fibre). However for the specimen in position Z5 this is dominated by the Goss orientation. The {001}<100> cube texture is a well-known sign indicating recrystallization in materials with medium to high stacking fault energies [110]. It is the main recrystallization texture component observed in most rolled aluminum sheets. The most important information about the recrystallization texture of Al can be found in the φ_2=0 section.

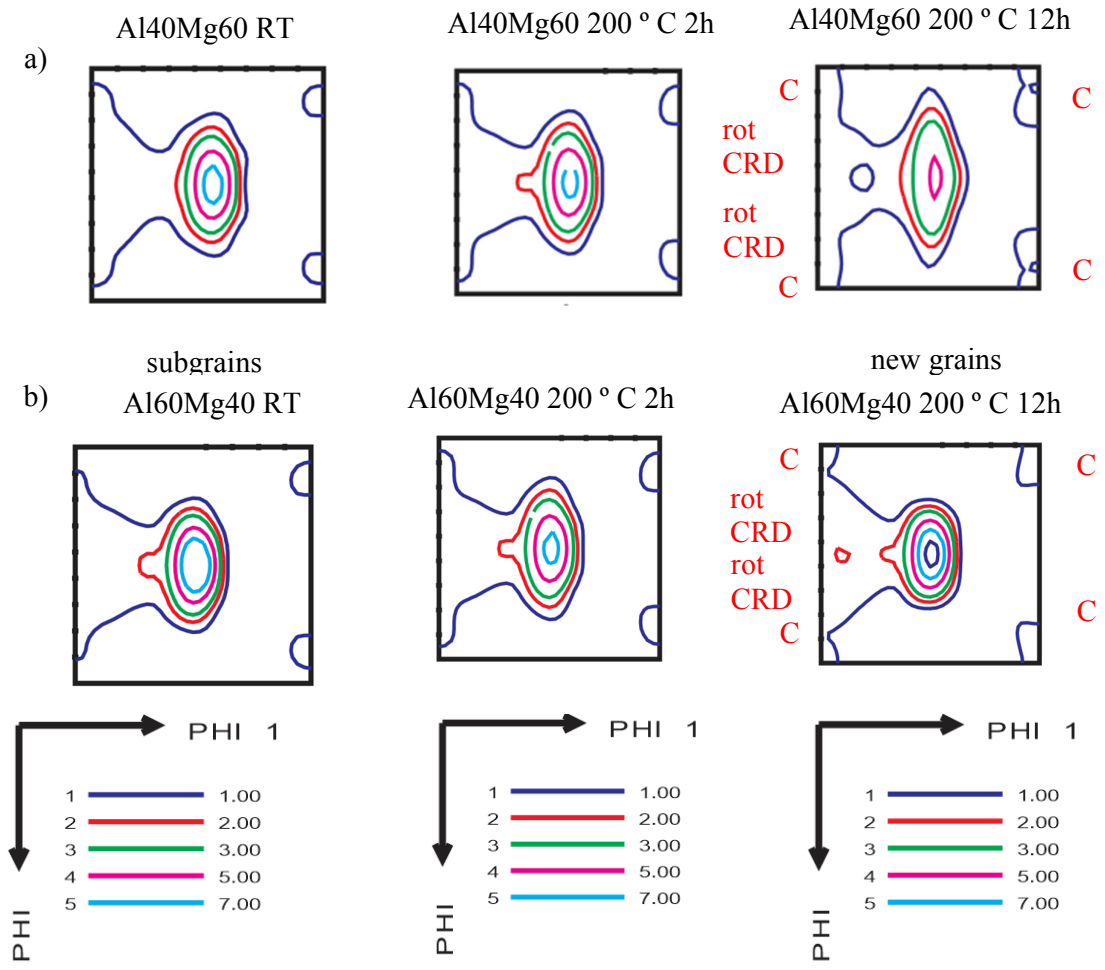

Figure 5.5-7: ODF sections of the Al phase for both bar compositions for φ_2= 0 at room temperature and after annealing at 200 °C for 2 and 12 h a) for the composition Al40Mg60 and b) Al60Mg40.

In the φ_2=0 section of the as-deformed composition (see Figure 5.5-7) one can see subgrains in the as-deformed state and that new grains are formed via annealing. Ridha [146] and later Dons [147] suggested that recrystallization nucleation is initiated within the bands that already existed in the as-deformed microstructure. In the neighborhood of these bands, there are components with all kinds of orientations the majority belonging to the β-fibre [148]. In some publications the S {123} <634> component, which was observed in the as-received material, was thought to be responsible for the cube {001}<100> texture found in FCC metals after recrystallization and formation of nucleation in band-like structures due to a 40˚<111> rotation [149]. The Cu component is also linked to the cube component. Since the driving force for recrystallization is higher in grains with the Cu orientation, the Cu component in the deformed texture is more likely to be responsible for the recrystallization texture than the S component [150].

5.6 Annealing at 400° C for 12 h

5.6.1 Microstructure of the Al40Mg60 composition after annealing at 400 °C for 12h

Both the Al40Mg60 and Al60Mg60 compositions are single phase after annealing at 400 °C for 12 h. Therefore the EBSD investigations were easier after annealing at 400 °C for 12 h. However, due to the complex crystal structure of the β-phase that was present after annealing at 400 °C for 12 h, the EBSD technique had difficulty in indexing the Kikuchi patterns. Therefore, the results of the EBSD measurements for the Al60Mg40 composition after annealing at 400 °C for 12h are not presented. An EBSD investigation of the middle section of the Al40Mg60 composition showed that annealing resulted in preferred grain growth.

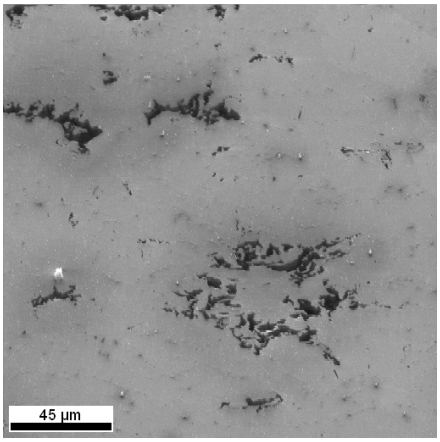

Figure 5.6-1: SEM micrograph of the Al40Mg60 sample after annealing at 400 °C for 12 h. This thermal treatment resulted in pores within the sample

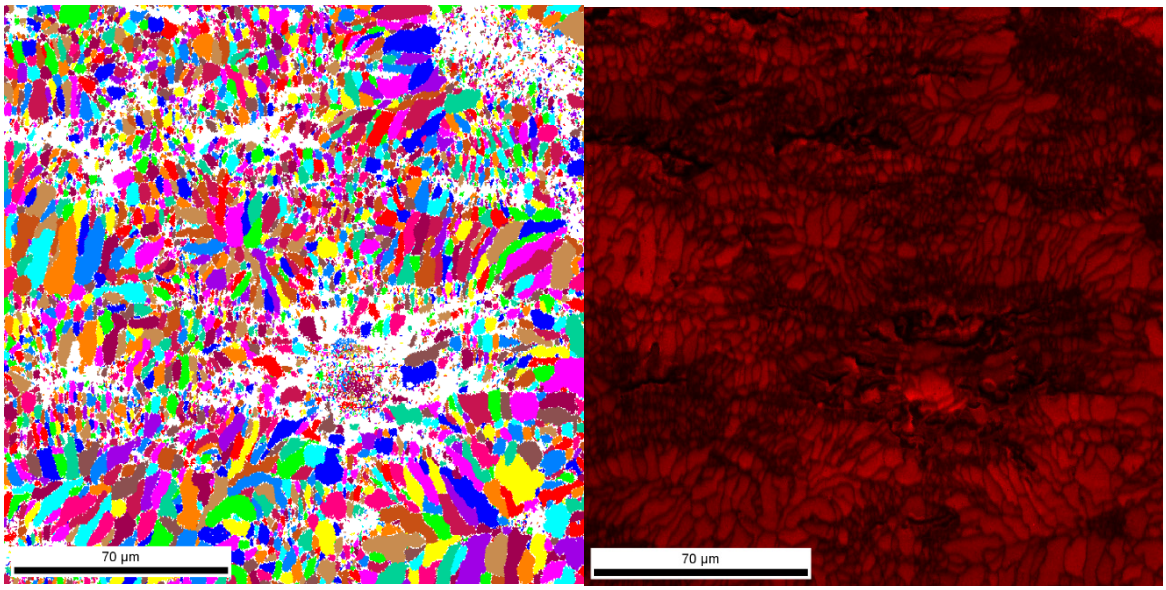

Figure 5.6-2: The inverse pole figure map and image quality map as obtained by EBSD taken from position Z5 of the Al40Mg60 extruded bar after annealing at 400 °C for 12 h. Preferred grain growth can be seen in the microstructure.

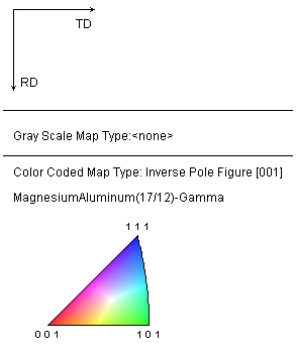

5.6.2 Texture development in Al40Mg60 after annealing at 400 °C for 12 h

As discussed in section 4.8 only the γ-phase remains in the Al40Mg60 composition after annealing for 12 hours at 400 °C. As discussed in section 3.12, in order to calculate the ODF a slit system was utilized and the resulting diffraction pattern obtained using this slit system technique is shown in Figure 5.6-3 and Figure 5.6-4. Generally, during a phase transformation a specific orientation relationship may exist between the disappearing (parent) and newly formed (daughter) phases (see Figure 5.6-5). When this preferred orientation relationship is known, the orientation of the parent or daughter phase may be calculated via the orientation distribution function (ODF) [58].

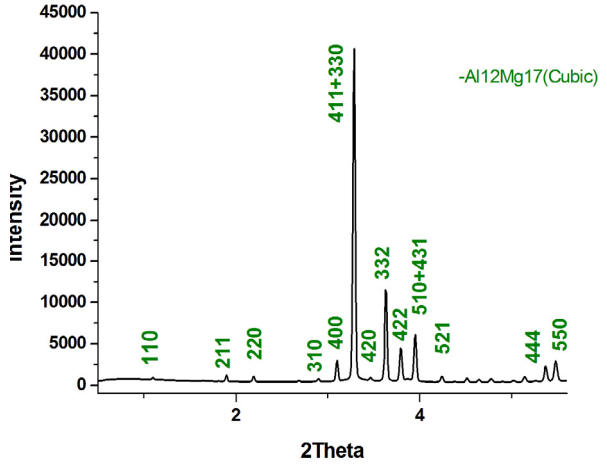

Figure 5.6-3: The diffraction pattern obtained for the Al40Mg60 composition annealed at 400 °C for 12h without using a slit system.

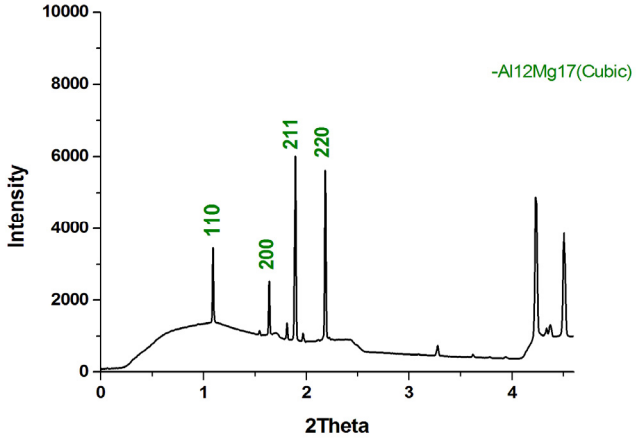

Figure 5.6-4: The resulting diffraction pattern for the Al40Mg60 composition after annealing at 400 °C for 12 h obtained using the slit system.

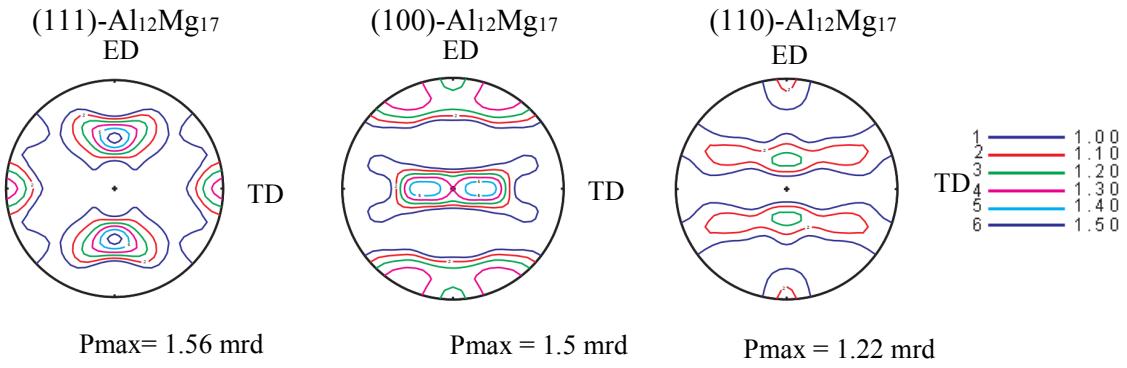

Figure 5.6-5: The calculated (111), (100) and (110) pole figures for the Al40Mg60 composition after annealing at 400 °C for 12 h.

A qualitative description of the orientation changes during the phase transformation by comparing that takes place while annealing at 400 °C with reveals that a Pitsch-Schrader relationship develops between the Mg phase of the as received material and the γ-phase of the annealed material. As can be seen in Figure 5.6-6 when one compares the (110) pole figure of the γ-phase and the (110) pole figure of Mg a Pitsch-Schrader orientation relationship can be identified. It should be noted that no orientation relationship between the β-phase and Al and Mg was found in this investigation. In the section 5.7, this point will be discussed comprehensively.

$(1\bar{1}0)\ Al_{12}Mg_{17} \parallel (1\bar{1}00)\ Mg$

$[100]\ Al_{12}Mg_{17} \parallel [2\bar{1}\bar{1}0]\ Mg$

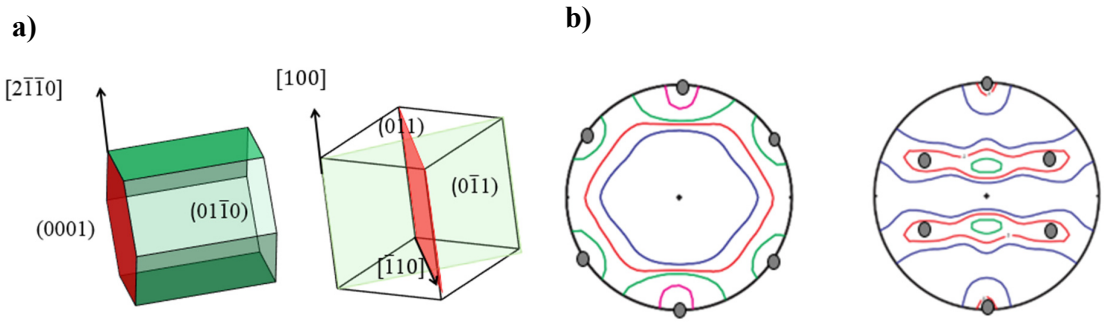

Figure 5.6-6: a) Schematic presentation of the Pitsch-Schrader orientation relation between the Mg and the γ-phase. b) Comparison between the calculated pole figures for the Mg- and γ-phases with. The grey points indicate the maximum intensity for the case of a single crystal.

5.7 Relationship between phase formation and texture

An orientation relationship is the crystallographic relation between specific directions and planes of two crystals. As discussed earlier (section 2.14) during some phase transformations certain specific orientation relationships develop between the parent and the product phases. These orientation relationships can associated with a minimization of the interfacial energy that allows the best fit at the interface between the two crystals. From the phase analysis in this study known that the γ- phase forms first via an interface reaction mechanism, whereas the β-phase formation is hindered by a nucleation barrier. The β-phase interface energy is very high and therefore no orientation relationship should occur between the parent and the daughter phase in case of the β-phase.

The result of lattice parameter determination by Rietveld refinement results in 1.054226 nm for the γ- $Al_{12}Mg_{17}$ -phase after annealing at 400 ° C for 12 h and cooling to room temperature which is in very good agreement with the literature [151] lattice parameter of 1.05492 nm. For Mg lattice parameter of a = 0.320936 nm and c = 0.521123 nm have been determined in the same way.

The unit cell of the γ-phase can be considered as a BCC crystal structure made up from 27 subcells repeated 3*3*3 [75, 76]. The d-value of the matching planes of phases arranged in a certain orientation relationship has an influence on the mismatch between these phases [75, 76].

Zhang and Kelly stated in their review article [151] that one criterion for good interface matching based on the edge-to-edge model is d-value mismatching < 6 % between the two phases, where for the Pitsch-Schrader OR with (101)BCC||(0001)HCP matching planes a rather low d-value mismatch of ~4.6 % was observed. As second criterion, the atom row

mismatch should be below 15 %. Using the measured lattice parameter for the Mg and γ-$Al_{12}Mg_{17}$ the mismatch along the directions [010] BCC || $[2\bar{1}\bar{1}0]$HCP and $[\bar{1}\bar{1}0]$BCC|| $[1\bar{1}00]$ HCP amounts to 9.5 % and 11.8 %, which explains the formation of this orientation relationship. However, the question arises, why multiple other orientation relationships were found between the Mg and γ- $Al_{12}Mg_{17}$ phases in other work. The (033), (411) and $(8\bar{7}\bar{7})$ are the closed-packed or near closed-packed planes of the γ-phase-Al12Mg17. It is suggested that there is a pseudo-twinning between the planes $(\bar{8}\bar{7}\bar{7})$, $(\bar{4}11)$, (033), (411) and $(8\bar{7}\bar{7})$ [152]. Liu et al. [152] found that the pseudo-twinning relationship between the 6 ORs, i.e. the Pitsch-Schrader, Crawley, Burgers, Potter, Porter and Gjöness-Östmoe OR of the γ-$Al_{12}Mg_{17}$ phase observed in their calculation reflects the pseudo-twinning relationship between the close or near-close packing planes planes $(\bar{8}\bar{7}\bar{7})$, $(\bar{4}11)$, (033), (411) and $(8\bar{7}\bar{7})$ in the γ-Mg12 Al17-phase with a tilting angle of (110) ||70.5°.

The experimental observation of the Pitsch-Schrader OR in the present work and the theoretical calculation indicates that this orientation relationship is the starting point for the five other ORs between Mg and the γ-$Al_{12}Mg_{17}$ phase (see Figure5.7-1).

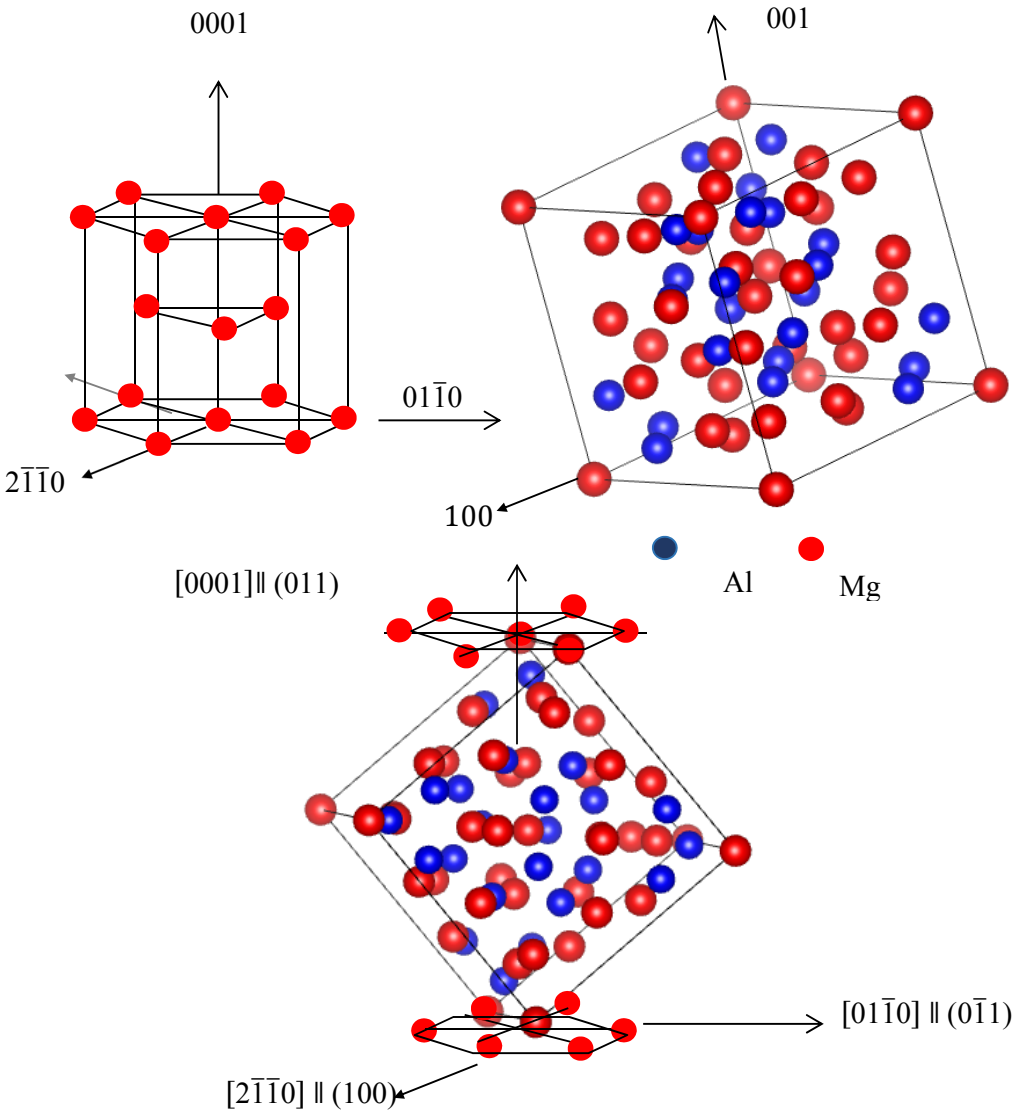

Figure 5.7-1 Schematic illustration of the crystal structures a) h.c.p Mg b) γ-$Al_{12}Mg_{17}$ c) description of Pitsch-Schrader orientation relationship .

6 Conclusion and recommendations

In this study the phase formation and growth of intermetallic phases in the Al-Mg system was investigated using Al-Mg metal matrix composites produced via powder metallurgy and cold extrusion. The main conclusions are:

- The cold extrusion process resulted in a texture gradient over the cross-section of the extruded profile. In the central region of the extruded bars the aluminum phase shows a typical texture component resulting from plane-strain deformation. Near to the outer surface of the bars a uniaxial deformation texture was observed. In the central region of the bars, the (0002) Mg pole figure shows a split along the extrusion direction (± ED); this has also been observed in rare-earth containing magnesium alloys. These two poles twist towards the transverse direction on moving towards the surface of the extruded bar, one pole moving towards +TD and the other one towards −TD. The angle of twist increases as the outer surface is approached.
- By annealing at 200 ℃ a recrystallization texture was observed in the Al phase as a cube texture component was formed. Additionally, a 30 º rotation of newly formed Mg crystals in the Mg-phase was observed. Like the cube texture component, which is the most prominent recrystallization texture in Al, a 30 º rotation is also sign of recrystallization in pure Mg.
- The γ-$Al_{12}Mg_{17}$-phase is the first phase to form during annealing in both the Al60Mg40 and Al40Mg60 compositions.
- A continuous linear growth of the γ-phase was observed during annealing, which indicates an interface reaction controlled growth mechanism. The β-Al_3Mg_2-phase is kinetically favorable to form but is hindered by a nucleation barrier, so that it was not formed at the beginning of annealing.
- The γ-$Al_{12}Mg_{17}$-phase shows an orientation relationship with the parent Mg phase.
- On annealing up to 250 ℃, no intermetallic phases other than the γ and β-phases were observed.

- On annealing at 400 ℃ for 2 h, both compositions reached their thermodynamic equilibrium. The Al40Mg60 composition consisted of the Mg and γ-phases and the Al60Mg40 composition had the γ- and β- phases.

Recommendations

- A mathematical model can be developed to describe phase development in the binary Al-Mg system from the qualitative and quantitative phase analysis results of the ex-situ and in-situ experiments performed at different temperatures for different annealing times.
- As described earlier, after annealing, the Mg phase shows a texture which has previously been seen in Mg rare earth alloys. It is known that the CRSS ratio of basal to <c + a> glide plays an important role for the formation of this texture. An investigation of the possible reasons for the formation of this kind of texture in the Al-Mg composites could be made using TEM. Such an investigation may increase the understanding concerning the formation of textures and could answer many related open questions about the formation of rare earth texture components.
- It would be useful to perform texture gradient simulations through the cross-section of the extruded bars using a self-consistent model or finite element model in order to better understand the relationship between the extrusion parameters and the texture gradient.
- There are many open questions based on the orientation relationship between the γ-phase and the Mg-phase and also between the β and Al with the parent Mg phase. Modelling and simulation of the evolution of texture during annealing would result in more detailed information about the orientation changes between the parent phase and transformed textures.

References

[1] J.L. Murray, The Al-Mg (Aluminum-Magnesium) System, Bulletin of Alloy Phase Diagrams 3(1) (1982) p. 60-75.
[2] S. Samson, E.K. Gordon, *The crystal structure of ε-$Mg_{23}Al_{30}$*, Acta Crystallographica. B24 (1968) p.1004-1013. https://doi.org/10.1107/S0567740868003638
[3] H.L. Su, P. Donnadieu, C. Baetzner, H. J. Seifert, H. L.Lukas, G. Effenberg, F. Aldinger, *Experimental investigation of the Mg-Al phase diagrm from 47 to 63 at% Al*, Journal of Alloys and Compounds 247 (1997) p. 57-65.
https://doi.org/10.1016/S0925-8388(96)02595-9
[4] Okamoto, *Al-Mg (Aluminum-Magnesium)*, Journal of Phase Equilibria and Diffusion 19(6) (1998) p.1.
[5] W.Z. Tomasz Czeppe, and Elzbieta Bielańska, *Study of the Thermal Stability of Phases in the Mg-Al System*, Journal of Phase Equilibria and Diffusion 24(3) (2001) p. 249-254.
https://doi.org/10.1361/105497103770330550
[6] D. Akhtar, R. Gopalan, T.P. Rajasekharan, *On a new metastable phase in the Al-Mg system*, Zeitschrift für Metallkunde 78 (1987) p. 201-203.
https://doi.org/10.1361/105497103770330550
[7] G.B. Walker, M. Marezio, *Lattice parameters and zone overlap in solid solutions of lead in magnesium*, Acta Metallurgica 7(12) (1959) p. 769-773.
https://doi.org/10.1016/0001-6160(59)90090-2
[8] Y. Li, P. Liu, J. Wang, H. Ma, *XRD and SEM analysis near the diffusion bonding interface of Mg/Al dissimilar materials*, Vacuum 82(1) (2007) p. 15-19.
DOI: 10.1016/j.vacuum.2007.01.073
[9] H. Chang, M.Y. Zheng, W.M. Gan, K. Wu, E. Maawad, H.G. Brokmeier, *Texture evolution of the Mg/Al laminated composite fabricated by the accumulative roll bonding*, Scripta Materialia 61(7) (2009) p. 717-720.
https://doi.org/10.1016/j.scriptamat.2009.06.014
[10] P. Donnadieu, M. Harmelin, H.-L. Su, H.-J. Seifert, G. Effenberg, F. Aldinger, *A quasicrystal with inflation symmetry and no forbidden symmetry axes in a rapidly solidified Mg-Al alloy*, Zeitschrift für Metallkunde 88(1) (1997) p. 33-37.
[11] S. Scudino, M. Sakaliyska, K.B. Surreddi, J. Eckert, *Solid-state processing of Al-Mg alloys*, The 13th International Conference on Rapidly Quenched and Metastable Materials, IOP Publishing Ltd, Dresden, Germany, 2009, p. 012019.
doi:10.1088/1742-6596/144/1/012019
[12] E. Hajjari, M. Divandari, S.H. Razavi, T. Hommab, S. Kamado, *Intermetallic compounds and antiphase domains in Al/Mg compound casting,* Intermetallics 32 (2011) p. 182-186.
https://doi.org/10.1016/j.intermet.2011.12.001
[13] D. Dietrich, D. Nickel, M. Krause, T. Lampke, M.P. Coleman, V. Randle, *Formation of intermetallic phases in diffusion-welded joints of aluminium and magnesium alloys*, Journal of Materials Science 46(2) (2010) p. 357-364.
DOI 10.1007/s10853-010-4841-5
[14] Ming-Che Chen, Che.Wei Kuo, Chia-Ming Chang, Chih-Chun Hsieh, Yin-Yu Chang and Weite Wu, *Diffusion and Formation of Intermetallic Compounds during Accumulative Roll-Bonding of Al/Mg Alloys*, Materials Transactions 48(10) (2007) p. 2595-2598.
DOI: 10.2320/matertrans.MD200718
[15] E. Schürmann, H.J. Voss, *Untersuchung der Schmelzgleichgewichte von Magnesium-Lithium-Aluminum-Legierungen*, Gießereiforschung 33 (1981) p. 43-46.
[16] N. Saunders, *A review and thermodynamic assessment of the Al-Mg and Mg-Li systems*, Calphad 14(1) (1990) p. 61-70.
https://doi.org/10.1016/0364-5916(90)90040-7

[17] Y. Zuo, Y.A. Chang, *Thermodynamic calculation of the Al-Mg Phase diagram*, Calphad 17(2) (1993) p. 161-174. https://doi.org/10.1016/0364-5916(93)90017-6
[18] P. Chartrand, A.D. Pelton, *Critical Evaluation and Optimization of the Thermodynamic Properties and Phase Diagrams of the Al-Mg, Al-Sr, Mg-Sr, and Al-Mg-Sr Systems*, Journal of Phase Equilibria 15(6) (1994) p. 591-605.
https://doi.org/10.1007/BF02647620
[19] H. Mehrer, S. Divinski, *Diffusion in Metallic Elements and Intermetallics*, Defect and Diffusion Forum (289-292) (2009) p. 15-38.
DOI: 10.4028/www.scientific.net/DDF.289-292.15
[20] V.I. Dybkov, *Reaction Diffusion and Solid State Chemical Kinetics*, Transtech Publications, Zurich, 2010.
[21] Y. Funamizu, K. Watanabe, *Interdiffusion in the Al-Mg System*, Transactions of the Japan Institute of Metals 13 (1972) p. 278-283.
[22] S. Brennan, A.P. Warren, K.R. Coffey, N.J. Kulkarni, P. Todd, M. Kilmov, Y. Sohn, *Aluminum Impurity Diffusion in Magnesium*, Journal of Phase Equilibria and Diffusion 33(2) (2012) p. 121-125.
https://doi.org/10.1007/s11669-012-0007-2
[23] A.D. Smigelskas, E.O. Kirkendall, *Zinc Diffusion in Alpha Brass*, Transactions of the Metallurgical Society of AIME 171 (1947) p. 130-142.
[24] S.K. Das, Y.-M. Kim, T. K. Ha, R. Gauvin, I.-H. Jung, *Anisotropic Diffusion Behavior of Al in Mg: Diffusion Couple Study Using Mg Single Crystal*, Metallurgical and Materials Transactions A 44 (2013) p. 2539-2547.
https://doi.org/10.1007/s11661-013-1636-8
[25] S. Fujikawa, K. Hirano, *Diffusion of ^{28}Mg in Aluminum*, Materials Science and Engineering 27 (1977) p. 25-33.
https://doi.org/10.1016/0025-5416(77)90190-2
[26] J.W. Christian, *The Theory of Transfomations in Metals and Alloys*, Pergamon Press, Oxford New York Toronto Sydney Paris Braunschweig, 1975.
https://doi.org/10.1016/B978-0-08-044019-4.X5000-4
[27] D. Eliezer, E. Aghion, F.H. Froes, *Magnesium Science, Technology and Applications*, Advanced Performance Materials 5(3) (1998) p. 12.
[28] I.J. Polmear, *Magnesium Alloys and Applications*, Materials Science and Technology 10 (1994) 1-16.https://doi.org/10.1179/mst.1994.10.1.1
[29] S S. Sandlöbes, M. Friák, S. Zaefferer, A. Dick, S. Yi, D. Letzig, Z. Pei, L.F. Zhu, J. Neugebauer, D. Raabe, *The relation between ductility and stacking fault energies in Mg and Mg–Y alloys*, Acta Materialia 60(6) (2012) p. 3011-3021.
https://doi.org/10.1016/j.actamat.2012.02.006
[30] G.I. Taylor, *Plastic strain in metals*, Journal of the Institute of Metals 62 (1938) 307-324.
[31] R.V. Mises, *Mechanik der plastischen Formänderung von Kristallen*, Zeitschrift für Angewandte Mathematik und Mechanik 8 (1928) p. 161-185.
[32] P.G. Partridge, T*he crystallography and deformation modes of hexagonal close packed metals*, Metallurgical Reviews 12 (1967) p. 169-194.
[33] S. Yi, *Investigation on the deformation behavior and the texture evolution in magnesium wrought alloy AZ31*, PhD thesis, Clausthal University of Technology, 2005.
[34] M.H. Yoo, *Slip, twinning, and fracture in hexagonal close-packed metals*, Metallurgical Transactions A 12(3) (1981) p. 409-418. https://doi.org/10.1007/BF02648537
[35] S.R. Agnew, *Deformation mechanisms of magnesium alloys,* in: Advances in wrought magnesium alloys: Fundamentals of processing, properties and applications, Woodhead Publishing, 2012 p. 63-103.

[36] B.F. Figgins, G.O. Jones, D.P. Riley, *The thermal expansion of aluminium at low temperatures as measured by an X-ray diffraction method*, Philosophical Magazine 1 (1956).https://doi.org/10.1080/14786435608238150
[37] M.E. Straumanis, *The Precision Determination of Lattice Constants by the Powder and Rotating Crystal Methods and Applications*, Journal of Applied Physics 20(12) (1949) p. 726-734. DOI:10.1063/1.1698520
[38] J. Hirsch, K. Lücke, *Mechanism of deformation and development of rolling textures in polycrystalline F.C.C. metals*, Acta Metallurgica. (1988) p. 2883-2904. https://doi.org/10.1016/0001-6160(88)90173-3
[39] J. Hirsch, *Crystallographic textures,a magnifying glass to investigate materials*, in: Microstructural Design of Advanced Engineering Materials, Wiley-VCH, Weinheim, 2013. https://doi.org/10.1002/9783527652815.ch16
[40] N. Hansen, D.A. Hughes, *High angle boundaries formed by grain subdivision mechanisms*, Acta Materialia 45(9) (1997) p. 3871-3886. https://doi.org/10.1016/S1359-6454(97)00027-X
[41] D.A. Hughes, M.E. Kassner, M.G. Stout, J.S. Vetrano, *Metal forming at the center of excellence for the synthesis and processing of advanced materials*, Journal of The Minerals Metals & Materials Society 50(6) (1998) p. 16-21. https://doi.org/10.1007/s11837-998-0122-z
[42] N. Jia, P. Eisenlohr, F. Roters, D. Raabe, X. Zhao, *Orientation dependence of shear banding in face-centered-cubic single crystals*, Acta Materialia 60(8) (2012) p. 3415-3434. https://doi.org/10.1016/j.actamat.2012.03.005
[43] E. Bauer, H. Kaldarar, R. Lackner, H. Michor, W. Steiner, E.-W. Scheidt, A. Galatanu, F. Marabelli, T. Wazumi, K. Kumagai, M. Feuerbacher, *Superconductivity in the complex metallic alloy β-Al_3Mg_2,* Physical Review B 76 (2007) 014528. DOI:https://doi.org/10.1103/PhysRevB.76.014528
[44] K. Urban, M. Feuerbacher, *Structurally complex alloy phases*, Journal of Non-Crystalline Solids Volume 334-335(2004) 143-150. https://doi.org/10.1016/j.jnoncrysol.2003.11.029
[45] K. Riederer, *Das system Aluminum-Magnesium-Zink,* Zeitschrift für Metallkunde 28 (1936) p. 312.
[46] F. Laves, K. Möller, *Contribution to the Understanding of the Aluminum-Magnesium System,* Z. Metallkd. 30 (1938) p. 232-235.
[47] H. Perlitz, *Crystal Structure of β-Aluminium-Magnesium Alloy*, Nature 154 (1944) 606.
[48] S. Samson, *The Crystal Structure of the Phase β Al_3Mg_2*, Acta Crystallographica 19 (1965) p. 401-413. https://doi.org/10.1107/S0365110X65005133
[49] M. Feuerbacher, C. Thomas, J. Makongo, S. Hoffmann, W. Carrillo-Cabrera, R. Cardoso, Y. Grin, G. Kreiner, J.-M. Joubert, T. Chenk, J. Gastaldi, H. Nguyen-Thi, N. Mangelinck-Noël, B. Billia, P. Donnadieu, A. Czyrska-Filemonowicz, A. Zielińska-Lipiec, B. Dubiel, T. Weber, W. Steurer, *The Samson phase, β-Al_3Mg_2, revisted,* Zeitschrift für Kristallographie 222(6) (2007) p. 259-288. doi:10.1524/zkri.2007.222.6.259
[50] J. Wolny, M. Duda, *Ordering of hexagonal layers in phase β and β'-Mg_2Al_3 phases,* Philosophical Magazine 91 (2011) p. 1568-1580. doi:10.1088/1742-6596/226/1/012035
[51] F. Laves, K. Löhberg, P. Rahlfs, *Über die Isomorphie von Mg_3Al_2 und α-Mangan*, Nachrichten von der Gesellschaft der Wissenschaften zu Göttingen Mathematisch-physikalische Klasse, neue Folge, Fachgruppe iv, Vandenhoek & Ruprecht, Göttingen (1934) p. 67-71.
[52] A. Bradley, J. Thewlis, *The crystal structure of α-manganese,* Proceedings of The Royal Society A: Mathematical, Physical and Engineering Sciences 115 (1927), p. 456-471.

[53] F.C. Frank, J.S. Kasper, *Complex alloy structures regarded as sphere packings.* II. Analysis and classification of representative structures, Acta Crystallographica 12 (1959), p. 483-499. https://doi.org/10.1107/S0365110X58000487
[54] J.-M. Joubert, M. Phejar, *Crystal chemistry and Calphad modelling of the χ phase*, Progress in Materials Science 54 (7) (2009) p. 945-980. https://doi.org/10.1016/j.pmatsci.2009.04.002
[55] N.S. Kurnakov, V.I. Mikheeva, *Transformations in the middle part of the system aluminum-magnesium,* Izv. Sekt. Fiz.-Khim. Anal., Inst. Obshch. Neorg. Khim., Akad. Nauk SSSR 13 (1940), p. 209-214.
[56] W. Witt, *Absolute Präzisionsbestimmung von Gitterkonstanten an Germanium- und Aluminium-Einkristallen mit Elektroneninterferenzen*, Zeitschrift für Naturforschung A 22(1) (1966) p. 6. DOI: https://doi.org/10.1515/zna-1967-0115
[57] P. Schobinger-Papamantellos , P. Fischer, *Neutronenbeugungsuntersuchungen der Atomverteilung von $Mg_{17}Al_{12}$*, Naturwissenschaften 57(3) (1970) p. 128-129.
[58] H. J. Bunge, M. Humbert, P. I. Welch, *Texture Transformation,* Textures and Microstructures 6 (1984) p. 81-96.DOI: 10.1155/TSM.6.81
[59] E.C. Bain, *The Nature of martensite*, Trans. AIME Steel Division 70 (1924) 4.
[60] G.V. Kurdjumov, G. Sachs, *Crystallographic orientation relationship between α-and γ-Fe*, Zeitschrift für Physik 64 (1930) 325.
[61] Z. Nishiyama, *X-ray investigation of the mechanism of the transformation from face centered cubic lattice to body centered cubic,* Science Report Tokohu Univ. 23 (1934) 637.
[62] G. Brückner, G. Gottstein, *Transformation textures during diffusional α→γ→α phase transformations in ferritic steels*, ISIJ International 41 (2001) p. 468-477.
[63] M. Bernole, R. Graf, P. Guyot, *Electron Microscope and X-ray Study of Precipitation in an Al-10 Mg Alloy at Ambient Temperature*, Philosophical Magazine 28(4) (1973) p. 771–782
[64] Y. Zhao, Z. Ding, Y. Chen, *Crystallographic orientations of intermetallic compounds of a multi-pass friction stir processed Al/Mg composite materials*, Materials Characterization 128 (2017) p. 156-164. https://doi.org/10.1016/j.matchar.2017.02.005.
[65] A.F. Crawley, K.S. Milliken, *Precipitate morphology and orientation relationships in an aged Mg-9% Al-1% Zn-0.3% Mn alloy,* Acta Metallurgica 22 (1974), p. 557-562. //doi.org/10.1016/j.matpr.2015.05.002.
[66] A.F. Crawley, B. Lagowski, *Effect of two-step aging on the precipitate structure in magnesium alloy AZ91*, Metallurgical and Materials Transactions B 5 (1974), p. 949-951. //doi.org/10.1007/BF02643153.
[67] S. Celotto, *TEM study of continuous precipitation in Mg-9 Wt%Al-l Wt%Zn alloy,* Acta Materialia 48(8) (2000), p. 1775-1787. 10.1016/S1359-6454(00)00004-5.
[68] D. Duly, *Application of the invariant line model for b.c.c./h.c.p. couples: A criterion based on surface variations,* Acta Metallurgica 41(5) (1993), p. 1559-1566. //doi.org/10.1016/0956-7151(93)90264-S.
[69] W. Pitsch, A. Schrader, *Die Ausscheidungsform des ε-Karbids im Ferrit und im Martensit beim Anlassen,* Archiv für das Eisenhüttenwesen 29 (1958), p. 715-721. //doi.org/10.1002/srin.195803018.
[70] W.G. Burgers, *On the Process of transition of the Cubic-body-centered modification into the hexagonal-closed-packed modification of zirconium,* Physica 1(7-12) (1934), p. 561-586. //doi.org/10.1016/S0031-8914(34)80244-3.
[71] D.L. Potter, *The structure, morphology and orientation relationship of V_3N in α-vanadium*, Journal of the Less Common Metals 31(2) (1973) p. 299-309.
[72] J.P. Zhou, D.S. Zhao, R.H. Wang, Z.F. Sun, J.B. Wang, J.N. Gui, O. Zheng, *In situ observation of ageing process and new morphologies of continuous precipitates in AZ91 magnesium alloy*, Materials Letters 61(25) (2007) p. 4707-4710. https://doi.org/10.1016/j.matlet.2007.03.013

[73] D.A. Porter, J.W. Edington, *Microanalysis and cell boundary velocity measurements for the cellular reaction in a Mg-9% Al alloy*, Proceedings of the Royal Society A 358(1694) (1978) p. 335-350. https://doi.org/10.1098/rspa.1978.0015
[74] M.-X. Zhang, P.M. Kelly, *Edge-to-edge matching and its applications: Part I. Application to the simple HCP/BCC system*, Acta Materialia. 53(4) (2005) p. 1073-1084. https://doi.org/10.1016/j.actamat.2004.11.007
[75] M.-X. Zhang, P.M. Kelly, *Edge-to-edge matching and its applications: Part II.* Application to Mg–Al, Mg–Y and Mg–Mn alloys, Acta Materialia. 53(4) (2005) p. 1085-1096.https://doi.org/10.1016/j.actamat.2004.11.005
[76] M.-X. Zhang, P.M. Kelly, *Crystallography of $Mg_{17}Al_{12}$ precipitates in AZ91D alloy*, Scripta Materialia 48(3) (2003) p. 647-652. https://doi.org/10.1016/S1359-6462(02)00555-9
[77] C.P. Luo, X.L. Xiao, J.W. Liu, J.F. Nie, B.C. Muddle, *Multi-orientation relationship and {112}γ pseudo-twin relationship of γ-$Mg_{17}Al_{12}$ precipitates in an AZ91 Mg-Al alloy*, Acta Metallurgica Sinica 38(7)(2002) p. 709–714.
[78] D. Duly, W.-Z. Zhang, M. Audier, *High-resolution electron microscopy observations of the interface structure of continuous precipitates in a Mg-Al alloy and interpretation with the O-lattice theory*, Philosophical Magazine A 19A (1995) p. 187-204. https://doi.org/10.1080/01418619508242964
[79] U. Dahmen, *Orientation relationships in precipitation systems*, Acta Metallurgica 30(1) (1982) p. 63-73.https://doi.org/10.1016/0001-6160(82)90045-1.
[80] O. Zhengab, J.P. Zhouab, D.S. Zhao, J.B. Wang, R.H. Wang, J.N. Gui, D.X. Xiong, Z.F. Sun, *The crystallography of continuous precipitates with a newly observed orientation relationship in an Mg–Al-based alloy*, Scripta Materialia 60(9) (2009) p. 791-794. https://doi.org/10.1016/j.scriptamat.2009.01.016
[81] X.L. Xiao, C.P. Luo, J.F. Nie, B.C. Muddle, *Morphology and crystallography of β-$Mg_{17}Al_{12}$ precipitate in AZ91 Magnesium-Aluminum Alloy*, Acta Metallurgica Sinica 37 (2001) 1-7.
[82] Z.Z. Shi, W.-Z. Zhang, *A transmission electron microscopy investigation of crystallography of τ-$Mg_{32}(Al, Zn)_{49}$ precipitates in a Mg–Zn–Al alloy*, Scripta Materialia 64(2) p. 201-204. https://doi.org/10.1016/j.scriptamat.2010.09.044.
[83] Y. Matsukawa, I. Okuma, H. Muta, Y. Shinohara, R. Suzue, H.L. Yang, T. Maruyama, T. Toyama, J.J. Shen, Y.F. Li, Y. Satoh, S. Yamanaka, H. Abe, *Crystallographic analysis on atomic-plane parallelisms between bcc precipitates and hcp matrix in recrystallized Zr-2.5Nb alloys*, Acta Materialia 126 (2017) p. 86-101. https://doi.org/10.1016/j.actamat.2016.12.053
[84] A.M.S. Hamouda, M.S.J. Hashmi, *Mechanical Properties of Aluminum metal matrix composites under impact loading,* Journal of Materials Processing Technology 56(1-4) (1996), p. 743-756. //doi.org/10.1016/0924-0136(95)01888-3.
[85] T.W. Clyne, P.J. Withers, *An introduction to metal matrix composites,* Cambridge University Press, New York, 1995. //doi.org/10.1017/CBO9780511623080
[86] D.B. Miracle, *Metal matrix composites – From science to technological significance,* Composites Science and Technology 65(15-16) (2005) p. 2526-2540. https://doi.org/10.1016/j.compscitech.2005.05.027.
[87] G. Frommeyer, G. Wassermann, *Microstructure and anomalous mechanical properties of in situ-produced silver-copper composite wires*, Acta Metallurgica 23(11) p.1353-1360.
[88] D. Raabe, U. Hangen, *Correlation of microstructure and type II superconductivity of a heavily cold rolled Cu-20mass%Nb,* Acta materialia,44(3)(1996), p. 953-961. //doi.org/10.1016/1359-6454(95)00239-1
[89] H.W. Bergmann, G. Fromeyer, G. Wassermann, *The dependence of the texture and microstructures in two-phase composites on the yield stresses of the components,* Proceeding of the Fifth International Conference on Textures of Materials (ICOTOM5)

March 28–31, 1978, Aachen,In: Texture of Materials; G. Gottstein, , K.Lücke, (Eds.); Springer-Verlag: Berlin, Germnay, (2007), Volume 2, p. 371–377, ISBN 0-387-09220-X.
[90] K. Xu, A.M. Russell, L. S. Chumbley, F. C. Laabsv, V. B. Gantovniky, Y. Tian, *Characterization of strength and microstructure in deformation processed Al-Mg composites,* Journal of Materials Science 34(24) (1999), p. 5955–5959. 10.1023/A:1004772526480.
[91] X. Kai, *Microstructure and strength of a deformation processed Al-20%Sn metal-metal composite, PhD Thesis*, Iowa State University, USA, 2003.
[92] H.-G. Brokmeier, *Experimental textures of Al-Pb,Al-Cu, and Fe-Cu metal-metal composites,* Materials Science and Engineering 175 (1994), p. 131-139. 10.1016/0921-5093(94)91052-9
[93] J. Grewen, G, Wassermann, *Textur-Untersuchungen an Draehten I.,* Zeitschrift für Metallkde. 45 (1954), p. 499-505.
[94] M. Dahms, T.J. Jewett, C. Michaelsen, *Phase Formation Kinetics of Titanium Aluminides Produceed from Elemental Powder Mixtures*, Zeitschrift für Metallkunde 88(2) (1997), p. 125-130.
[95] S. Gall, *GrundlegendeUntersuchungen zum Strangpressen von Magnesiumblechen und deren Weiterverarbeitung*: *Mikrostruktur und mechanische Eigenschaften,* PhD Thesis,Technische Universität Berlin, Berlin, 2013.
[96] S. Müller, *Weiterentwicklung des Strangpressens von AZ Magnesiumlegierungen im Hinblick auf eine Optimierung der Mikrostruktur des Gefüges und der mechanischen Eigenschaften,* Dissertation, Fakultät Prozesswissenschaften TU Berlin, Berlin, 2007.
[97] G.S. M.Bauser, K. Siegert, *Strangpressen*, Aluminium-Verlag, Düsseldorf, Germany, 2001.
[98] K. Müller, *Grundlage des Strangpressens*, Expert Verlag, Germany, 2003.
[99] H.-G. Brokmeier, H. J, *Neutron Diffraction Texture Analysis of 1 Vol.% Cu in Aluminium,* Textures and Microstructures 10 (1988), p. 1-8.
[100] H.-J. Bunge, *Texture analysis in materials science*, Butterworth, London, 1982.
[101] V. Pecharsky, P. Zavalij, *Fundamentals of Powder diffraction and Structural Chracterization of Materials*, Springer, United States of America, 2005.
[102] D.W. Kerst, *A 20-million-electron-volt betatron or induction accelerator,* Review of Scientific Instruments, 13 (1942), p. 387-394. https://doi.org/10.1063/1.1770070
[103] J. Schwinger, *On the classical radiation of accelerated electrons*, Physical Review 75(12) (1949) p. 14.
[104] S.K. H.Hsieh, A.Luccio, C. Pellegrini and A.van Steenbergen, *Wiggler, Undulator and free electron laser radiation sources development at the national synchrotron light source*, Nuclear Instrumments and Methods 208(1-3)(1983) p. 79-90.
[105] H. Winick, G. Brown, K. Halbach and J. Harris, *Wiggler and Undulator Magnets*, Physics Today 34(5) (1981) p. 50-63.
[106] G. Gottstein, *Automatic Microtexture determination with synchrotron radiation*, In: Eight International Conference on Textures of Materials (ICOTOM8), Santafe, J.S. Kallend. G. Gottstein (Eds.), The metallurgical Society, Warrendale, 1988. 10.1557/PROC-143-259.
[107] H. F. Poulsen, S. Garbe, T. Lorentzen, D. Juul Jensen, F. W. Poulsen, N. H. Andersen, T. Frello, R. Feidenhans and H. Graafsma, *Applications of High-Energy Synchrotron Radiation for Structural Studies of Polycrystalline Materials*, Journal of Synchrotron Radiation 4 (1997) p. 147-154. https://doi.org/10.1107/S0909049597002021
[108] K.J. Roberts, *The application of synchrotron X-ray techniques to problems in crystal science and engineering*, Journal of Crystal Growth 130 (3-4) (1993), p. 657-681. //doi.org/10.1016/0022-0248(93)90556-C.
[109] H.-R. Wenk, S. Grigull, *Synchrotron texture analysis with area detectors*, Journal of Applied Crystallography 36 (2003), p. 1040-1049. //doi.org/10.1107/S0021889803010136.
[110] J.G. G. Wassermann, *Texturen metallischer Werkstoffe*, Springer Verlag, Berlin, 1962.

[111] H.-G. Brokmeier, *Hard X-rays for In Situ Strain and Texture Measurements*, Particle and Particle Systems, (26) (2009) p.117-124. 10.1002/ppsc.200800050.
[112] L. Wcislak, H.Klein, H. J. Bunge, U. Garbe,T. Tschentschera and J. R. Schneidera, *Texture analysis with high-energy synchrotron radiation*, Journal of Applied Crystallography 35 (2002) p. 82-95. https://doi.org/10.1107/S0021889801019902
[113] A. Beer, *Bestimmung der Absorption des rothen Lichts in farbigen Flüssigkeiten*, Annalen der Physik und Chemie 86 (1852) p. 78-88.
[114] H.M. Rietveld, *A profile refinement method for nuclear and magnetic structures,* Journal of Applied Crystallography 2 (1969), p. 65-71. //doi.org/10.1107/S002188986900655.
[115] K. Helming, U. Preckwinkel, *Texture analysis with area detectors*, in: C. Esling, M. Humbert, R.A. Schwarzer and F. Wagner (Ed.), Solid State Phenomena 105 (2005) p. 71-76. DOI: 10.4028/www.scientific.net/SSP.105.71
[116] H.-G. Brokmeier, S. Yi, *Textures in Engineering Materials*, in: P. Staron, A. Schreyer, H. Clemens, S. Mayer (Eds.), Neutrons and Synchrotron Radiation in Engineering Materials Science, Wiley-VCH, Weinheim Germany, 2017, p. 55-71. https://doi.org/10.1002/9783527684489.ch3
[117] A.P. Hammersley, *FIT2D: An Introduction and Overview,* ESRF Internal Report, ESRF97HA02T (1997).
[118] M. Dahms, H.-J. Bunge, *The iterative series-expansion method for quantitative texture analysis*. I. General outline, Journal of Applied Crystallography (22) (1989) p. 439-447. //doi.org/10.1107/S0021889889005261.
[119] S. Scudino, M. Sakaliyska, K.B. Surreddi, J. Eckert, *Mechanical alloying and milling of Al–Mg alloys,* Journal of Alloys and Compounds 483(1-2) (2009), p. 2-7. 10.1016/j.jallcom.2008.07.161.
[120] R.S. Busk, *Lattice parameters of Magnesium Alloys*, Journal of Metals 188 (1950) p. 1460-1464. https://doi.org/10.1007/BF03399173
[121] L. Lutterotti, S. Matthies, H. Wenk, *MAUD:* a *friendly Java program for material analysis using diffraction*, Newsletter of the CPD 21 (1999) p. 14-15.
[122] P. Liang, P. Donnadieu, M.G. Harmelin, A.Quivy, P.Ochin, G.Effenberg, H.-J. Siefert, H.-L. Lukas, F.Aldinger, *Experimental investigation and thermodynamic calculation of the central part of the Mg-Al phase diagram*, Zeitschrift für Metallkunde, 89(8), p. 536-540.
[123] J. Philibert, *Reactive Interdiffusion*, Materials Science Forum (155-156) (1994) p. 15-30.https://doi.org/10.4028/www.scientific.net/MSF.155-156.15
[124] G. Gibbs, *Diffusion Layer Growth in a binary System*, Journal of Nuclear Materials 20(3) (1966) p. 303-306. https://doi.org/10.1016/0022-3115(66)90042-0
[125] M. Kajihara, *Analysis of kinetics of reactive diffusion in a hypothetical binary system*, Acta Materialia 52(5)(2004) p.1193-1200. https://doi.org/10.1016/j.actamat.2003.10.047
[126] G. Kidson, *Some Aspects of the Growth of Diffusion Layers in Binary Systems*, *Journal of Nuclear Materials*. 3(1) (1961) p. 21-29.
[127] G. Gottstein, *Physical Foundations of Materials Science*, Springer-Verlag Berlin Heidelberg, 2004.
[128] S. Brennan, K. Bermudez, N.S. Kulkarni, Y. Sohn, *Interdiffusion in the Mg-Al System and Intrinsic Diffusion in β-Mg_2Al_3*, Metallurgical and Materials Transactions A 43(11) (2012) p. 4043-4052. https://doi.org/10.1007/s11661-012-1248-8
[129] E. M. Tanguep Njiokep, M. Salamon, H. Mehrer, *Growth of Intermetallic Phases in the Al-Mg System,* Defect and Diffusion Forum (194-199) (2001), p. 1581-1586. 10.4028/www.scientific.net/DDF.194-199.1581.
[130] J. Robson, A. Panteli, P.B. Prangnell, *Modelling intermetallic phase formation in dissimilar metal ultrasonic welding of aluminium and magnesium alloys*, Science and Technology of Welding and Joining 17(6) (2013), p. 447-453. //doi.org/10.1179/1362171812Y.0000000032.

[131] Z.F. Li, J. Dong, X.Q. Zeng, C. Lu, W.J. Ding, Z.M. Ren, *Influence of strong static magnetic field on intermediate phase growth in Mg–Al diffusion couple*, Journal of Alloys and Compounds 440(1-2) (2007) p. 132-136. https://doi.org/10.1016/j.jallcom.2006.09.032
[132] T. Takenaka, S. Kano, M. Kajihara, N.Kurokawa, K. Sakamoto, *Growth behavior of compound layers in Sn/Cu/Sn diffusion couples during annealing at 433-473 °K*, Material Science and Engineering: A 396 (2005) p. 115-123. https://doi.org/10.1016/j.msea.2005.01.025
[133] C. Brubaker, Z.-K. Liu, *Diffusion Couple Study of the Mg-Al System*, in: A. A.Luo (Ed.) Magnesium Technology, The minerals, Metals & Materials Society, 2004, p. 229-234.
[134] H.-G. Brokmeier, *Hot rectangular extrusion textures of six Mg-alloys via neutron diffraction,* Advanced engineering materials 20 (2018) 1700234. https://doi.org/10.1002/adem.201700234.
[135] K. Hantzsche, J. Bohlen, J. Wendt, K.U. Kainer, S. Yi, D. Letzig, *Effect of rare earth additions on microstructure and texture development of magnesium alloy sheets,* Scripta Materialia 63(7) (2010), p. 725-730. //doi.org/10.1016/j.scriptamat.2009.12.033.
[136] U. Schläfer, H.J. Bunge, *Cyclic textures in Aluminium wires,* Textures 1(31-49) (1972), p. 31-49. 10.1155/TSM.1.31
[137] G. Tempus, W. Calles, G. Scharf, , *Influence of extrusion process parameters on the mechanical properties of Al-Li-Extrusions,* Journal de Physique Colloques C3(48) (1987), p. 187-193. https://doi.org/10.1179/mst.1991.7.10.937
[138] M.A. Przystupa, A.K. Vasudēvan, A.D. Rollet, *Crystallographic texture gradients in the aluminum 8090 matrix alloy and 8090 particulate composites,* Materials Science and Engineering A, A186(1-2) (1994), p. 35-44. 10.1016/0921-5093(94)90303-4
[139] Z.Y. Zhong, H.G. Brokmeier, E. Maawad, N. Schell, *Texture dependent lattice strains and texture gradient in Al7020*, In: The 17th International Conference on Textures of Materials (ICOTOM17), W. Skrotzki, C.-G. Oertel (Eds.) IOP Conference Series: Materials Science and Engineering, Dresden, Germany, 2015. DOI: 10.1088/1757-899X/82/1/012100
[140] S.R. Agnew, Ö. Duygulu, *Plastic anisotropy and the role of non-basal slip in magnesium alloy AZ31B,* International Journal of Plasticity 21(6) (2005), p. 1161-1193. //doi.org/10.1016/j.ijplas.2004.05.018.
[141] S.R. Agnew, M.H. Yoo, C.N. Tome, *Application of texture simulation to understanding mechanical behavior of Mg and solid solution alloys conatining Li or Y*, Acta Materialia 49, (2001), p. 4277-4289. 10.1016/S1359-6454(01)00297-X.
[142] M.A. Steiner, J.J. Bhattachary, S.R. Agnew, *The origin and enhancement of <0001>{11$\bar{2}$0} texture during heat treatment of rolled AZ31B magnesium alloys*, Acta Materialia 95 (2015) p. 443-455. 10.1016/j.actamat.2015.04.043
[143] M.T. Pérez-Prado, J.A. del Valle, O.A. Ruano, *Effect of sheet thickness on the microstructural evolution of an Mg AZ61 alloy during large strain hot rolling,* Scripta Materialia 50(5) (2004), p. 667-671. //doi.org/10.1016/j.scriptamat.2003.11.015.
[144] S. Yi, J. Bohlen, S. Sandlöbes, S. Zaefferer, D. Letzig, K.U. Kainer, *Microstructural evolution during recrystallization of magneisum alloys,* Materials Science Forum (6) (2012) p. 706-709. https://doi.org/10.4028/www.scientific.net/MSF.706-709.1291
[145] G. Gottstein, T. Al Samman, *Texture Development in pure Mg and Mg alloy AZ31,* Materials Science Forum (495-497) (2005) p. 623-632. https://doi.org/10.4028/www.scientific.net/MSF.495-497.623.
[146] A.A. Ridha, W.B. Hutschinson, *Recrystallisation mechanism and the origin of cube texture in copper,* Acta Metallurgica 30(10) (1982) p. 1929-1939. https://doi.org/10.1016/0001-6160(82)90033-5
[147] A.L. Dons, E. Nes, *Nucleation of cube texture in aluminium,* Materials Science and Technology 2(1) (1986) p. 8-18. //doi.org/10.1179/mst.1986.2.1.8

[148] H. Erik Vatne, E. Nes, O. Daaland, *On the Formation of Cube Texture in Aluminium,* Materials Science Forum, (157-162) (1994), p. 1087-1094. 10.4028/www.scientific.net/MSF.157-162.1087.
[149] D.N. Lee, H. Nam Han, *The Cube Recrystallization-Texture Related Component in the β-Fiber Rolling-Texture FCC Metals,* Materials Science Forum (783-786) (2014), p. 51-56. 10.4028/www.scientific.net/MSF.783-786.51.
[150] D.N. Lee, *Strain energy release maximization model for recrystallization textures,* Metals and Materials 5 (1999), p. 401-417. https://doi.org/10.1007/BF03026153.
[151] M.-X. Zhang, P.M. Kelly, *Crystallographic features of phase transformations in solids*, Progress in Materials Science 54(8) (2009) p. 1101-1170. https://doi.org/10.1016/j.pmatsci.2009.06.001
[152] H.Liu, J. Liu, L. Ouyang, C. Luo, *On the multiple orientation relationship of the Mg/γ-$Mg_{17}Al_{12}$ precipitation system,*, Journal of Applied Crystallography, 45 (2) (2012) p. 224-233. DOI: 10.1107/S002188981200091X

7 Appendix

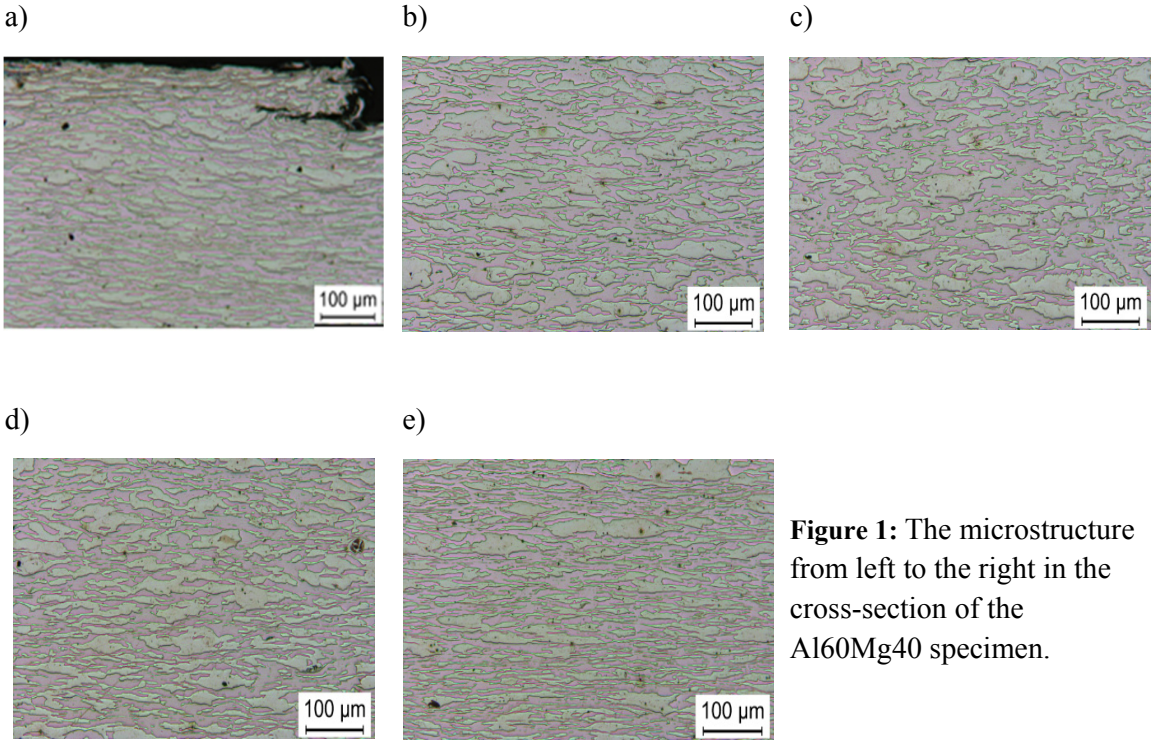

Figure 1: The microstructure from left to the right in the cross-section of the Al60Mg40 specimen.

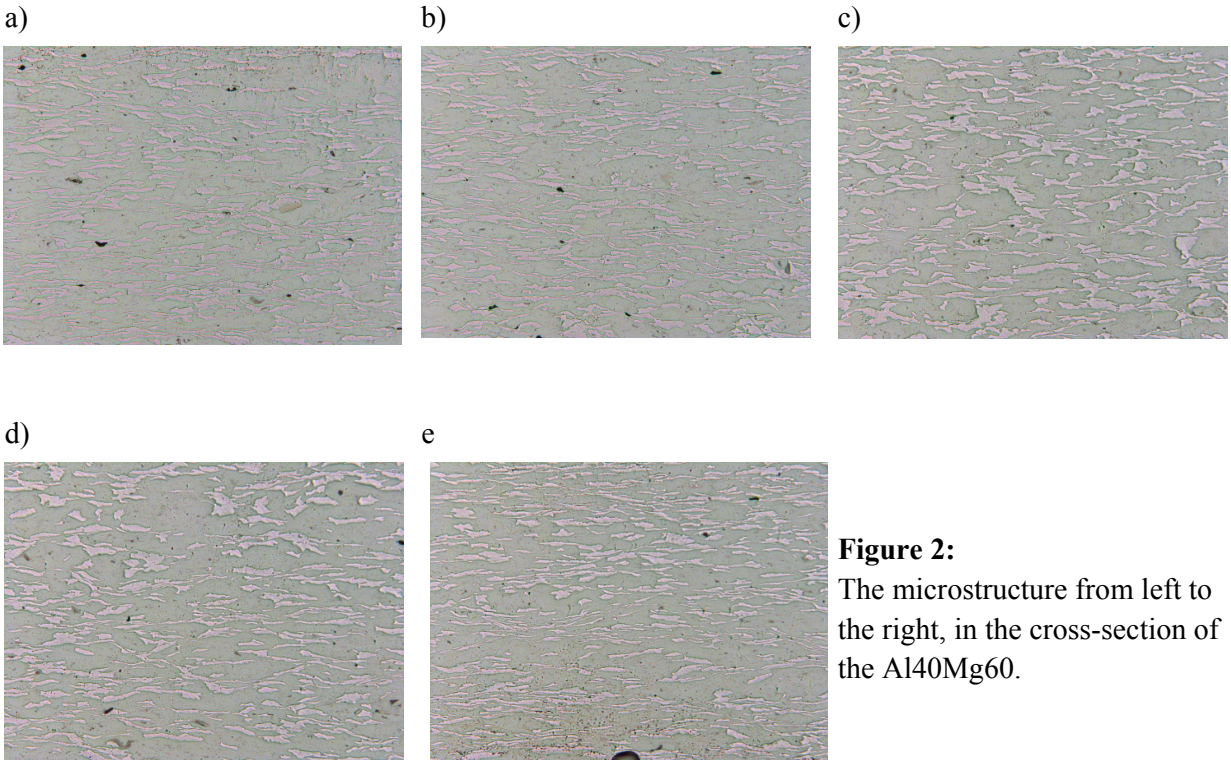

Figure 2:
The microstructure from left to the right, in the cross-section of the Al40Mg60.

Pubications

Publication in connection to the thesis:

- S. Sanamar, H.-G Brokmeier, N. Schell, Texture Gradient in a Rectangular Extruded Al60Mg40 Metal Matrix Composite, 2019, Metals, 167, 9(2), https://doi.org/10.3390/met9020167

- S. Sanamar, H.-G Brokmeier, N. Schell, Phase evolution of Al-Mg metal matrix composites during low temperature annealing at 200 °C and 250 °C, Intermetallics, Volume 124, September 2020, https://doi.org/10.1016/j.intermet.2020.106862

- S. Sanamar, H.-G. Brokmeier, N. Schell, $Al_{12}Mg_{17}$ and Al_3Mg_2 formation during annealing of Al-Mg composites studied by high-energy X-ray diffraction (in progress).

Publications:

- R. Kalsar, S. Sanamar, N. Schell, H-G. Brokmeier, R. Saha , P. Ghosh , A.N. Bhagat, Satyam Suwas, Rapid elemental partitioning in medium Mn steel during short time annealing: An in-situ study using synchrotron X-rays, January 2019, SSRN Electronic Journal, DOI: 10.2139/ssrn.3339909

- R. Kalsar, S. Sanamar, N. Schell, H-G. Brokmeier, R. Saha , P. Ghosh , A.N. Bhagat, Satyam Suwas, Elemental partitioning in medium Mn steel during short-time annealing: an in-situ study using synchrotron x-rays, January 2020, Materialia, https://doi.org/10.1016/j.mtla.2020.100594.

Thesis:

-Vergleichende Untersuchungen zur Textur unterschiedlicher Aluminiumbleche, Masterarbeit vorgelegt von Chang Liu, Kooperation mit Novelis Deutschland,
Betreuer: M.Sc. Soheil Sanamar, Referent: Prof. Dr. rer. nat. Dr. Ing. habil Heinz-Günter Brokmeier, Korreferent: Prof. Dr. Ing. habil. Lothar Wagner. TU Clausthal.

Conference:

-S. Sanamar, H.-G Brokmeier, N. Schell, Texture evolution of Al40Mg60 composite during thermal treatments, Annual Texture Symposium of DGM-SF2M, March 2019, Garching, Germany.